Universitá degli Studi di Pavia
Dottorato di Ricerca in Fisica - xxx Ciclo

Feasibility study of a CdZnTe prototype detector for BNCT-SPECT imaging on small animals.

Setareh Fatemi

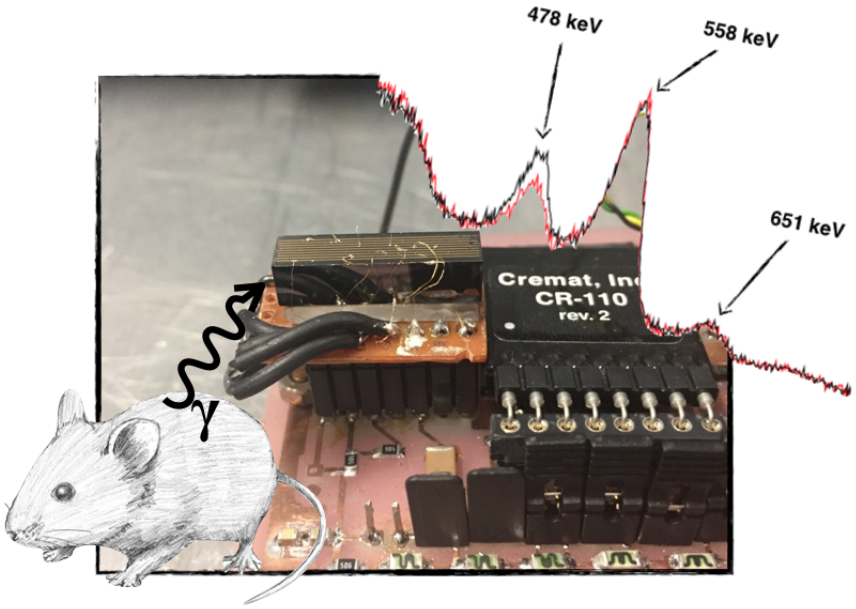

Tesi per il conseguimento del titolo

Full Title: Feasibility study of a CdZnTe prototype detector for BNCT-SPECT imaging on small animals.

Setareh Fatemi

2017

University of Pavia

Department of Physics

Istituto Nazionale di Fisica Nucleare

Dottorato di Ricerca in Fisica - XXX Ciclo

Feasibility study of a CdZnTe prototype detector for BNCT-SPECT imaging on small animals.

dissertation submitted by

Setareh Fatemi

Submitted to the Graduate School in Physics in partial fullfillment of the requirements for the degree of

DOTTORE DI RICERCA IN FISICA
DOCTOR OF PHILOSOPHY IN PHYSICS

Supervisor: Prof. Saverio Altieri (University of Pavia)

Co-supervisor: Dr. Nicoletta Protti (INFN Pavia)

Referee: Prof. Alejandro Valda (University of San Martín)

Referee: Dr. Michal Gryzinski (National Centre for Nuclear Research)

Cover: 5x5x20 mm^3 CZT detector studied in the thesis (centre), small animal model for preclinical studies (left), spectrum obtained in thermal column measurements at L.E.N.A. laboratory (right).

Feasibility study of a CdZnTe prototype detector for BNCT-SPECT imaging on small animals
Setareh Fatemi
PhD thesis - University of Pavia
Pavia, Italy, January 2018

To Evelyn,
remember that anyone can dream

Contents

Summary

Boron Neutron Capture Therapy (BNCT) is a binary radiotherapy modality based on the neutron capture reaction n + ^{10}B $\rightarrow$ ^{7}Li + α induced by thermal neutrons.
BNCT consists of two phases, first a ^{10}B carrier compound, which has the ability to preferentially accumulate in the tumour than in the healthy tissue, is administered to the patient and then the tumour is irradiated with a neutron beam.
The thermal neutrons interaction with the ^{10}B carrier compound produces alpha particles and ^{7}Li ions. In the 94% of captures the ^{7}Li ion is produced in an excited state which causes the emission of a prompt gamma ray of 478 keV. The range of the alpha particles and the ^{7}Li ions is less than 10 μm which is smaller than the mean cell diameter and therefore most of the reaction energy is deposited in the ^{10}B filled target cell. Hence BNCT has a cell level selectivity.
The effectiveness of BNCT strongly depends on the microscopic distribution of ^{10}B in tumour cells at the time of irradiation.
Many methods have been developed to evaluate the ^{10}B concentration in the tumour but none of them gives the information live during the treatment.
The development of a Single Photon Emission Computed Tomography (SPECT) system, that exploits the 478 keV gamma ray emitted during the therapy, for mapping of ^{10}B reaction rate inside the patient will allow a real time monitoring of the therapeutic dose delivered in the irradiated volume. The on-line measurement will make it possible to optimize the dose delivering during the irradiation, thus improving the effectiveness of the treatment.
Aim of this thesis was to evaluate the performances of a SPECT system for small animals, starting from the experimental characterization of a CdZnTe (CZT) semiconductor detector for the spectrometry of ^{7}Li 478 keV gamma rays and the computational study of its imaging capabilities.
This thesis is structured in five chapters and a conclusion section.
The first chapter is an introduction to BNCT and an overview of the most commonly used methods to measure the ^{10}B concentration in samples and *in-vivo*. Moreover the first chapter gives an introduction to SPECT imaging describing

the software and hardware requirements for a high performing SPECT system. Finally the rationale and the requirements for SPECT in BNCT are also discussed in chapter 1.
In chapter 2 the properties and advantages of a solid state detector are discussed focusing on the Cadmium Zinc Telluride detector. The energy, timing and spatial resolution of a CZT detector are discussed and compared to the most commonly used detector in SPECT imaging.
Chapter 3 is dedicated to the simulation studies started in collaboration with Ph.D. student Chunhui Gong at Nanjing University of Aeronautics and Astronautics during the author research period in Nanjing, China. Main focus of these simulation studies were the image reconstruction capabilities of a 20x20x20 mm^3 CZT detector employed as a base element for a BNCT-SPECT imaging system. The results of this work are discussed in chapter 3.
In the fourth chapter the experimental characterization of a 5x5x20 mm^3 CZT detector is presented. The prototype CZT detector was tested using standard calibration gamma source and its energy resolution and efficiency were studied. To conclude the characterization of the 5x5x20 mm^3 CZT detector a measurement campaign was carried out at the University of Pavia TRIGA Mark II reactor. In chapter 5 the results of these measurements are discussed showing the prototype detector performances when employed in a neutron and photon mixed field.
In the final section the conclusions of this thesis work and the future steps are presented.

Chapter 1

Introduction

1.1 Boron Neutron Capture Therapy

Boron Neutron Capture Therapy (BNCT) is a binary radiation therapy which is able to selectively destroy malignant cells while sparing the normal tissue. BNCT is based on the ^{10}B high capture cross section (3840 barns) of thermal neutrons ($E_n < 0.5eV$) (shown in Figure 1.1) which yields charged particles with high linear energy transfer (LET) such as α particles and ^7Li-nuclei.

$$n+^{10}B \Longrightarrow \begin{cases} ^7\mathrm{Li} + \alpha, & \mathrm{E}_{Li} = 1.01 \text{ MeV}; \mathrm{E}_\alpha = 1.78 \text{ MeV}(6\%) \\ ^7\mathrm{Li} + \alpha + \gamma(0.478 \text{ MeV}), & \mathrm{E}_{Li} = 0.84 \text{ MeV}; \mathrm{E}_\alpha = 1.47 \text{ MeV}(94\%) \end{cases} \tag{1.1}$$

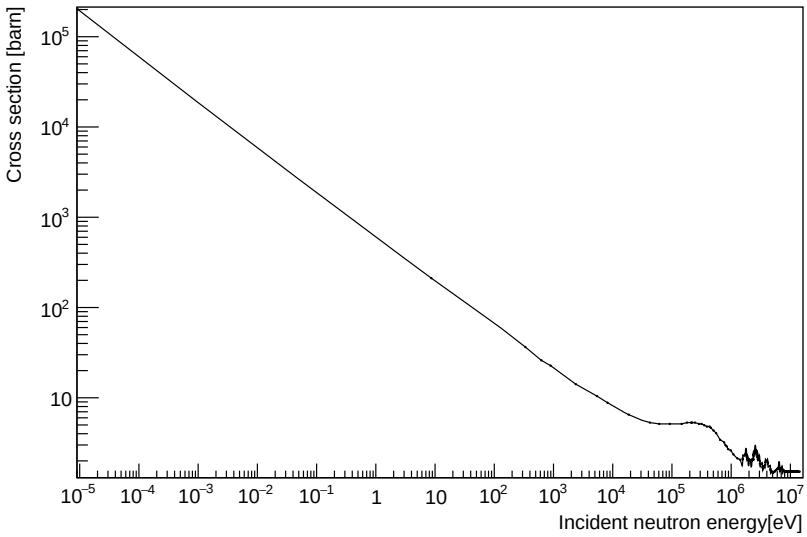

Figure 1.1: Neutron capture microscopic cross section of ^{10}B

The α particles and ^{7}Li-nuclei obtained from the capture reaction have respectively a LET of about 150 $keV\mu m^{-1}$ and 175 $keV\mu m^{-1}$, thus the path lengths of these particles in tissue are in the range of 4.5 μm to 10 μm which is comparable to the cell diameter and ensures that all the energy of these particles is deposited inside the cell where the capture reaction took place [1, 2]. Hence, BNCT effectiveness depends on the ability to selectively convey a higher quantity of ^{10}B in the neoplastic cells than in the healthy ones, thus leading to a greater number of capture reactions inside the tumour. Therefore, is extremely important to correctly estimate the ^{10}B concentration in tumour and healthy tissue to be able to evaluate a correct dose to the neoplastic cells while minimizing the dose to the normal ones.
BNCT treatment is able to selectively destroy malignant cells and as such could be in many cases more advantageous than other conventional and non-conventional treatments. To exploit its selectivity and further develop its clinical application the boronated compound administered to patients must be able to correctly target tumour cells. Moreover, since the major component of the dose delivered to the tumour comes from the ^{10}B neutron capture reaction, it is of great importance to be able to correctly estimate the concentration and the distribution of ^{10}B in the patient at the irradiation time.
The most important characteristics to take into account to have a good performing estimation method are the possibility to be as noninvasive as possible, to be able to perform *in-vivo* measurements in the patient and to be able to obtain the results within a time frame that allows to make clinical decisions to keep or optimize the treatment plan for the patient.
To such purpose many different methods of estimating the ^{10}B concentration have been developed and used in BNCT preclinical and/or clinical applications [3].

1.2 Current Methods for Boron Concentration Measurement in BNCT

The methods for the boron concentration measurement described in the following sections can be divided in two groups because they are either used to measure the ^{10}B concentration of samples or *in-vivo*. Therefore the first sections describe the techniques used on samples while the last sections take into consideration the methods that can be applied *in-vivo*.

1.2.1 Inductively Coupled Plasma Spectroscopy

Inductively Coupled Plasma-Atomic Emission Spectroscopy (ICPS-AES) also called Inductively Coupled Plasma Optical Emission Spectroscopy (ICPS-OES) is an emission spectroscopy. ICPS exploits the energy emitted by the excited

elements in returning to their ground states, where the atoms are excited by means of an inductively coupled plasma. The emitted wavelengths can be detected and used to find out the elemental composition of the sample, moreover the intensities of the wavelengths can be determined and used to quantify the elemental composition by comparison to a standard reference.
Another application of the Inductively Coupled Plasma Spectroscopy is the ICP-MS (Inductively Coupled Plasma-Mass Spectroscopy) which is a type of mass spectroscopy commonly used for it's high sensitivity for metals and some non metals thus making possible to determine them at concentrations below one part in 10^{12}. ICP-MS is also capable of distinguishing between isotopes of the same element thus making it a powerful tool to quantify separately the two stable isotopes of boron ^{10}B and ^{11}B
ICP-MS is one of the largely employed methods for boron estimation in serum, plasma, urine, saline, water and tissue.
Nonetheless ICP-MS has drawbacks due to some characteristics of elements such as boron, for example its tendency to absorb into glass thus requiring a validated procedure for sample preparation.
Once the sample is correctly prepared the ICP-MS is often preferred to ICP-OES, its advantages are a higher sensitivity, lower detection limit, i.e. 1 ppb to 3 ppb for biological materials and 0.5 ppb for human serum [4, 5, 6]. Moreover the simultaneous measurement of ^{10}B and ^{11}B ratio and total boron concentration in sample can be achieved, this is very important for biological boron tracer studies. Furthermore there is no need for the sample to be irradiated so it's free from the availability of a neutron source. The disadvantage of this method is that is destructive so it can not be used for an imaging of the boron distribution.
In 2001 Laakso et al.[7] compared ICP-MS and ICP-OES finding a strong correlation between the results and thus establishing that ICP-OES is a feasible method for BNCT because of its accuracy and high speed for boron determination.
ICP-OES has been employed for B concentration measurement in blood for patients [7, 8, 9, 10].

1.2.2 Neutron Capture Radiography

Neutron Capture Radiography (NCR) is a technique that gives a qualitative visualization of the boron distribution but can also be combined with other techniques to provide a quantitative evaluation of the boron concentration, for example in combination with a densitometric analysis. Moreover the ^{10}B concentration can be measured and spatially correlated with the stained tissue section by means of the spectroscopy of the charged particles emitted during the boron neutron capture reaction [3].
The procedure of NCR begins by cutting three adjacent tissue slices of 0.5 cm^2 from the same sample which was cryofixed using liquid nitrogen. The fixing

step allows to stop the ^{10}B carrier distribution and "photograph" the boron concentration in the tissues.
The first of the three samples are deposited on a Mylar disk to be used for charged particle spectroscopy [11], the second one is deposited on a glass plate for histological analysis by standard hematoxilin-eosin staining, (this sample is usually used to find out the percentage of tumour cells and healthy tissue), the third sample is deposited on a solid state nuclear track detector (SSTD) for imaging of the macroscopic boron distribution. The third tissue sample is then exposed to thermal neutrons thus giving start to the neutron capture reaction by ^{10}B and the α particles and the ^{7}Li-nuclei produced during the irradiation damage the nuclear detection film making it possible to see the tracks on the detector after a chemical etching in a dilute NaOH solution [12]. The macroscopic boron distribution in the sample is directly inferred from the tracks distribution in the detector. Last step is to superimposed the histological image and the map of the boron distribution, as showed in Fig.1.2.
The first sample that was deposited on a Mylar disk is placed in front of a

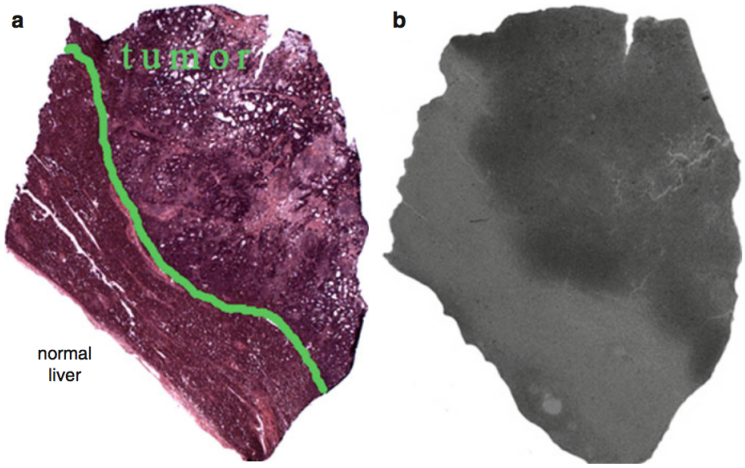

Figure 1.2: Histology (a) and neutron capture radiography (b) of a liver sample from a patient with liver metastases of colorectal adenocarcinoma after infusion of BPA [3].

silicon state detector in a vacuum container and irradiated with thermal neutrons thus inducing a neutron capture reaction in the ^{10}B and consequently emitting α particles and ^{7}Li-nuclei that reach the Si detector and are registered and counted. The energy distribution spectra recorded from the emitted particles is used to have a quantitative measurement of the boron concentration by means of equation 1.2.

$$^{10}B(ppm) = K\frac{C}{\eta\sigma\phi S}\frac{\Delta E}{\Delta(\rho x)} \tag{1.2}$$

In equation 1.2 K is the normalization constant, C represents the experimental counts in the energy range ΔE, η is the geometrical efficiency, σ is the

cross section of the boron neutron capture reaction, ϕ is the thermal neutron flux and $\Delta(\rho x)$ represents the tissue thickness where the alpha particles are produced and is calculated using their mass stopping power in tissue.
This method has an experimental error of $\pm 10\%$ and its lower detection limit is of 0.5 ppm due to the boron background concentration in tissue.
The advantage of this method is the ability to measure the boron concentration as well as to have an image of its distribution in a tissue slice thus correlating the macroscopic spatial information to the histology of the tissue. NCR has some drawbacks due to the impossibility of analyzing liquid samples due to the need of a vacuum, furthermore the technique needs a dedicated neutron source separated from the therapeutical beam and as such is difficult to employ in a clinical facility.

1.2.3 High Resolution Alpha Autoradiography

In 1956 Edwards[13] reported the first attempts at imaging the boron distribution in a sample by means of a neutron induced nuclear reaction. Solares at al.[14, 15] and Yam et al. [16] were later able to use a variant of Edwards' approach to reach cellular level spatial resolution. The technique is fundamentally based on the ^{10}B neutron capture reaction described at the beginning of this chapter.
The ability of mapping these particles implies the possibility to find the distribution of boron in the sample. To such purpose the technique exploits the ability of the produced particles to interact with some solid state track detectors like Lexan films thus leaving tracks on it that can be used to find the boron distribution in the sample.
The procedure consist in removing and freezing tissue samples after the boron carrier administration and subsequently cutting 2 μm thick slices of the frozen sample and mounting them on Ixan and Lexan films on top of a quartz glass slide.The system thus created is irradiated with thermal neutrons. After the irradiation the samples is histologically stained and the quartz glass is moved next to sample thus exposing the Lexan films that, as previously said, have now tracks on them due to the interaction of the α particles and the ^{7}Li-nuclei produced during the irradiation of ^{10}B.
To be able to see the tracks the films are chemically etched and the Ixan film acts as a barrier to protect the sample during the etching process. In the end the sample system is studied with a microscope, acquiring microphotographs of the tracks superimposed on the stained sample (an example is shown in Fig.1.3).
The system has to be calibrated but once it has been done the track density can be related to absolute boron concentration in the tissue thus providing a quantitative analysis of the boron concentration.
This technique has very good quantitative results that can be superimposed on the image to have also a qualitative assessment of the boron concentration

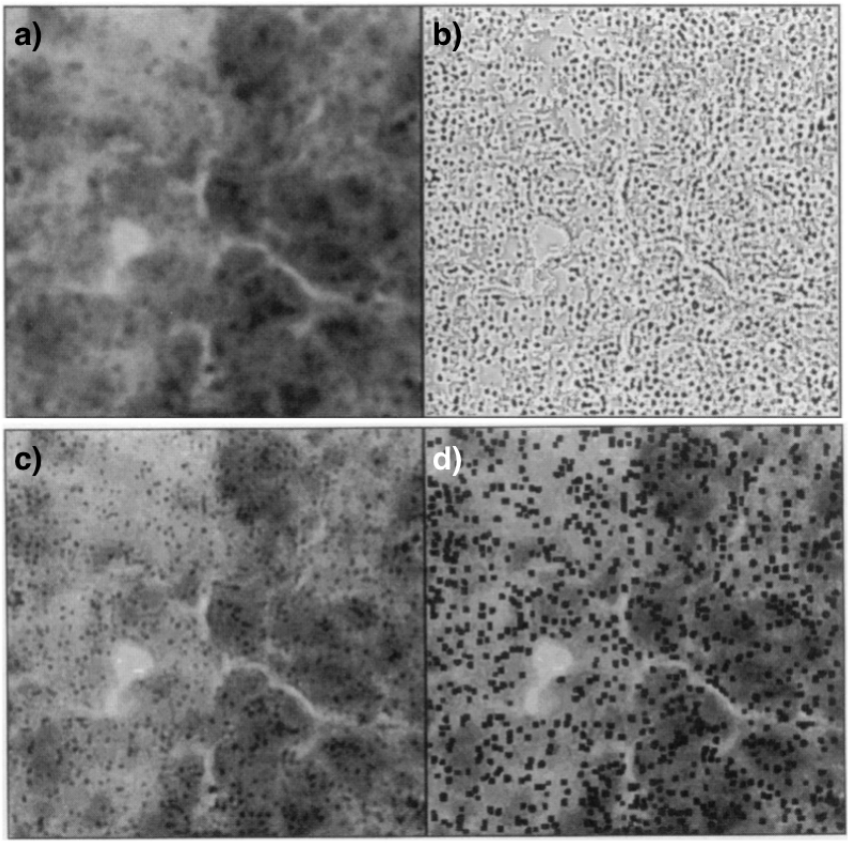

Figure 1.3: Two μm thick High Resolution Autoradiography of a murine brain tumour section. (a) Original image after low-pass filtering, (b) Particle track image, (c) Original image, (d) Superimposition of image (a) and the fully extracted and enhanced particle track image [17].

but it is very complex to apply and quite time consuming, and thus it is not possible to use it during clinical patient treatments.

1.2.4 Charged Particle Spectrometry

Charged particle spectrometry (or α spectrometry) was developed as a technique to evaluate the boron concentration in tissue. The main characteristic of such technique is the ability to quantify the boron content in tumour, healthy and necrotic tissue [18].
Charged particle spectrometry is based on the spectroscopy of the ^{10}B capture reaction products such as ^{7}Li and α particles. The charged particles produced by the ^{10}B capture reaction are collected using a thin silicon detector and their spectrum is used to calculate the boron concentration in the sample.
The samples are taken from biopsies of treated animals or patients and divided in 1 cm^3 cubes and frozen with liquid nitrogen. These smaller samples are then

cut in 70 μm thick sections and deposited on a 100 μm thick Mylar disks.
The samples are then positioned in a rotating holder, a cap is positioned on the top of the sample housings, the cap has holes of diameter 0.4 cm that act as collimators. The holder is then screwed to the chamber where a thin silicon detector is fixed as can be seen in Fig.1.4.
The chamber is then connected to a pump to keep the setup under vacuum. The whole system is then irradiated with neutrons and the spectra are acquired.
The obtained spectra are characterized by Gaussian peaks corresponding to

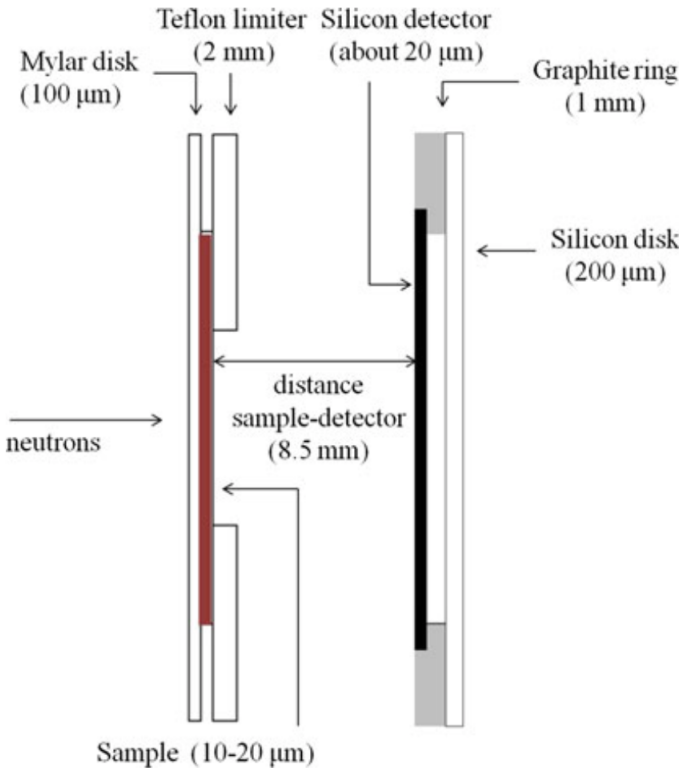

Figure 1.4: Setup of the charged particle spectrometry system where the Mylar disk with the sample is positioned in front of a thin silicon detector [18].

α-particles and Li ions produced by the ^{10}B neutron capture reaction. The thin silicon detector is able to separate the two peaks due to alpha particles but not the peaks due to the lithium ions since its energy resolution is 2.5%. Therefore the α particles are chosen as reference to calculate the ^{10}B concentration in the sample.
To consider only the α particles an energy interval ΔE from 1100 keV to 1350 keV is chosen. The integral of the histogram in ΔE corresponds to N, the number of α particles that left the tissue sample, and thus can be directly connected to the boron concentration in the tissue.

If K is the number of events that took place in a time interval Δt and per ΔE (see Eq.1.3) then we can find the nuclear boron density in the sample from Eq.1.4.

$$K = \frac{N}{\Delta E \cdot \Delta t} \tag{1.3}$$

$$n = \frac{K}{\eta \cdot \sigma \cdot \phi \cdot S} \frac{\Delta E}{\Delta x} \tag{1.4}$$

In Eq.1.4 K is the value measured from the experiment, η is the measurement efficiency, σ is the microscopic cross section of the boron neutron capture reaction, ϕ is the thermal neutron flux, S is the surface of the sample while Δx is the sample thickness.
Finally the boron concentration in the sample is given as the ^{10}B mass in the sample volume over the tissue mass in the sample volume ($^{m_B}/_{m_t}$) and can be calculated using Eq. 1.5, where N_A is the Avogadro number and A_w is the atomic weight of boron.

$$\frac{m_B}{m_t} = \frac{K}{\eta \cdot \sigma \cdot \phi \cdot S} \cdot \frac{\Delta E}{\Delta(\rho x)} \cdot \frac{A_w}{N_A} \tag{1.5}$$

The error associated with this procedure is about 20% mostly due to the limited precision of the sample thickness Δx.
Main advantage of this technique is the possibility to measure macroscopic sample and to separate the boron concentration values for tumour cells, healthy and necrotic tissues. Moreover it is possible to couple α spectrometry with neutron autoradiography and histology to have also an image of the boron distribution but this procedure is very complex and time consuming. Furthermore to perform an α spectrometry the sample must be obtained from a biopsy after boron administration. For these reasons it is difficult to use α spectrometry in clinical BNCT treatments.

1.2.5 Nuclear Magnetic Resonance and Magnetic Resonance Imaging

Nuclear Magnetic Resonance (NMR) and Magnetic Resonance Imaging (MRI) can be used to detect boron and moreover they can detect both ^{10}B and ^{11}B nuclei. NMR is a quantitative method where the signal is proportional to the amount of nuclei detected in the sample[19]. Also MRI can be used as a quantitative method. Since the image intensity is proportional to the amount of nuclei in each voxel it is possible to compare the image to a reference sample and thus quantify the boron concentration from the MRI image.
The procedure for NMR consists in placing a sample (or patient) in a magnetic field and then altering the equilibrium of the sample particles' spins by means of a properly tuned radio-frequency coil (RF). The particles' spins will then

go back to their equilibrium emitting signals at their characteristic resonance frequencies. The RF delivers energies in short pulses of the order of 10^{-3} to 10^{-6} s, the energy range is such as to be absorbed by the nuclear spins because it matches the gaps in energy levels corresponding to different spin states.
The signals emitted during the spins return to equilibrium, once the RF has been turned off, can be detected and analyzed both to create a spectrum or an image.
After the pulse, the signals from each spin have the same phase and the total signal is detectable. The return to equilibrium follows an exponential law characterized by a time constant T_1 called spin-lattice relaxation time. This constant is short for ^{10}B and ^{11}B used for BNCT, therefore it allows to repeat many signal excitations in high rate, thus making it possible to have many independent inputs to create images with a good signal to noise ratio.
While returning to equilibrium there is also an exponential loss of coherence ruled by the time constant T_2 called spin-spin relaxation time which is also very short for ^{10}B and ^{11}B especially in tissue. To avoid losing part of the signal the inevitable technical delay between signal excitation and detection must be shorter than T_2. Since for boron the spin-spin relaxation time is very short part of the signal could be lost thus decreasing the signal to noise ratio and creating difficulties in the correct quantification of boron in the sample.
NMR and MRI, as previously said, are quantitative method but there is a setback in their use for boron quantification for BNCT. The T_2 connection to the correct quantification of boron and its dependance on molecular mobility makes it possible to use these techniques only in liquid or liquid-like samples thus creating problems for *in-vivo* experiments.
The main application of BNCT-MRI would be for the real time monitoring of the boronated compound administered to the patient before the neutron irradiation. Although the BNCT-MRI technique has not been used on patients during BNCT treatment [20], many promising results have been obtained when the technique has been applied on small animals [21, 22].

1.2.6 Positron Emission Tomography

Positron Emission Tomography (PET) is a diagnostic modality that allows the physician to monitor the biological processes inside the patient body. PET is a technique based on the use of a positron emitting radio-tracer linked to a labeled molecule able to target specific types of cells, i.e. tumours [23].
PET in BNCT can be exploited by linking the radio-tracer to the boronated drug used for therapy thus helping to answer one of the most important questions in BNCT that is the correct assessment of the ratio of concentrations between boronated drug into tumours and surrounding normal tissues.
The radio-tracer emits 511 keV gamma rays that are collected by a ring of detectors positioned around the patient, the signal is then corrected for self attenuation, spurious events and scanner efficiency calibration yielding in the

end to a quantitative measurement of the radio-tracer distribution present in the scanned Field of View (FOV). The acquired data can then be displayed as a 2D or 3D image. BNCT-PET images serve as *in-vivo* analogues of autoradiographes.
To quantify the radio-tracer distribution many methods have been developed and validated such ad Standardized Uptake Value for semi-quantitative measurements, Multiple Time Graphical Analysis and full Compartmental Models. Compartmental modeling is based on the conservation of matter through different compartments such as vascular system, tissues and intracellular space thus the fate of the radio-tracer in the patient body can be described in mathematical form by means of differential equations. A typical compartmental model has three or four compartments and it describes the transport of the tracer.
Imahori et al.[24, 25] amd Kabalka et al.[26] studied and validated the *in vivo* pharmacokinetics of Fluorine-18-Boronophenylalanine-Fructose (L-^{18}F-BPA). Both groups concluded that the concentration of boron in the tumoural tissue gained by PET imaging was close enough with the measurement done directly in surgical specimens.
Main advantage of the PET method is the possibility to quantitatively measure the boron tumour/healthy ratio thus personalizing the therapy for each single patient and achieving a better therapeutic effect.
Nonetheless PET imaging for BNCT has some drawbacks due to the necessity to link the radioactive label to each boron carrier, to date this has been successfully done just for BPA. Moreover the PET imaging can not be performed during the treatment and as such gives information only on the boron concentration and not directly on the dose given to the tumour. Moreover the amount of L-^{18}F-BPA administered to the patient for the PET exam is much lower than the therapeutic amount of BPA usually employed in patients thus creating some uncertainty in the estimation of the Boron dose when using BNCT-PET.

1.2.7 Prompt-Gamma Ray Spectroscopy

Prompt Gamma Ray Spectroscopy (PGS) is based on the possibility to detect the 478 keV gamma rays emitted by the ^{10}B capture reaction in the 94% of the cases (see Eq. 1.1). The gamma emission is proportional to the reaction rate of the boron capture reaction and as such is linked to the boron concentration [27, 28]. PGS can be used as non invasive method to measure the boron concentration during the treatment.
To be able to detect the 478 keV gamma ray a detector with high energy resolution is needed. Such detector can be used to also monitor the 2.223 MeV gamma emitted by the Hydrogen capture reaction which gives information on the thermal neutron fluencies.
In PGS the line due to the boron capture reaction must be compared to refer-

ence samples to be able to correctly estimate the boron concentration.
PGS, for samples down to 1 ppm, allows a fast measurement of about 5 min per sample with a 0.5ppm standard deviation and it is not destructive for the analised samples of blood, tissue and urine.
Another interesting fact is that the PGS facility can be automatised completely and such can be exploited all day long for the sample measurements, an example of a PGS configuration can be seen in Fig.1.5.
The drawbacks of this technique can be summarized in the necessity to use

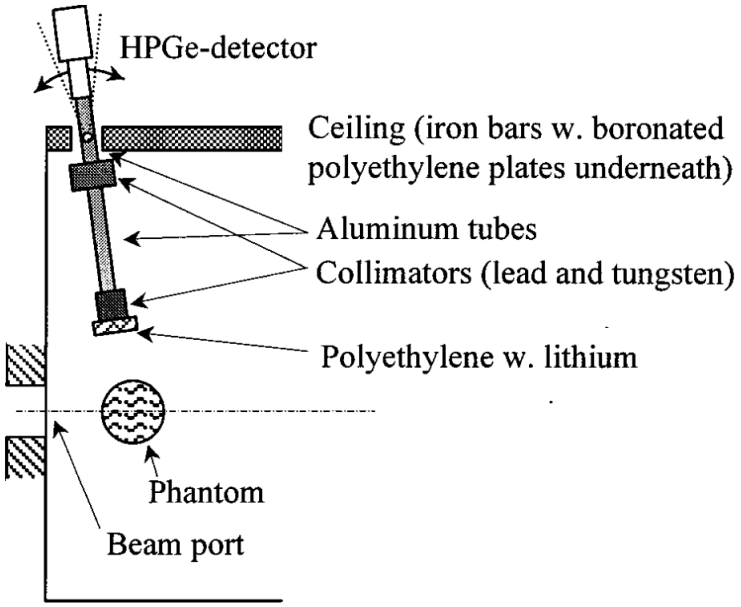

Figure 1.5: Side view of the PGS configuration, called The Gamma-Ray Telescope, installed at the BNCT facility in Petten, The Netherlands [29].

relatively large samples and the impossibility to study inhomogeneities that can happen in the boron distribution in the sample and which can be relevant for BNCT treatment.

1.3 New Perspectives: SPECT for BNCT

To prepare a treatment plan for a patient undergoing BNCT the clinical dosimetry needs to take into account the boron concentration and distribution inside the tumour as well as the neutron flux.
The neutron flux used to irradiate the tumour is measured with a method that relies on the activation of foils which takes from 15 to 30 minutes and as such can not be used on-line during the patient treatment.
The measurement of the boron concentration can be done with one of the methods previously described or a combination of them. Although the estima-

tion made by such methods are currently used in therapeutic BNCT they are not personalised for each patient and moreover are not on-line but have to be performed before and/or after the treatment. To improve BNCT efficacy it is fundamental to have a tool that is tailored on each patient and can be reliable to estimate the dose not just from the blood but directly in the tumour.
In 2000 Kobayashi et al. [30] proposed a Prompt Gamma-Single Photon Emission Computed Tomography (PG-SPECT) to measure the ^{10}B dose distribution during BNCT treatment.
The PG-SPECT system is based on the possibility to detect the 478 keV photon emitted in the 94% of the cases during the boron capture reaction as shown in Eq.1.1

These gammas emitted during the reaction can be directly linked to the boron concentration and the neutron flux on the tumour since the number of gammas emitted per second is directly proportional to the ^{10}B reaction rates due to the neutron capture, and thus PG-SPECT is a clever tool for BNCT on-line dosimetry.
Eq.1.6 shows that the dose D due to ^{10}B capture reactions is proportional to the local concentration of ^{10}B (n_B) and to the thermal neutron flux ϕ, thus the measurement of the number of 0.478 MeV gamma ray would allow a direct estimation of the delivered dose in the tumour avoiding the difficulty of measuring ^{10}B concentration and neutron flux as separated quantities.

$$D \propto \int n_B \sigma \phi dV \tag{1.6}$$

Moreover using a SPECT technique opens the possibility to acquire an image of the boron capture reaction spatial distribution in the patient which would give both a qualitative information and a quantitative one of the spatial dose distribution due to the boron capture reaction.

1.4 Rationale for SPECT imaging

SPECT is an imaging technique based on the use of a labelled radioisotope such as ^{99m}Tc which will be tailored on the target and will emit a single gamma ray per nuclear disintegration. The radioisotope is commonly attached to a physiologically active agent that can be used to identify specific functions or abnormalities, thus SPECT imaging gives an understanding of the physiological functions of the body. The monoenergetic gamma rays emitted by the radioisotope are acquired by an array of detectors that can be rotated around the patient. The acquired data is used to reconstruct a 2D or 3D image of the radioisotope distribution in the patient. The final result is a map of the spatial distribution of the radioisotope and therefore an image of the physiological distribution of the targeted functions or abnormalities [31].

The SPECT system can be implemented as a limited-angle (or longitudinal) imaging or as a transaxial (or transverse section) imaging. In the first case the angular range of detection is limited by the patient anatomy thus leading to blurred information in the images and to the necessity of deblurring methods such as deconvolution or iterative reconstruction techniques. The obtained images are parallel to the detector face and give mainly a qualitative information due to the problems of the limited angular view, therefore this technique was gradually replaced by transaxial imaging. In this last method the detectors rotate around the body or are placed in a ring to achieve 360° sampling. The reconstructed images lay in a plane orthogonal to the detector face. The two methods are represented in Fig.1.6 and differ mostly on the density of the data that can be gathered thus requiring different image reconstruction techniques.

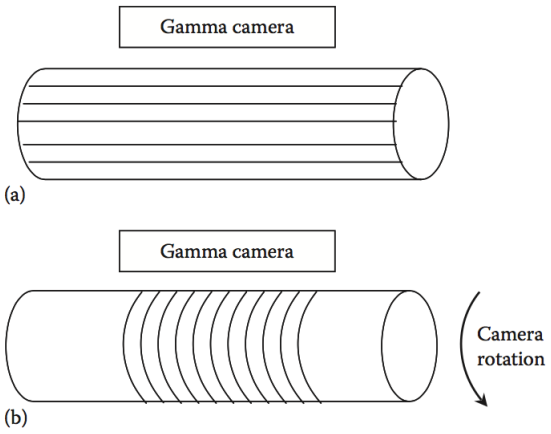

Figure 1.6: Orientation of the imaging planes in longitudinal (a) and transaxial (b) SPECT [32].

Transaxial imaging is the most common method used for SPECT, each projection in position x' and at angle θ $g(x', \theta)$ can be obtained by an attenuated Radon transform (1.7) where $f(x, y)$ is the two dimensional distribution of the radioactivity, $\mu(u, v)$ is the two dimensional distribution of the linear attenuation coefficients and the integrals are intended over s along the whole length of the line of response (LOR) and over l along the LOR from each (x,y) in the object to the detector, and thus taking into account the photon attenuation. The process of the Radon transform for one slice can be seen in Fig.1.7.

$$g(x', \theta) = \int f(x, y) e^{-\int \mu(u,v) dl} ds \tag{1.7}$$

The 1D profiles obtained with the Radon transform can be displayed as a function of the rotation angle, this graph is called a sinogram as shown in Fig.1.8. The sinogram is then used to reconstruct the SPECT image.

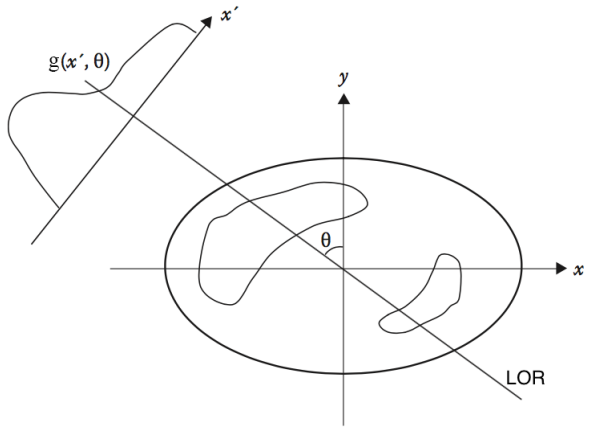

Figure 1.7: Image profile of radioactivity for a single transaxial slice of an object with two radiotracer deposition areas [32].

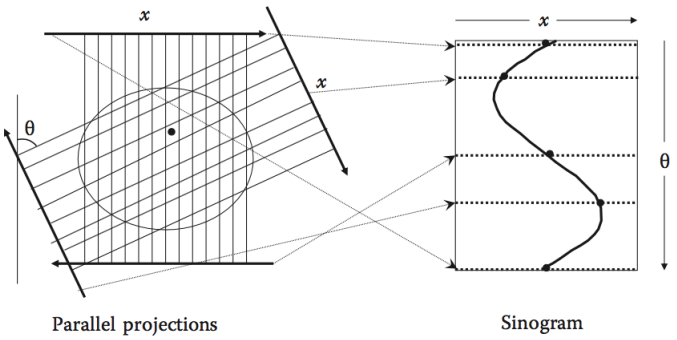

Figure 1.8: sinogram plot from a set of 1D profiles [32]

1.4.1 Reconstruction Algorithms

The choice of the image reconstruction algorithm is a fundamental one for the SPECT system. The most commonly used algorithms are filtered backprojection (FBP) and iterative algorithms such as maximum likelihood expectation maximization (MLEM).
At first the projection data expressed by equation Eq.1.7 is acquired by the measurement system. Fig.1.9 shows a discrete projection of a 3x3 image acquired at two angles. The result is a 2x3 sinogram where the rows correspond to the projection angles and the columns are the three point of measurement on the detector.
The backprojection method aims to reconstruct an image $b(x, y)$ from the integral of $g(x', \theta)$ along $d\theta$ as expressed by equation 1.8. Fig.1.10 shows a simplified example of the backprojection.

$$b(x, y) = \int g(x', \theta) d\theta \tag{1.8}$$

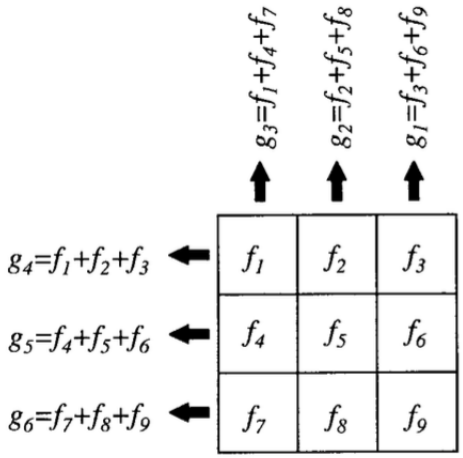

Figure 1.9: Principle of projection for one 3x3 slice at angle 0° and 90°. The value in each bin is the sum of values of the pixels that project onto that bin. Result of the projection is a sinogram with 2 rows, whose values are (g_3, g_2, g_1) and (g_4, g_5, g_6) [33].

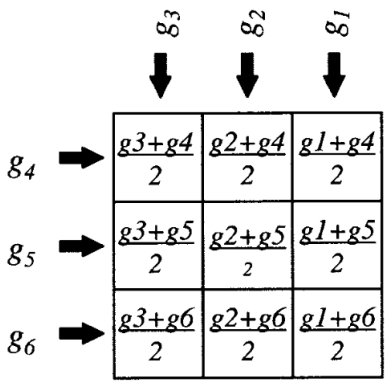

Figure 1.10: Principle of backprojection for a 2x3 sinogram. The value in each pixel is the sum of values of the bins that can receive photons from that pixel at each angle and it's divided by the number of rows of the sinogram [33].

Different images could have the same projections if they are acquired with a small set of angles thus to perfectly reconstruct an image an infinite number of projection would be required. Moreover if the number of acquired angles is smaller than the matrix size a star artefact can be seen in the reconstructed image. To reduce the artefact presence it is important to have a high number of projection as shown in Fig.1.11. Moreover an important step of the reconstruction algorithms is the possibility to apply some filters to the image. In the case of FBP the ramp filter is part of inverse Radon transform. Each image can be divided into several frequency components using the Fourier Transform, then each frequency could be weighted differently and in the end they could be all added together to build once again the original image. The filtering can

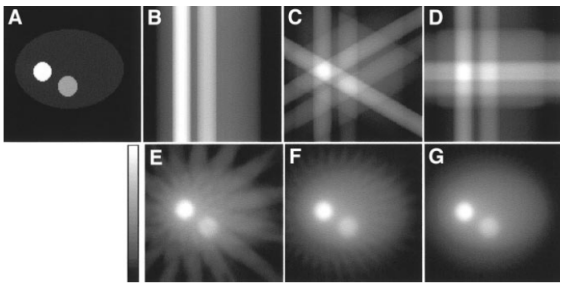

Figure 1.11: Backprojection algorithm and star artifacts. A: image used to create projections. B to G: 1, 3, 4, 16, 32 and 64 projections equally distributed in 2Π [33].

improve the image reconstruction, for example lowering the weight of the low frequencies which usually tend to blur the image or reducing the amplitude of the low frequencies which can conduct to an image with better edges definition. Moreover noise predominates in the high frequencies thus making it useful to apply a filter able to decrease both the low and high frequency contribution. In FBP usually the filtering step is applied on each line of the sinogram and then the backprojection is applied.
Fig.1.12 shows the most commonly used filters in FBP.
FBP is very efficient from a computational point of view but it is based on

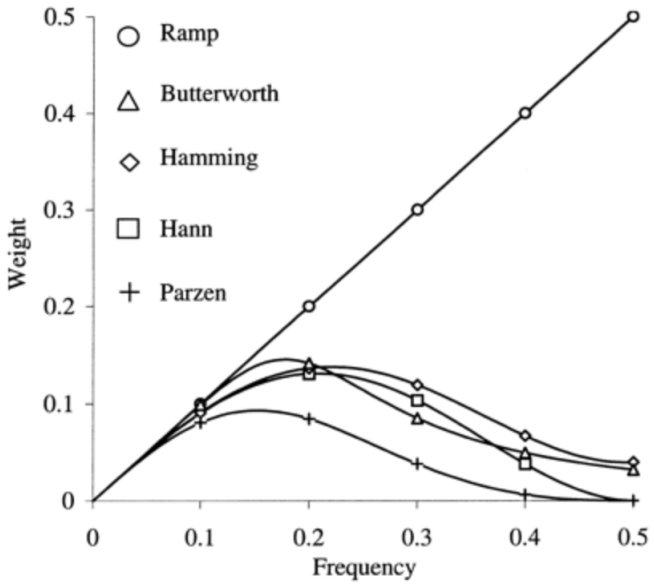

Figure 1.12: Filters commonly used in FBP [33].

the assumption that the projections are perfectly representative of the object which is not true due to attenuation of the photons in the patient and the decreasing spatial resolution as the patient-collimator distance increases. To improve the reconstruction in SPECT imaging it is possible to use iterative

methods. Although these algorithms are less computational efficient they take into account the initial activity distribution in the patient thus achieving a better image quality.
Iterative reconstruction algorithms aim to find the vector f to solve $g = Af$, where A is the system matrix, to do so the iterative approach is used by making a first estimation which will be compared to the projections. The comparison result will then be used to modify the estimation thus creating a new one. Various algorithms use different comparison parameters and unique ways to modify the first estimate.
The first step of each iterative algorithm is to make a first estimate, for example initializing the image to 0 or 1 or even by using the mean pixel count as a parameter for all the pixels, then the chosen comparison method is applied.
The most commonly used iterative algorithm in SPECT is the MLEM algorithm where g is the vector of values of the sinogram, A is a matrix and f is the unknown vector representing the image reconstruction.
The algorithm assumes that the raw data g representing the radioactive disintegrations follows the Poisson distribution, as such there is not a singular solution f corresponding to a unique measurement g. The aim of the MLEM algorithm is to find $\overline{f}$ which, with the highest likelihood, represents the mean number of radioactive disintegrations in the image that can produce sinogram g.
The algorithms exploits the Poisson law and it is divided in two steps, the first creates the formula of the likelihood of any $\overline{f}$ reconstructed image (estimation step) and the second is the maximization step which looks for the image with the highest likelihood to correctly estimate g. Eq.1.9 was developed by Lange and Carson and represents the MLEM algorithm [34].

$$\overline{f}_j^{(k+1)} = \frac{\overline{f}_j^{(k)}}{\sum_{i=1}^{n} a_{ij}} \sum_{i=1}^{n} \frac{a_{ij} \cdot g_i}{\sum_{j'=1}^{m} a_{ij'} \overline{f}_{j'}^{(k)}} \qquad R_i = \frac{g_i}{\sum_{j'=1}^{m} a_{ij'} \overline{f}_{j'}^{(k)}} \tag{1.9}$$

The ratio between the current estimation of the counts and the mean measured counts in bin i is represented by R_i and the backprojection of such ratio for pixel j is $\sum_{i=1}^{n} R_i \cdot a_{ij}$. Eq.1.9 must be applied pixel by pixel but can also give an interpretation of the process for the whole image by means of Eq.1.10 [33].

$$\text{Image}^{(k+1)} = \text{Image}^{(k)} \cdot \text{Norm. BP of} \Big(\frac{\text{Measured projections}}{\text{Projections of image}^{(k)}} \Big) \tag{1.10}$$

Both FBP and MLEM algorithms are widely applied for SPECT image reconstruction. As previously said the first is faster than the MLEM algorithm and computational efficient though the image quality could be lower. A comparison of the two methods can be seen in Figure 1.13 and an image reconstruction comparison can bee seen in Fig. 1.14.

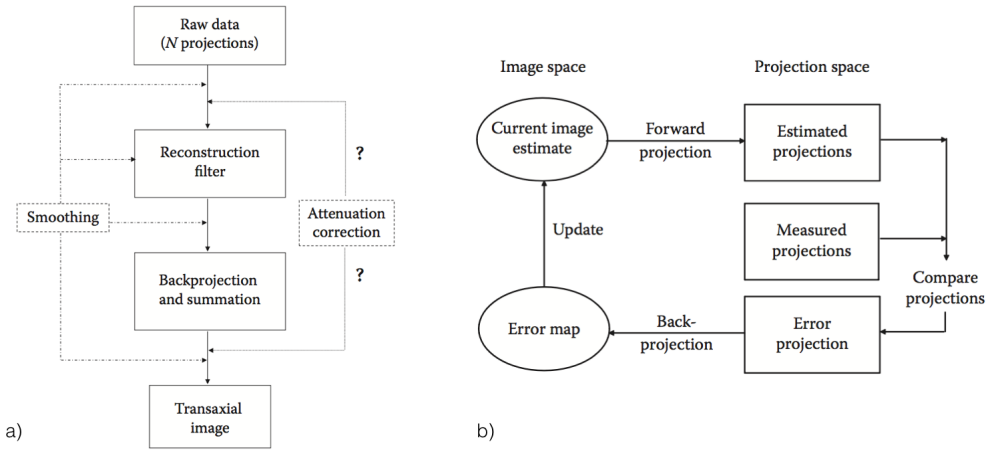

Figure 1.13: Flowcharts for FBP (a) and MLEM (b) algorithms [32].

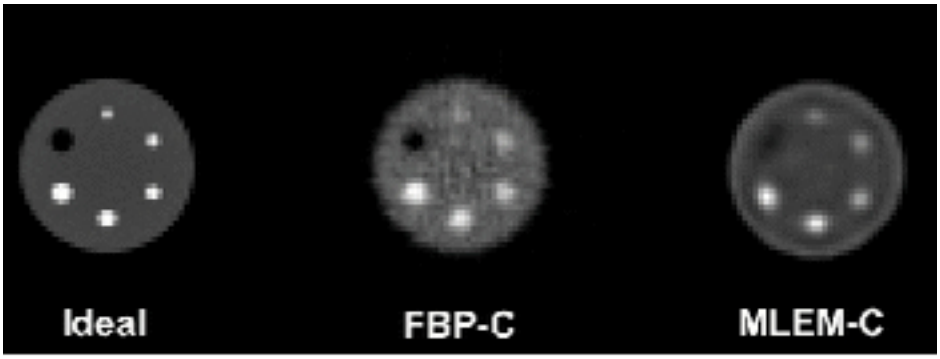

Figure 1.14: Comparison of FBP and MLEM algortihms in a Monte Carlo simulation [35].

1.4.2 Hardware development for SPECT

SPECT systems are usually developed using one or more gamma-camera heads on a rotating gantry. This detectors need to be electronically and mechanically stable and have a very good uniformity and spatial linearity. Usually the gamma-cameras are based on inorganic scintillators such as NaI(Tl) and are used with a set of collimators that are changed based on the imaging purpose. The system as such is also shielded with lead and the photomultiplier tubes must be shielded from any possible influence of magnetic fields which could change the trajectories of the electrons, therefore the whole system has a considerable weight and needs to be rotated carefully and precisely thus requiring a state of the art mechanical and computer system.
Since solid state detectors have interesting properties such as an higher energy resolution than scintillators they have been studied to be used as gamma cameras [36].
Moreover solid state detectors are more compact and thus weight less and they don't need to be shielded for possible magnetic fields, as such they can be

used to reduce the limitations due to the weight of the system. Some special-purpose SPECT system have been studied using solid state detectors such as the BNCT-SPECT systems.
The properties of solid state detectors will be further discussed in the following chapters.
To achieve the best possible image quality the hardware development and rotation is fundamental and some parameters has to be taken into account, such as the geometry of the collimator, the radius of rotation of the gantry and the number and range of the angular views which are also connected to the duration of the SPECT scan and the administered activity of the radio-tracer. Moreover the pixel size of the projections and the reconstructed image are fundamental.
Usually the collimator choice is strictly connected to the radionuclide used and the purpose of the SPECT system, e.g. the low energy high resolution (LEHR) collimator is recommended for a high count-rate study.
Another important parameter is the radius of rotation of the cameras, which is also dependent on the collimator type and length since it is defined as the distance between the outer surface of the collimator and the axes of rotation. To improve the imaging performances the radius of rotation should be the minimum possible value taking into account patient size and hardware requirements.
SPECT systems can be developed as a 180° or 360° scanning devices, the first option is more commonly used for cardiac imaging while the second one has better performances when the imaging interest rests on larger and deeper seated organs. In both cases it is also important to have a high number of angular steps even though increasing the number of steps diminishes the counts per view thus leading to the choice between lower counts or higher scanning time.
It is clear that all the hardware requirements are strictly connected and have to be taken carefully into account. The studies for state of the art gamma-camera SPECT system have aimed to achieve a spatial resolution smaller than 10 mm, to such purpose the focus has been the reduction of the distance between the camera and the patient.

1.4.3 Spatial Resolution

The spatial resolution is a quantity commonly used to appraise the image quality of any imaging system.
Spatial resolution represents the accuracy with which an object can be reproduced, for example the amount of details that can be seen in the image.
Usually the assessment of this quantity is made using high doses of X or gamma rays to lower the noise influence on the image.
The spatial resolution is dependent of the pixel size used for the imaging system since that is the theoretical limit on the smallest image that the system can resolve, but it is not the only parameter affecting the quality of the recon-

structed image.

To study the spatial resolution of an imaging system the point spread func-

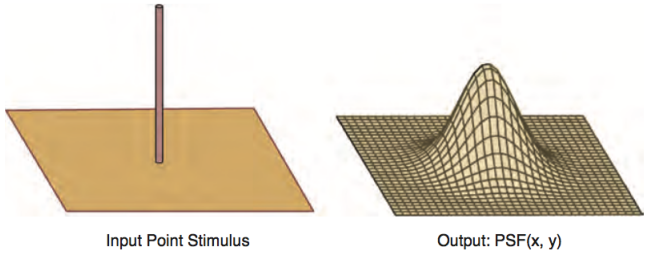

Figure 1.15: On the left: Input point source. On the right: response of the imaging system, PSF function [37].

tion (PSF) is commonly used. PSF is also called impulse response function and it consists in the study of the response of the system when a point source is used. Fig.1.15 shows an example of a PSF function obtained after sending to the imaging system an input obtained by a point source, the full width half maximum (FWHM) of the PSF function is the quantity most often used to describe the spatial resolution. The input source has an infinitely small diameter thus the ideal response of the system should be an equally small FWHM of the PSF. Since the real system has some physical constraints the FWHM shows the limits of the imaging system and as such its spatial resolution.
In a SPECT system the image spatial resolution is about 7 mm [38].

1.5 Current applications of SPECT for BNCT

SPECT imaging has become an important research field in BNCT in the last 30 years. As previously discussed a BNCT-SPECT system would be based on the possibility to detect the 478 keV photon emitted in the 94% of the cases during the boron capture reaction (see Eq. 1.1)
The gamma emitted during the reaction can be detected and used for a SPECT imaging from which a measure of the ^{10}B dose distribution can be obtained, giving both a qualitative information and a quantitative one.
Kobayashi et al. [30], Murata et al. [39] and Valda et al. [40, 41] have studied the feasibility of a BNCT-SPECT and found a set of minimum requirements that should be met to obtain a state of the art specific imaging system.
Murata et al. reported the main difficulties that stand on the path of a high performance BNCT-SPECT system. The presence of hydrogen in the human body gives way to the $^1H(n,\gamma)^2H$ reaction from which a 2223 keV gamma-ray is emitted thus creating a high background. Moreover the detector operates in a mixed background field of neutrons and gammas due to the nature of the neutron source thus it needs to be shielded to avoid radiation damage and to

suppress the gamma signals not coming from the patient. Furthermore the $^1H(n,\gamma)^2H$ gamma rays and the ones coming from the irradiation field could interact in the detector shielding or on the collimation system producing annihilation gammas which energy is close to the 478 keV gamma ray of interest making the background reduction quite important.
Such problems set some parameters that should be taken into account when working on a BNCT-SPECT system:

1. The detection time must be set under 30 minutes
2. The statistical accuracy of the measurements should be at least few percent (at least 1000 counts per detector)
3. The detector must have a high energy resolution and efficiency at 478 keV thus suppressing the 2223 keV peak
4. The spatial resolution should be around 2 mm

A similar study has been carried out by Kobayashi et al. reaching some similar results. They also considered a measuring time of 30 minutes but they accepted a statistical error of about 10%, corresponding to 100 counts per detector. To be able to have such statistical error they calculated a required thermal neutron flux on the sample of $5 \cdot 10^8$ n cm^{-2} s^{-1} with a minimum ^{10}B concentration of 10 ppm, leading to a minimum 478 keV gamma yield of $1.1 \cdot 10^6 n/s$. Moreover they set a minimum voxel size of 1x1x1 cm^3.
Valda et al. studied the possibility to use a SPECT system in an accelerator based BNCT facility (A-BNCT). They took into account that the measured dose delivered to a brain tumour during A-BNCT treatment is 40 RBE-Gy which, considering the mean energy per capture reaction, would correspond to $2 \cdot 10^9$ photons cm^{-3}. This result does not take into account the attenuation due to the soft tissue which would amount to the 37% of the photons. They also considered that the statistical fluctuation of the results should be less than 10%. Moreover they considered a tumour size of 1 cm^3 thus obtaining that 5 arrays of $LaCl_3$(Ce) detectors, with their collimation systems, should be employed at 4 different angles to obtain a statistically good image reconstruction at mid-time during the treatment.
To build a proficient BNCT-SPECT system such constraints should be taken into account. In fact using the previously studied parameters Minsky et al. were able to reconstruct the first tomographic image of the neutron capture rate in a BNCT facility [42].
The choice of the detector is also fundamental. Kobayashi et al. studied a high-purity Germanium detector (HPGe) and a Cadmium-Telluride detector (CdTe), the characteristics of the two semiconductor devices can be seen in Table.1.1. HPGe detectors have an energy resolution and efficiency that is sufficient for the BNCT-SPECT system requirements but they need a large

Material	Working T (K)	Atomic Number	Density (g/cm^3)	Energy gap (eV)	Electron mobility ($cm^2/V \cdot s$)	Hole mobility ($cm^2/V \cdot s$)
Ge	77	32	5.33	0.74	3900	1900
CdTe	300	48-52	6.21	1.47	1050	80

Table 1.1: Characteristics of HPGe and CdTe semiconductors

effective volume and cooling with liquid nitrogen thus being quite bulky and less advantageous for an on-line dosimetry application. CdTe detectors have a larger band gap thus being employable at room temperature and their size is quite smaller and therefore easier to use in a treatment room. Even though the efficiency of the CdTe detectors is not as high as the HPGe detector.
Murata et al. also studied the feasibility of a system based on CdTe semiconductor detectors simulating crystals with different dimensions and concluded that the best option is to use a thick crystal that allows for the best detection efficiency for the 478 keV peak while keeping the same efficiency for the 2223 keV peak.
The results seem to suggest the use of a thick CdTe or CdZnTe detector as the base element for a BNCT-SPECT imaging system. In this thesis we chose to study a CZT detector due to its ability to work at room temperature. We studied the detector from both a computational and an experimental point of view to establish its feasibility.

Chapter 2

Properties of a CdZnTe detector

2.1 Introduction to semiconductor detectors

Semiconductor detectors have been the focus of many studies in the last years. They are of interest in many fields mostly as an alternative to commonly used gas detectors and scintillators. Semiconductor detectors offer the possibility to have a compact system with high energy resolution and imaging qualities. Traditionally the semiconductors used for radiation detection were silicon and germanium but more recently the studies have shifted on new compound semiconductors that are composed of elements from groups III and V, e.g GaAs, or from group II and VI, e.g. CdTe, of the periodic table. Table 2.1 shows some properties of the most common semiconductor detectors.

Our focus lays on the compounds from groups II and VI which generally have a wide band gap, compared to Si and Ge, thus being able to work at room temperature. Furthermore their high atomic number and density ensures a high detection efficiency.

In all semiconductor detectors the photon interaction inside the material releases energy converted into electron-hole pairs that are collected using an external electric field. The drift of the electron-hole pairs toward respectively the anode and the cathode induces the electronic output signal.

The photon interaction in the material is characterized by three main processes. Photoelectric absorption is the most interesting for spectroscopy because the photon releases all its energy to an atomic electron that induces a signal proportional to the initial gamma energy. Photoelectric effect has an interaction cross-section that increases as the atomic number of the material as $Z^4 - Z^5$, therefore semiconductors with a high atomic number are preferable for spectroscopic purposes.

Compton scattering is another process due to the interaction of photons in the matter and consist in the transfer of part of the initial gamma energy to

Material	Ge	Si	GaAs	CdTe	$Cd_{0.9}Zn_{0.1}Te$	HgI_2
Atomic Number	32	14	31,33	48,52	48,30,52	80,53
Density g/cm^3	5.33	2.33	5.32	6.20	5.78	6.4
Band Gap eV	0.67	1.12	1.43	1.44	1.57	2.13
Pair creation Energy eV	2.96	3.62	4.2	4.43	4.6	4.2
Resistivity $\Omega\ cm$	50	10^4	10^7	10^9	10^{10}	10^{13}
Electrons mobility cm^2/V	> 1	> 1	10^{-5}	10^{-3}	$10^{-3} - 10^{-2}$	10^{-4}
Holes mobility cm^2/V	> 1	~ 1	10^{-6}	10^{-4}	10^{-5}	10^{-5}

Table 2.1: Properties of the principal semiconductor detectors on the market [43].

an atomic electron while the scattered photon has the remaining energy. This process depends from the material atomic number as Z.
The last possible process is pair production which depends from the material atomic number with a Z^2 proportionality and is typical of high energy photons, i.e. with energy above 1.02 MeV, the threshold energy a photon needs to interact with the coulombian field to produce an electron-positron pair.
Fig.2.1 shows the linear attenuation coefficient for some semiconductor detectors compared to the values for a typical NaI scintillator detector commonly used for spectroscopic purposes.
Silicon detectors have a lower linear attenuation coefficient for all the processes. Germanium detectors have a lower coefficient for the energies where photoelectric effect is dominant while for higher energies the performances are comparable to the other detectors. For CdZnTe detectors it is possible to see that for energies lower than 200-300 keV the photoelectric effect is dominant, for energies between 200-300 keV and 1-2 MeV the dominant component is the Compton scattering and for higher energies the main process is pair production.
If we consider a CdZnTe detector 20 mm thick and we calculate the absorption efficiency (2.1) for a gamma of 500 keV, i.e. a reference energy close to the 478 keV peak of our interest, we find that the photoelectric effect has a 14.5% absorption efficiency while for the dominant Compton scattering it is 57%. At such energy we have to take into account that the sensitivity of the detector will be lower due to the value of the photoelectric absorption efficiency.

$$\epsilon_{abs} = 1 - \frac{I}{I_0} = 1 - e^{-\mu_{lin} \cdot x} \tag{2.1}$$

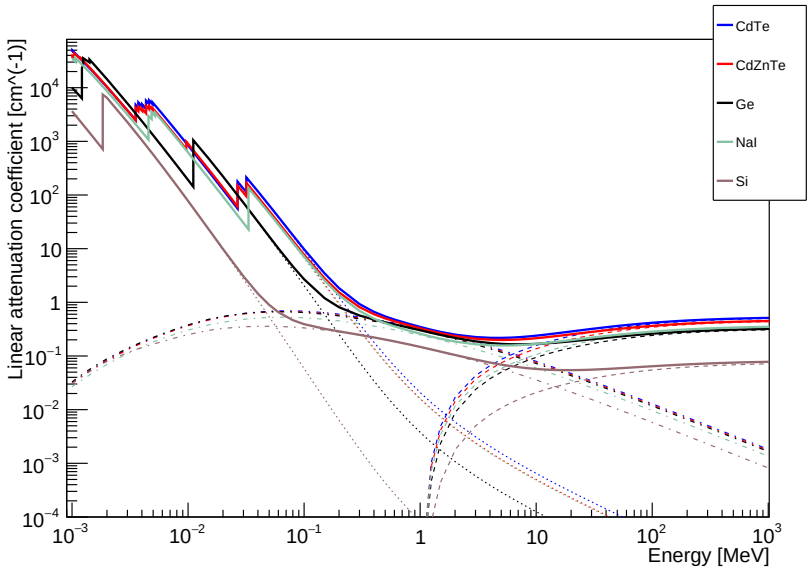

Figure 2.1: Linear attenuation coefficient for various detectors. Solid line is the total coefficient. Photoelectric effect, Compton scattering and pair production are singularly reported for each detector.

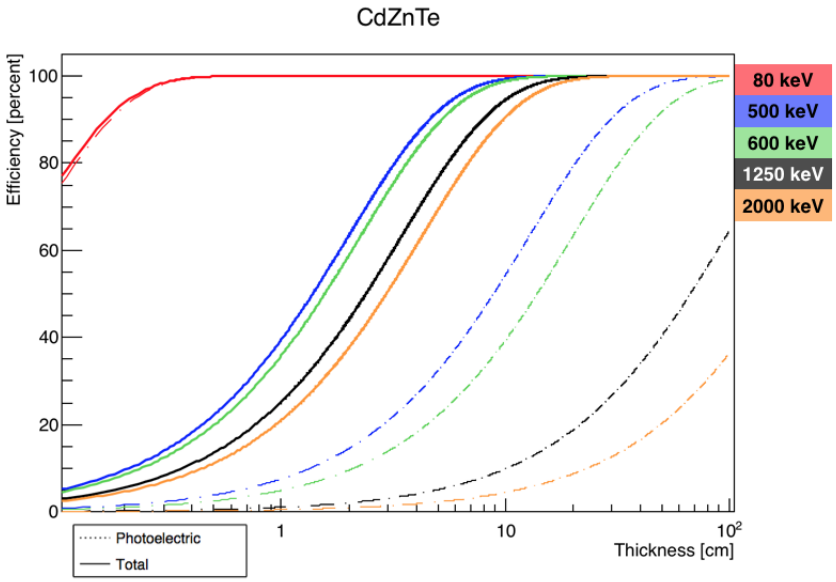

Figure 2.2: Photoelectric and total absorption efficiency as function of CdZnTe detector thickness.

2.2 Physics of the electron-hole collection

Usually in scintillator detectors the photon energy is converted in scintillation photons which in turn are turned into an electronic signal by means of a photomultiplier. Semiconductor detectors don't need the photo-multiplication step, the photon interactions in the material emit electrons which in turn create electron-hole pairs in the material. The number of pairs created is proportional to the initial photon energy and their drift towards respectively the anode and cathode, through and external electric field, induces a variation of charge ΔQ on the electrodes. ΔQ can be calculated using the Shockley-Ramo theorem described by Eq.2.2 [44, 45].

$$\Delta Q = -q[\phi(x_f) - \phi(x_i)] \tag{2.2}$$

ΔQ is the charge induced by a carrier q which moves from an initial point x_i to a final point x_f. ϕ represents the weighting potential namely the potential measurable in a detector when the anode is set at unit potential while the cathode is set at zero. In a semiconductor planar detector the weighting potential can be written as $\phi(x) = \frac{x}{L}$, with $0 \leqslant \frac{x}{L} \leqslant 1$, where L is the distance between the two electrodes and x is the distance between the cathode and the point of the electron-hole pair production.
If we consider not to be any charge loss during the carriers drift the ΔQ induced by N elctron-hole pairs can be written as:

$$\Delta Q = \Delta Q_{holes} + \Delta Q_{e^-} = -e\Big[N\frac{0-x}{L} - N\frac{L-x}{L}\Big] = N \cdot e \tag{2.3}$$

N is the number of electron-hole pairs created by the interaction and thus can be written as $N = \frac{E}{w}$, E is the incident photon energy and w is the average pair creation energy for the detector. The quantity $N \cdot e$ can also be called Q_0 or the generated charge cloud.
Nonetheless not all produced electron-hole pairs are collected due to charge trapping and recombination which are two typical effects in semiconductor detectors. To quantify the influence of these effects the charge collection efficiency (CCE) is introduced. CCE is given by Hecht equation 2.4 where $\lambda_h = \mu_h \tau_h E$ and similarly λ_e are the mean drift lenghts of holes and electrones respectively [46].

$$CCE = \frac{Q}{Q_0} = \frac{1}{L}\Big[\lambda_h\Big(1 - e^{-\frac{x}{\lambda_h}}\Big) + \lambda_e\Big(1 - e^{-\frac{L-x}{\lambda_e}}\Big)\Big] \tag{2.4}$$

It is clear that the position of interaction influences the collection efficiency thus producing a peak broadening in the spectrum. Moreover the mobility of electrons and holes plays a crucial role in choosing the detector thickness and energy range. Compound semiconductors are characterized by low mobilities thus limiting the mean drift ranges of electrons and holes, moreover the trapping is crucial in limiting the transport and it is due for example to impurities in the material, crystal defects or dislocations. Both factors are taken into

account in the charge collection efficiency.
One parameter to study the detector performances is the energy resolution which is also dependent from the CCE via equation 2.5.

$$\Delta E = \sqrt{2.355^2 \cdot F \cdot E \cdot w + \Delta E_{el}^2 + \Delta E_{coll}^2} \tag{2.5}$$

F is the Fano factor which represents the noise due to statistical fluctuations of the electric charge production process in a detector. In a CZT detector the Fano factor is $F = 0.089 \pm 0.005$ as reported by Redus et al.[47].
ΔE_{el} represents the electric noise while ΔE_{coll} is the contribution due to the charge collection process. The first can be measured using a precision pulser while the second can be calculated using some semi-empirical models [48].

2.3 Properties of a CdZnTe detector

This thesis focused on CdZnTe detectors for a BNCT-SPECT system exploiting the crystal characteristics.
The 1.57 eV bandgap of this solid state detector not only ensures it to work at room temperature but also lowers the leakage currents and increases its resistivity. The leakage currents are less than 10 nA at room temperature while its resistivity is of the order of 10^{10} Ωcm [49]. Another important advantage of CZT detectors is that they do not suffer from any polarization effect which in turn is a drawback from CdTe detectors [50, 51].
Main disadvantage of CZT detectors is the very low value of carriers mobility, in particular the difference between holes and electrons mobility leads to long tails in the measured spectra. Fig.2.3 shows the difference between a NaI(Tl) and a CZT acquired spectra of ^{99}Tc non-collimated source.
Various methods have been studied to reduce the low energy tail and thus to increase the charge collection efficiency.
Usually a planar CZT detector is used in planar parallel field (PPF), i.e. the detector is irradiated through the cathode. The mean free path of a photon is proportional to its energy, therefore a low energy photon, such as those used in conventional SPECT, would have a low penetration in the detector volume, the electron-hole production would take place close to the cathode thus favouring the hole collection and lowering the loss of information that gives way to the low energy tail in the spectra. However the PPF irradiation is not as good performing for high energy photons that need thicker detectors and have an increased depth of interaction thus producing an electron-hole pair closer to the anode [53].
To improve the detection for high energy photons a planar CZT detector can be used in planar transverse field (PTF) which means that the irradiation takes place orthogonally to the electric field. Fig.2.4 shows the difference between the two irradiation setups.

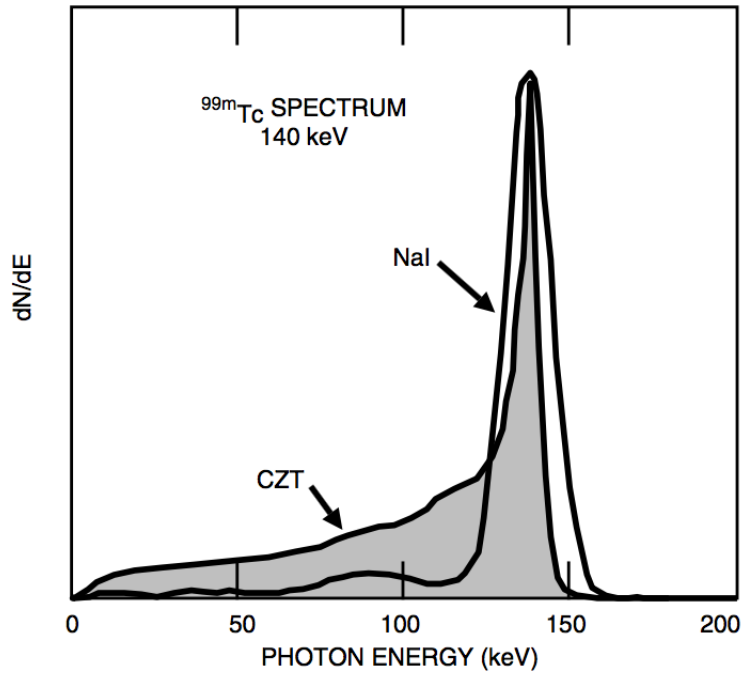

Figure 2.3: Comparison between a NaI(Tl) and a CZT spectra obtained with a ^{99}Tc source [52].

PTF is versatile for high energy photons because the thickness of the detector can be chosen accordingly while keeping the distance between the electrodes fixed as the charge collection properties of the detector.

PPF and PTF are methods based on modifying the irradiation geometry, other commonly employed methods are based on the analysis of the preamplified signal such as risetime discrimination (RTD) methods.

RTD consists in selecting only the signal due to electrons by discriminating the preamplifier pulses with short rise time thus leading to a better energy resolution even though it reduces the sensitivity of the detector.

RTD is not the only electronic method that can be used, bi-parametric analysis (BP) exploits both the rise time of the signals and the amplitude. It has been proved that there is a correlation between these two parameters and an incomplete charge collection. Thus by recognizing the partial signals it is possible to reject them and improve the CZT detector performances [55].

Single charge collection detectors are an additional solution to the low hole mobility. If the electrodes are designed correctly the signal can be obtained by taking into account only the electron drift, thus making the signal unaffected by holes trapping.

To such purpose the small pixel effect is exploited, the anodes are to be made as small as possible this way it is possible to avoid the possible contribution of hole on the anode and obtain a signal due only to the electrons [56]. Moreover to enhance this effect conductor surfaces can be added in the detector design,

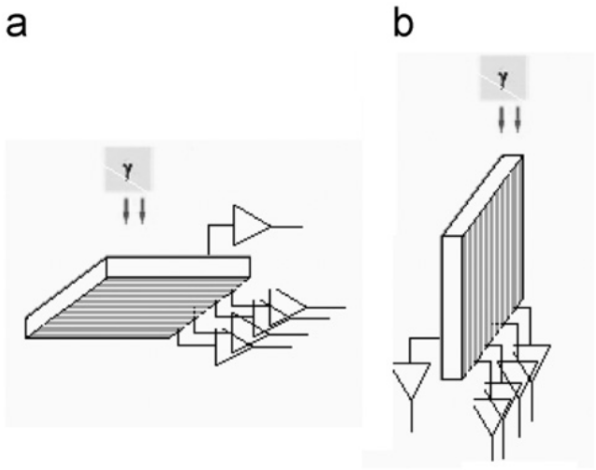

Figure 2.4: CZT detector irradiated in a) PPF mode b) PTF mode [54].

a voltage is applied to the conductors to drive the electrons to the anodes; this approach is called Frisch grid approach [57].
To manage a pixelated detector and to remove the low-frequency background due to leakage currents a dedicated and advanced electronic is necessary, usually ASIC boards are used. Even though the detector itself doesn't need cooling, the electronic system needs to be cooled, mostly to keep the heat from the detector.

2.4 Energy, timing and spatial resolution

Many studies have been conducted with the aim of exploiting CdTe and CdZnTe detectors for medical applications. One of the main fields is PET imaging, to such purpose the time resolution of the detector must be high to be able to acquire two signals in coincidence, therefore some groups focused on studying the timing resolution of CZT detectors. Table 2.2 shows some of the results for different detector sizes.

The results show some differences between detectors due to their thickness

Group	CZT Dimensions (mm^3)	Timing resolution (ns)
Okada et al. [58]	4x4x2	8.5
Amrami et al.[59]	2x2x4	5
Drezet et al.[60]	16x20x0.9	2.6
Bertolucci et al. [61]	2x10x10	20
Vaska et al. [62]	16x5x10	10

Table 2.2: Timing resolution results from various CZT detector studies

and other studies show the possible timing resolution improvements that can be achieved by using dedicated electronic readouts, therefore CZT detectors could be used for PET coincidence measurements. For SPECT imaging the timing resolution is not fundamental but the spatial and energy resolution have an important role.
Currently, in SPECT, the main detectors employed are gamma cameras with a spatial resolution around 3 or 4 mm and an energy resolution of 11% at 140 keV [63]. CdTe and CdZnTe detectors show better performances in both cases. Pixellated CZT detectors showed an energy resolution of 3% at 140 keV and an intrinsic spatial resolution smaller than 2.5 mm [64].
Table 2.3 shows a comparison of the properties of different detectors employed for nuclear medicine applications.
The energy resolution of these CdZnTe detectors is better than that of a NaI

Experiment	Detector	Energy resolution (%) at 140 keV	Spatial resolution (mm)
Anger camera [64]	NaI(Tl) 9.5 mm thick	11	3.5
Digirad 2020tc Imager^{TM} [65]	64 CZT modules (25x25x5 mm^3)	4	not reported
NUCAM3 [66]	528 CZT pixel detectors (8.5x8.5x5 mm^3)	4.5	2.1
PEGASE [67]	groups of 16 single CZT detectors (4x4x6 mm^3)	4.7	not reported

Table 2.3: Energy and spatial resolution of some detectors used in nuclear medicine [43].

detector for a source of 140 keV and the spatial resolution is similar for the two types of detectors. For a BNCT-SPECT system the source has a higher energy thus requiring thicker detectors. To have an estimation of the performances of a CZT detector suitable for BNCT-SPECT we can consider a source of 511 keV. Vaska et al. [62] reported for such source an energy resolution of 2%, which is an improvement with respect to the lower energy performances.
In regard to the spatial performances of a CZT detector Wagenaar et al. [68] compared an NaI detector and a CZT detector with a 12 x 20 cm^2 Field of View. They reconstructed the image of a Hoffman brain phantom filled with 110 MBq of ^{99m}Tc pertechnetate for both detectors as shown in Fig.2.5. It is possible to see that the CZT detector has a smaller field of view thus the image is cut on the edges, but the image resolution is higher.

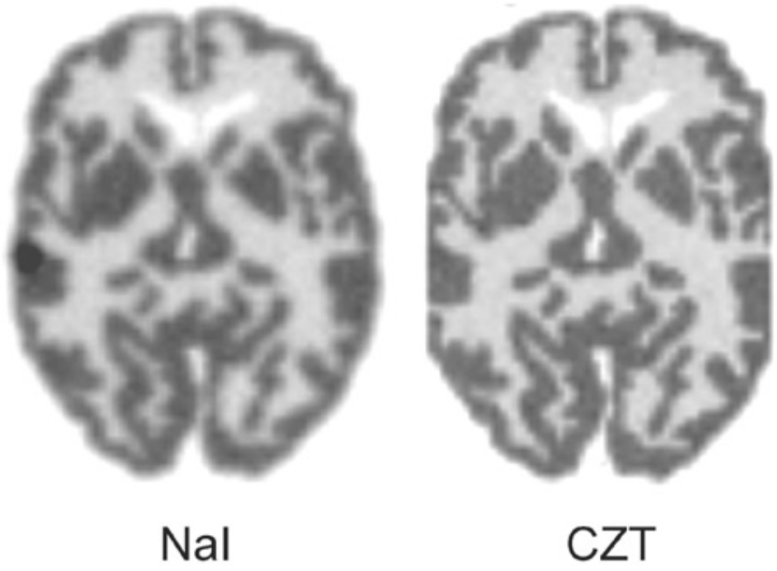

Figure 2.5: Hoffman brain phantom comparison between an NaI and CZT detectors, the hot spot on the far left in the NaI image is from activity spilled on the fill hole [68].

Chapter 3

Simulation study of a 20x20x20 mm^3 CZT detector

This Chapter focuses on the computational study of a 20x20x20 mm^3 CZT detector to be employed as a base element for a BNCT-SPECT imaging system. Currently the 3CATS project (3D Cadmium Zinc Telluride Spectro Imager for X and gamma-ray applications) funded by the Fifth National Scientific Committee (CSNV) of the Italian National Institute of Nuclear Physics (INFN) is underway and aims to build and study two 5x20x20 mm^3 CZT detectors representing half of the detector considered in this Chapter.
The simulated CZT detector is composed of four layers, each layer is a single crystal detector of 5x20x20 mm^3, the dimension of each layer is fixed due to the constraints of growing a single crystal.
Fig. 3.1 shows the single detector layer and the stacked 20x20x20 mm^3 prototype. Each layer would have 20 anodic strips and 10 cathodic strips perpendicular to the anodic ones, thus each pixel has dimensions 1x5x2 mm^3.

Each detector layer is employed in Planar Transversal Field, which means that the photons enter the crystal perpendicularly to the electric field; in our case this means that each layer is irradiated on a 5x20 mm^2 surface and has a 20 mm thickness thus we expect a good detection efficiency around 500 keV (the mean free path in CZT material is $\sim$ 17 mm).
The choice of using 4 layers gives a total irradiated surface of 20x20 mm^2 covering a limited FOV. To be able to build a BNCT-SPECT imaging device it will be necessary to use bigger detector arrays composed of this 20x20x20 mm^3 base element. Therefore the study of such detector gives us some preliminary information about the detector efficiency and image reconstruction capabilities.

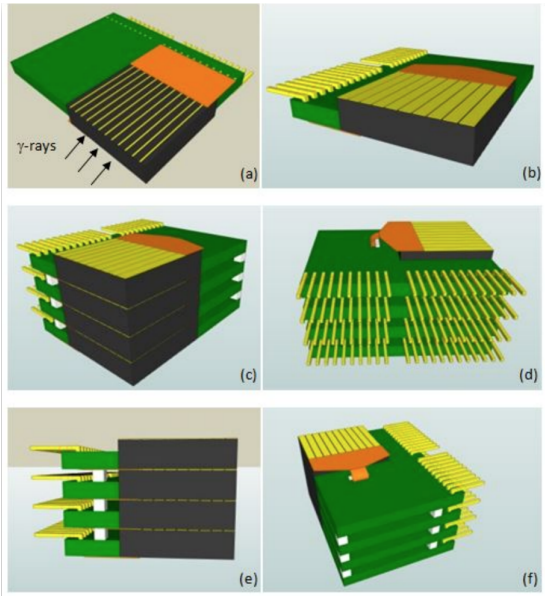

Figure 3.1: Schematic representation of the array of four 5x20x20 mm^3 CZT detectors (a) and (b) show a 5x20x20 mm^3 single crystal layer and figures (c) to (f) show the complete prototype made of 4 layers, on behalf of 3CATS experiment.

3.1 Energy Resolution and Efficiency

The 20x20x20 mm^3 CZT detector was first simulated using MCNP6 Monte Carlo code to study its response to standard gamma calibration sources such as ^{133}Ba, ^{137}Cs, ^{22}Na and ^{60}Co. The point sources were positioned at 21 cm distance from the detector face and their emission was isotropic. The ^{137}Cs, ^{22}Na sources were chosen because the photopeak and the annihilation peak respectively are in the energy range of interest for BNCT-SPECT thus giving a good idea of the detector performances in recording the 478 keV photon emitted during BNCT treatment. ^{133}Ba and ^{60}Co were instead chosen to probe the detector performances at energy ranges lower and higher respectively to the range of BNCT-SPECT interest.
The Monte Carlo simulation results were deemed acceptable if the error was below 10%. Fig. 3.2, Fig. 3.3, Fig. 3.4 and Fig. 3.5 show the spectra obtained from the simulation.
The width of the energy bin of the simulation was chosen coherently to the FWHM measured for each source in the experiment described in Chapter 4.
The simulations have then been used to calculated the detector efficiency. The intrinsic efficiency ϵ_i of a detector is defined as the number of detected photons under the photopeak over the number of gammas incident on the detector 20x20 mm^2 surface, i.e. the number of photons emitted by the source multiplied by the geometrical efficiency ϵ_g as in equation 3.1.
Therefore an high quality detector must maximise the number of detected

photons. CZT detector has high Z materials thus being able to absorb a high number of gamma rays, even with modest thicknesses when compared to scintillators, to improve the detection efficiency.

$$\epsilon_i(E) = \frac{detected\ \ photons}{emitted\ \ photons \cdot \epsilon_g} \tag{3.1}$$

To calculate the simulated efficiency of the detector Eq.3.2 is used, where B.R. is the branching ratio of the source gamma emission.

$$\epsilon_i(E) = \frac{R(E)}{B.R. \cdot \epsilon_g} \tag{3.2}$$

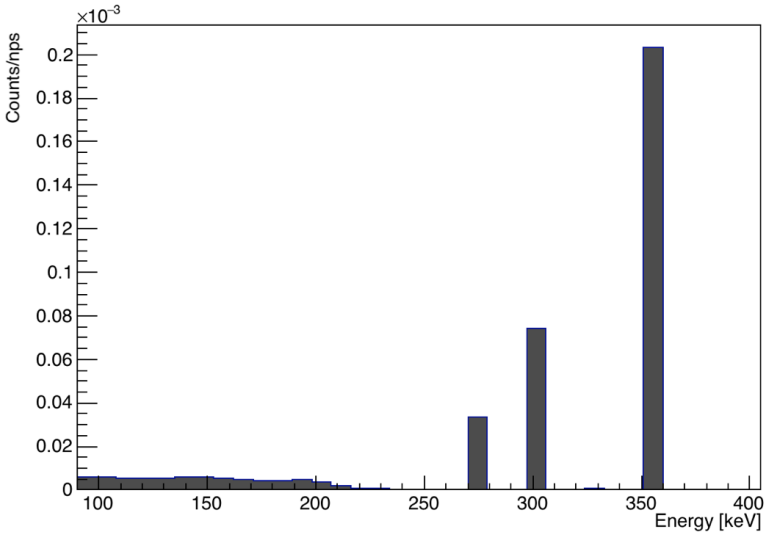

Figure 3.2: Simulation of the 20x20x20 mm^3 CZT detector response to a ^{133}Ba point-like source, the detected energies are 276 keV, 302.8 keV and 356 keV.

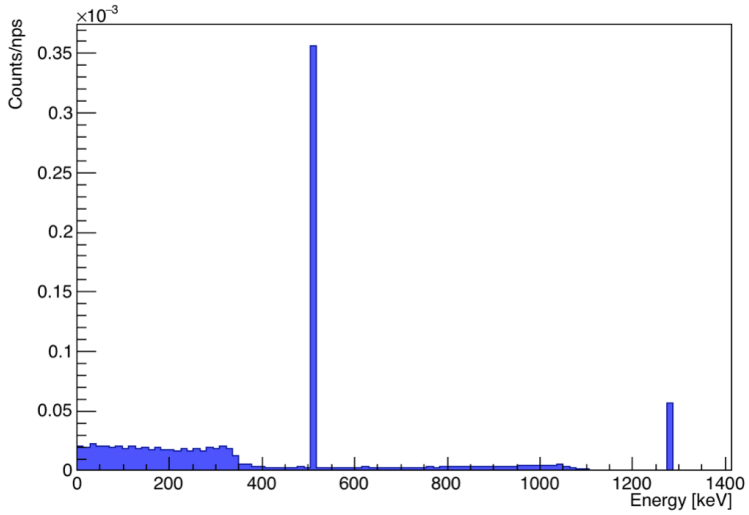

Figure 3.3: Simulation of the 20x20x20 mm^3 CZT detector response to a ^{22}Na point-like source, the detected energies are 511 keV and 1274.5 keV.

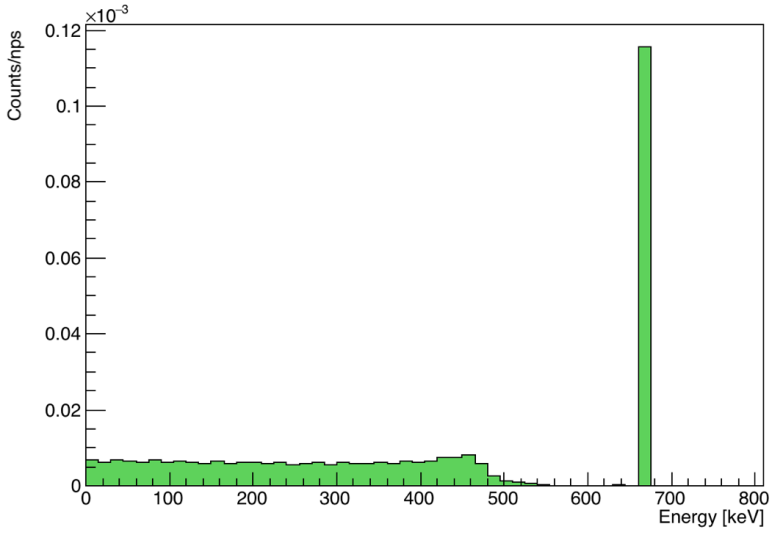

Figure 3.4: Simulation of the 20x20x20 mm^3 CZT detector response to a ^{137}Cs point-like source with emission energy of 661.6 keV.

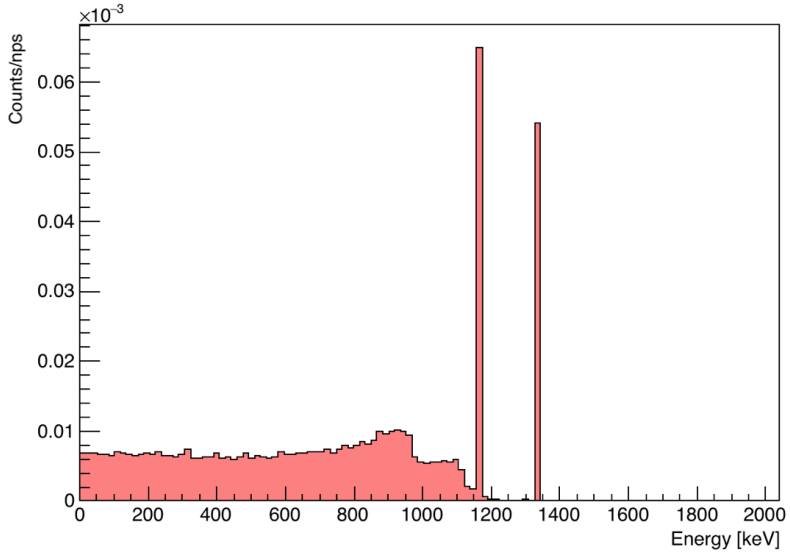

Figure 3.5: Simulation of the 20x20x20 mm^3 CZT detector response to a ^{60}Co point-like source, the detected energies are 1173 keV and 1332.5 keV.

R(E) is the result given by the computation performed with MCNP code which counts the particles detected under the photopeak by the simulated CZT volume and normailizes the result to source particle.
The geometric efficiency of the detector can be expressed as the solid angle subtended by the source and the detector surface Ω over 4π. To calculate the detector geometrical efficiency when the source is 21 cm away a simulation was performed. The detector volume was filled with air and an F1 current tally was used to calculate the fraction of photons passing through the detector 20x20 mm^2 surface. The computed geometric efficiency of the 20x20x20 mm^3 detector was found to be $\epsilon_g = 7 \cdot 10^{-4}$. The results are shown in Tab. 3.1.

Source	Energy [keV]	ϵ_i [%]
^{133}Ba	276	67.13
^{133}Ba	302.8	57.98
^{133}Ba	356	47.08
^{22}Na	511	29.49
^{137}Cs	661.6	19.53
^{60}Co	1173	10.75
^{22}Na	1274.5	8.32
^{60}Co	1332.5	7.83

Table 3.1: Simulated intrinsic detection efficiency of a 20x20x20 mm^3 CZT detector.

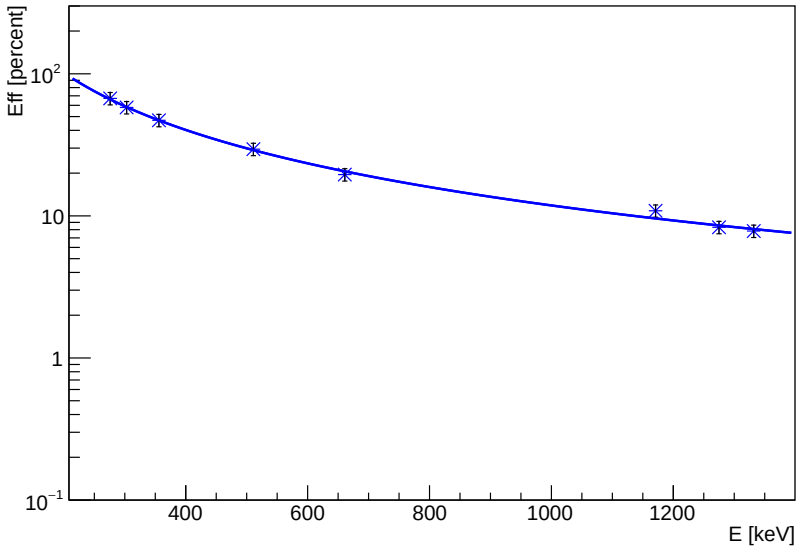

Figure 3.6: Simulated intrinsic efficiency for a 20x20x20 mm^3 CZT detector as function of the energy between 276 keV and 1333 keV.

Fig. 3.6 shows the 20x20x20 mm^3 detector efficiency when fitted with a function of type $\epsilon_i = a \cdot E^b$ where $a = (1.2 \pm 0.5) \cdot 10^5$, $b = (-1.34 \pm 0.06)$ and $\chi^2 = 1.73$
The efficiency for a 478 keV source located at 21 cm from the detector surface is 30.8 % when calculated using the previously found function.

3.2 Image reconstruction and Spatial Resolution

We aim to use the 20x20x20 mm^3 CZT detector as the base element for a BNCT-SPECT system dedicated for small animals such as mice and rats.
To understand the imaging capabilities of the 20x20x20 mm^3 CZT detector a simulation campaign was taken up using Geant4 Monte Carlo code [69, 70].
The simulation campaign began as a collaboration with Ph.D. student Chunhui Gong and Nanjing University of Aeronautics and Astronautics (NUAA) while the author spent 3 months as an exchange PhD student at NUAA.
The purpose of these simulations was to acquire enough data to be able to reconstruct an image of the computed object. The geometry of the simulation is shown in Fig.3.7.

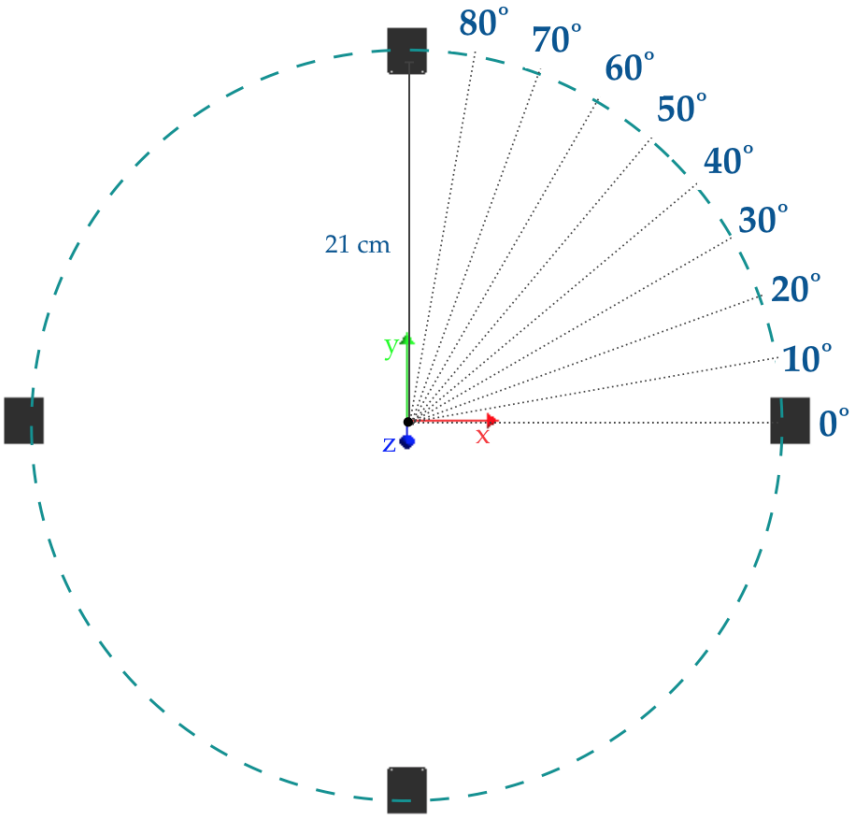

Figure 3.7: Schematic representation of Geant4 simulation geometry of the 20x20x20 mm^3 CZT detector used to reconstruct an image.

Four 20x20x20 mm^3 detectors are positioned around the origin at 0°, 90°, 180° and 270°, the distance between the detectors and the origin is 21 cm to take into account the distance that should be left between the rat phantom and the detectors. The detectors are then rotated around the z axes with 10° steps, spectra are acquired from each detector at each angular step.
Each detector is composed of 20 mm thick and 1x5 mm^2 pixels as can be seen in Fig.3.8, the total number of pixels is 80, 20 for each 20x5x20 mm^3 detector layer, corresponding to the segmentation due to the 20 anodic strips. The simulation allows us to read each pixel singularly to understand the position of the photoelectric interaction inside the detector.
In this simulation no collimation system was implemented in the geometry, instead a virtual collimator with a 1 degree acceptance angle was used.
The pixels data are separately stored for each 20x20x20 mm^3 detector and are saved in a CERN ROOT NTuple. The data is then analysed using ROOT5 [71] and the images are reconstructed with a Filtered Back Projection using Python2.7 and its packages NumPy [72] and scikit-image [73].
As described in Chapter 1 to calculate the spatial resolution of the reconstructed image the PSF function must be used, therefore a point-like, isotropic source of 478 keV gamma rays was positioned on the coordinates (-0.6, 0, 0)

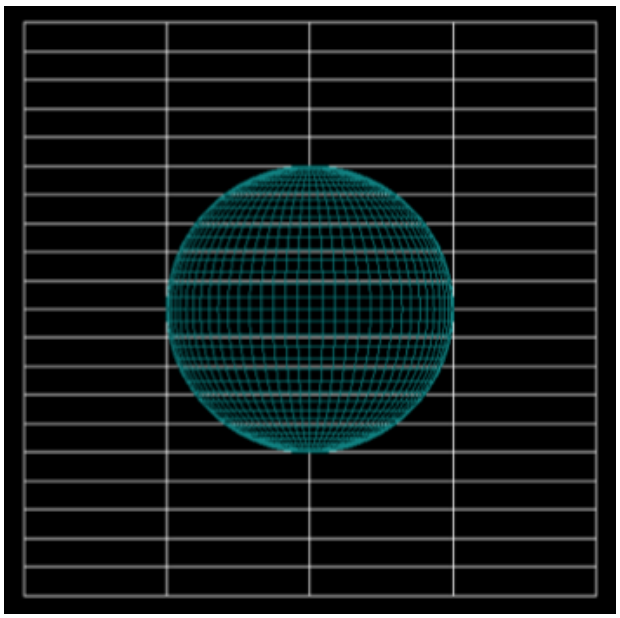

Figure 3.8: Geant4 geometry of the 20x20x20 mm^3 CZT detector, detail of the detector's pixels (in white lines) and a spherical source in the origin (in blue).

cm of the simulated reference system. The data was deemed acceptable if the error on the most populated bins was <7%.
The reconstructed image is shown in Fig.3.9. Since the detector is composed of four layers of dimension 20x5x20 mm^3 the image is reconstructed for each layer. The two central layers are shown for reference, the layers collect 478 keV photons and the source is reconstructed as a circular bright point.
To calculate the spatial resolution of the image each layers data was projected on a 2D scatter plot and fitted with a Gaussian function.
Fig. 3.10 and Fig. 3.11 show respectively the gaussian fitted data for Layer 2 and Layer 3. In Layer 2 the mean value is $\mu = 13.8 \pm 0.02$ pixels and the standard deviation is $\sigma = 2.38 \pm 0.01$ pixels. Layer 3 has a mean value identical to the previous one $\mu = 13.8 \pm 0.02$ pixels and a standard deviation of $\sigma = 2.36 \pm 0.01$ pixels. In both cases we can find the FWHM using equation 3.3.

$$FWHM = \sigma\sqrt{8ln2} \tag{3.3}$$

Layer 2 and Layer 3 have respectively a full width half maximum of $FWHM = 5.61 \pm 0.02$ pixels and $FWHM = 5.56 \pm 0.02$ pixels. If we approximate to an integer value we can say that the FWHM is found to be 6 pixels and thus this is the spatial resolution of our 20x20x20 mm^3 CZT detector.

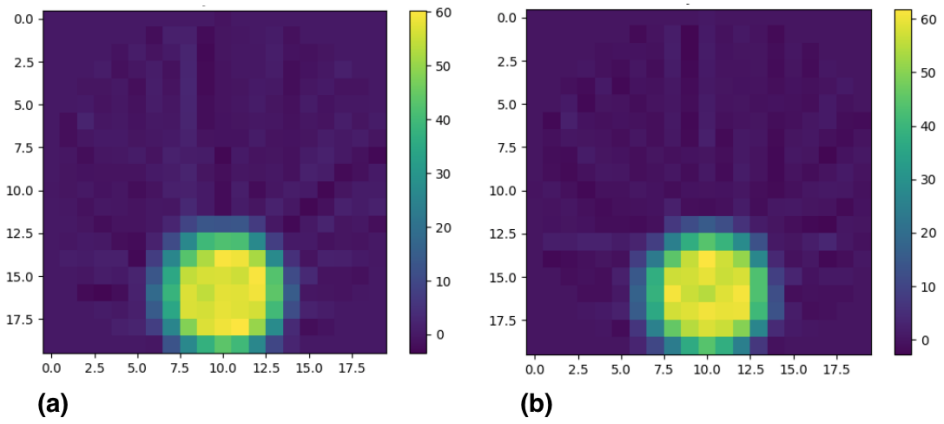

Figure 3.9: FBP image reconstruction of a point-like, isotropic source: (a), (b) are the reconstructions for the two central layers of the 20x5x20 mm^3 CZT detector.

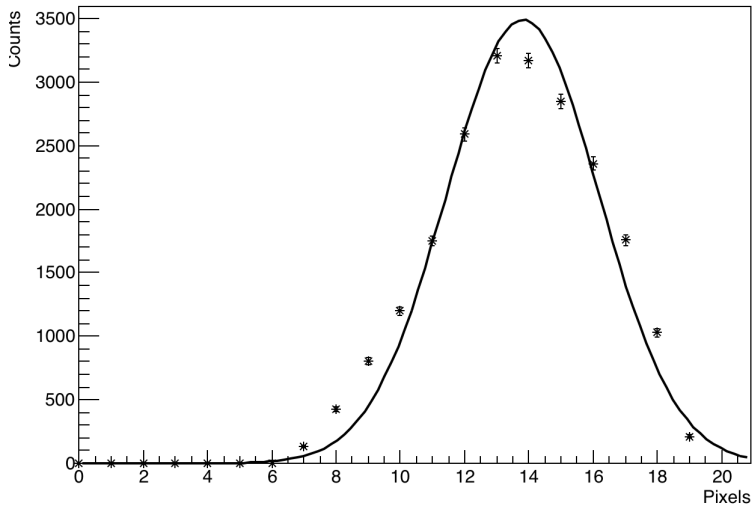

Figure 3.10: Layer 2 counts vs. pixel number fitted with a Gaussian function.

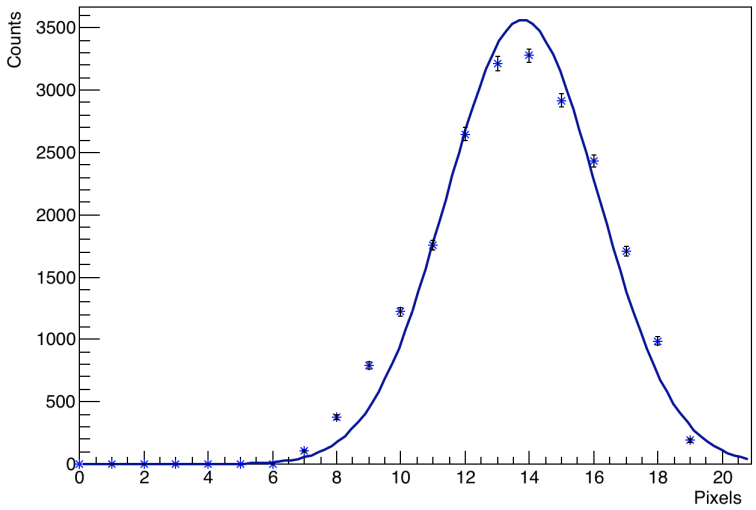

Figure 3.11: Layer 3 counts vs. pixel number fitted with a Gaussian function.

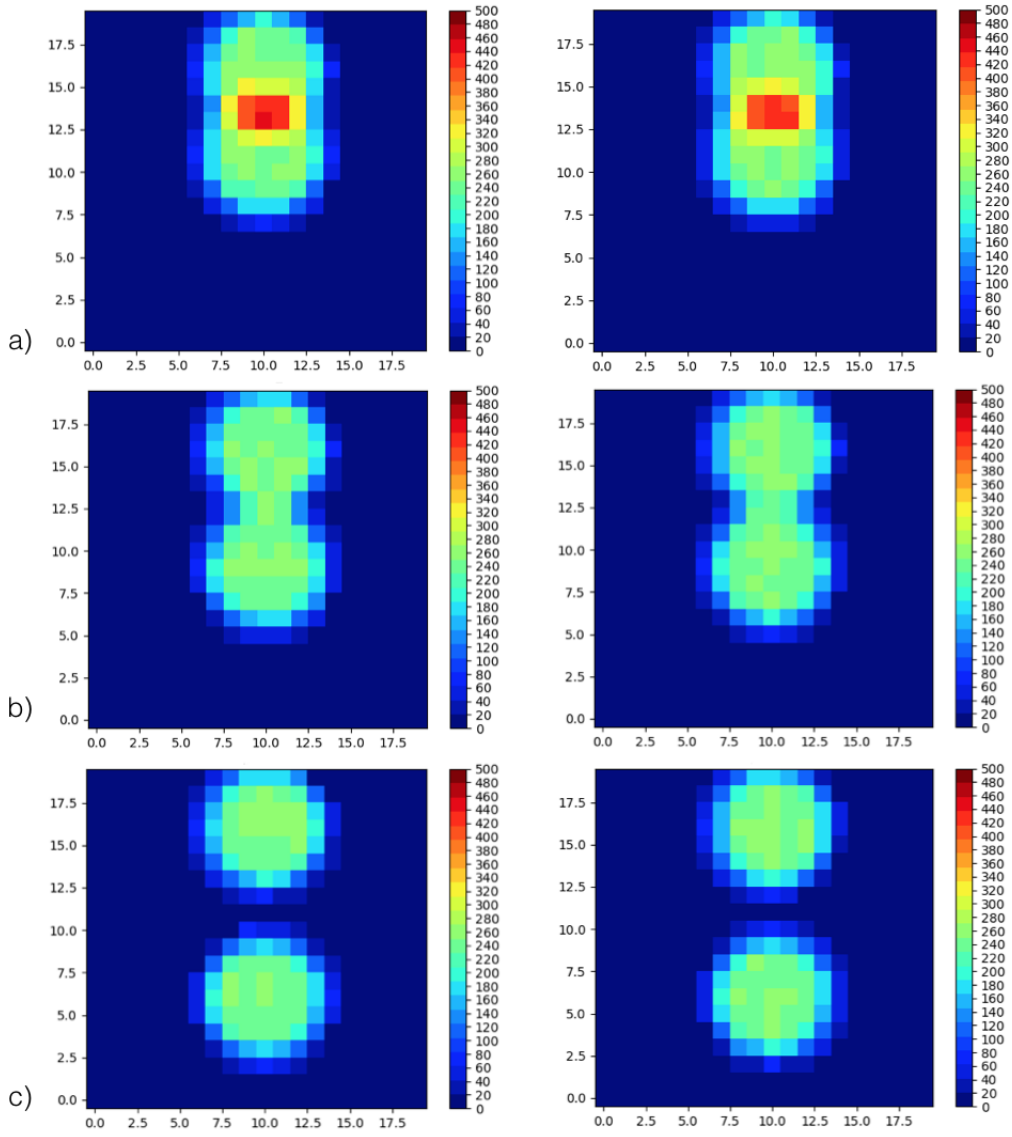

Figure 3.12: Image reconstruction of two point sources at distances: a) 5 mm, b) 7 mm and c) 10 mm, the figure shows Layer 2 and 3 as examples of the result.

To test the ability of the detector to distinguish between two point sources positioned in the field of view we simulated three diffent setups where the distance between the two sources was respectively 5, 7 and 10 mm. For each case Layer 2 and 3 are shown. Fig.3.12 shows the comparison of the three cases. It is possible to see that when the two source are at 5 mm distance are not correctly distinguishable and are partially superimposed. When the distance increases we can see that at 7 mm the two sources are almost separated and at 10 mm they are correctly distinguishable.

3.3 Rat phantom

The previous simulations aimed to study the spatial resolution of the detector and its imaging capabilities in an ideal situation. To make the simulations more realistic a first step is to introduce a PMMA rat phantom. One of the research subjects that the Pavia BNCT group focuses on is the pre-clinical studies of the safety and feasibility of BNCT treatment on tumours induced on small animals. Therefore, a more realistic simulation that in the future could be compared to a measurement in our facility, consists in using a rat phantom. The phantom is a cylinder of 8 cm diameter and 20 cm length representing a rat.
Moreover the source has been changed to a finite sphere of diameter 1 mm.
The simulation was once again performed with a reciprocal distance source-detector of 21 cm.
Fig.3.13 shows the comparison between the simulation with and without phantom for a single source of 1 mm diameter.
The rat phantom does not emit any background gamma, it is just used to understand which is the photon attenuation due to the phantom. We calculated that 4 cm of PMMA phantom should attenuate the 478 keV photons by 35%. When the phantom is added to the simulation the detected 478 keV counts are lower than the case without phantom. This attenuation can be explained considering that the phantom acts as a scatterer thus changing the directions of some photons. From the reconstructed image we can see that the photon contribution with the phantom is 33% lower than the case without the phantom close to result we expected.

3.4 478 keV background

Another step to consider to make the simulations closer to reality is to add the background contribution. A possible problem for correct image reconstruction in a BNCT-SPECT system is connected to the presence of low quantities of boron also in the healthy tissues, the amount is usually 3 to 6 times lower

than the one in the tumour, nonetheless when irradiated it emits the 478 keV gamma.
In the simulations the setup considered an emitting rat phantom and a d=1 mm source located inside the phantom at 21 cm distance from the detectors. Since in reality not the whole phantom is irradiated only the 3 cm long section of the phantom that includes the source was set as the 478 keV background emitter. The emission intensities were set to 1:3 for the background in respect to the source.

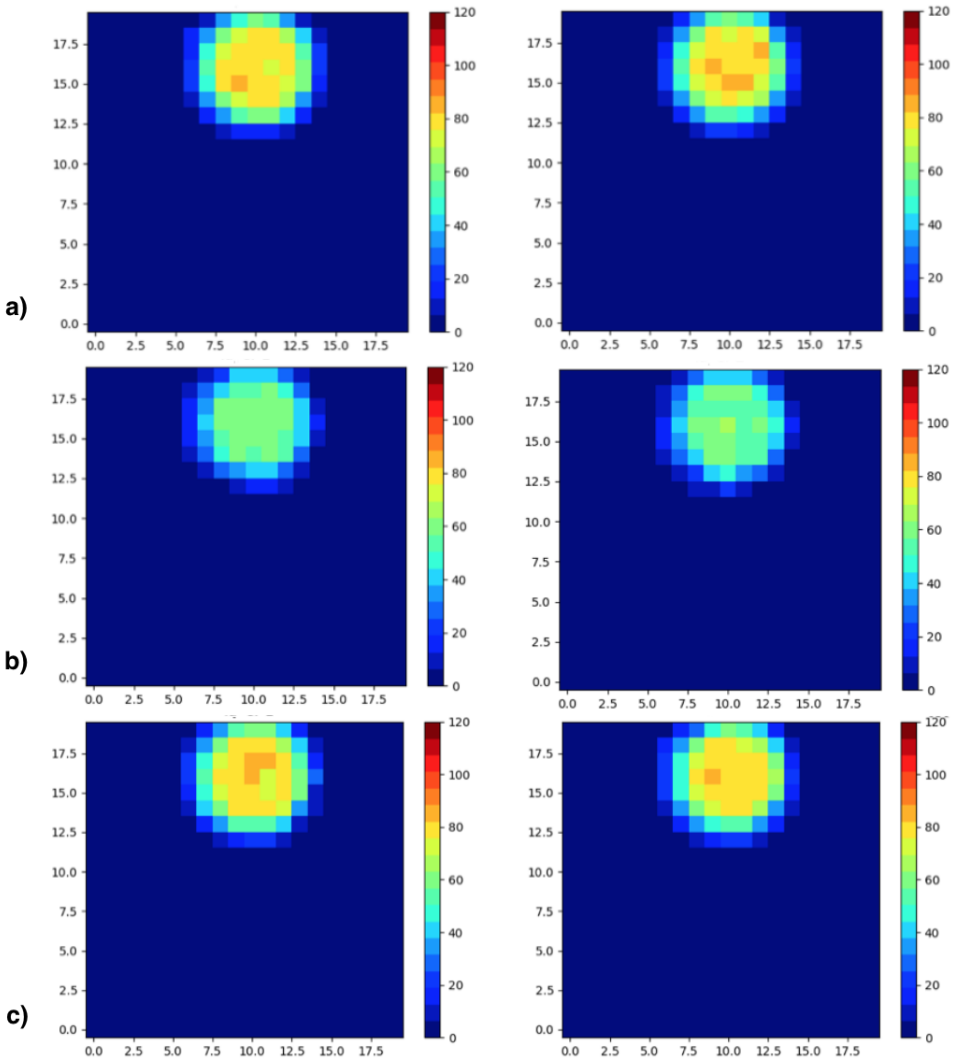

Figure 3.13: Comparison between Layer 2 an 3 FBP reconstructions of a 1 mm source without phantom (a), with phantom (b) and with emitting phantom at 478 keV (c).

Fig.3.13 b) and c) show the image reconstructed without and with gamma background emitted by the phantom. The comparison shows that the 478 keV

gamma signal is higher in case c), this might be due to the fact that even though the phantom attenuates the source contribution it also emits at the same energy.
The results also show that even though there is a 478 keV gamma background the spatial resolution of the reconstructed image is still 6 mm.

3.5 Performances with NEMA phantom

Another step to consider to study the reconstruction abilities of the detector consists in reconstructing the image of a three source simulation. Usually to asses the imaging capabilities of a SPECT system a NEMA phantom is employed [37]. The NEMA phantom is a plastic cylinder of 22 cm diameter filled with water. Fig.3.14 shows the NEMA cylindrical phantom in which 3 rods of ^{57}Co are inserted as source emitting at 122 keV.

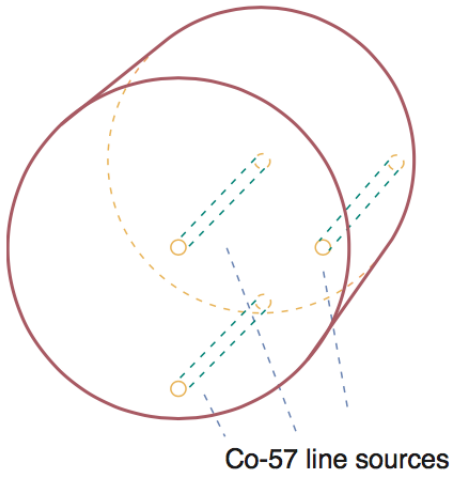

Figure 3.14: NEMA phantom for evaluating the spatial resolution of a SPECT camera [37]. The phantom is a 22 cm diameter plastic cylinder filled with water.

3.6 Four detector array

To have a larger field of view and a simulation closer to a possible small animal BNCT-SPECT imaging system we coupled together four 20x20x20 mm^3 detectors, thus we obtained a 40x40x20 mm^3 array with a 4 cm FOV and 8

layers each composed of 40 pixels.
Once again we used as a source three rods of diameter 1mm and length 3 cm but in this simulation the relative distances of the rods employed were higher than the previous case, and thus we were able to better distinguish them.
Fig. 3.16 shows the 4 layers of image reconstruction for the simulation. In the reconstructed image of the layers we are able to distinguish the three sources. In this reconstruction it is possible to see that the artefacts are much more visible than in the previous cases, this is due to the higher number of pixels that are more than the projection angles. To reduce the artefacts we should increase the angular projection. To improve the reconstruction a filter could be employed or a different kind of reconstruction algorithm could be studied. Nonetheless the simulations and the image reconstructions show that the 20x20x20 mm^3 CZT detector had a good spatial resolution and imaging capabilities and if employed as part of an array it could be successfully employed for a BNCT-SPECT imaging system for small animals.

3.7 Application to clinical BNCT

The aim of this study was to test the feasibility of the 20x20x20 mm^3 CZT detector as a base element of a BNCT-SPECT system to be employed for the imaging of small animals during BNCT treatment.
The results show a good image resolution that has room for improvement. To obtain these results the simulation was performed using four detectors collecting data at the same time and with 9 angular position, each simulation was performed with a 478 keV source emitting 10^9 particles, and thus the total number of gamma emitted to have these results was $9 \cdot 10^9$.
We have now to understand if in clinical conditions this number of emitted 478 keV photons is realistic.
To understand how many 478 keV photons are emitted in a standard clinical protocol irradiation we can use Eq.3.4.

$$R.R. = n \cdot \sigma \cdot \phi \cdot V \tag{3.4}$$

A standard clinical flux ϕ for a tumour irradiation is approximately 10^9 n cm^{-2} s^{-1}. Moreover the tumour usually absorbs ~ 50 ppm of ^{10}B which corresponds to $n = 3 \cdot 10^{18}$ ^{10}B atoms per cm^3. We know that the ^{10}B capture reaction cross section for thermal neutrons is $\sigma = 3840$ barns, and if we consider a 1 mm^3 we have all the parameters needed to find the reaction rates (R.R.) of thermal neutrons on 50 ppm of ^{10}B and thus the number of emitted 478 keV photons per second.
Using Eq.3.4 we found $R.R. = 1.15 \cdot 10^4$ reactions per second.
If we consider that the 478 keV photons are emitted in the 94% of the cases by the ^{10}B thermal neutron capture (as shown in Eq. 1.1), we can find the number of photons emitted per second which is $1.08 \cdot 10^4$ photons per second. Moreover

if we consider that a standard BNCT clinical irradiation lasts at least 30 min the total number of 478 keV photons emitted during a therapy is $1.9 \cdot 10^7$. The total number of 478 keV photons emitted during a standard BNCT clinical therapy is almost two order of magnitude lower than the total emission we used in our simulations and as such shows us that to successfully perform the imaging of a small animal during BNCT treatment using the 20x20x20 mm^3 CZT detector we need to consider a smaller distance between the detector and the small animal and to use a thicker angular step.

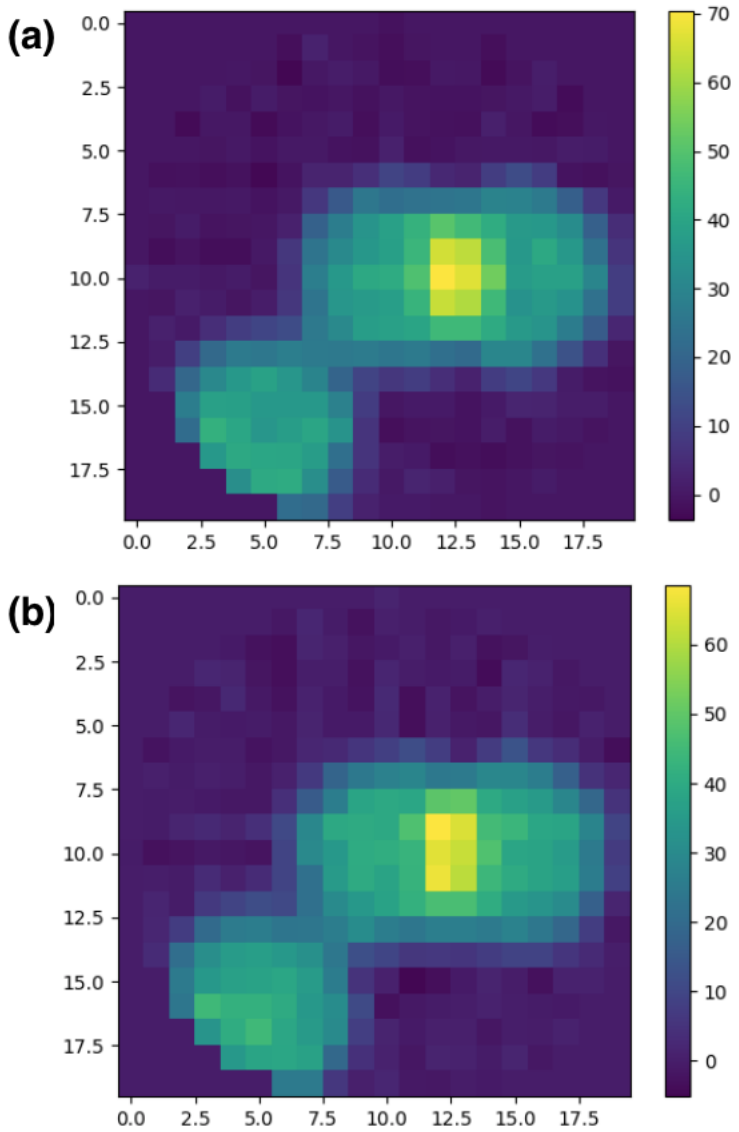

Figure 3.15: Image reconstruction of three emitting rods inside a 8 cm diameter phantom: (a), (b) are the reconstructions for the two central layers of the for a 20x20x20 mm^3 CZT detector.

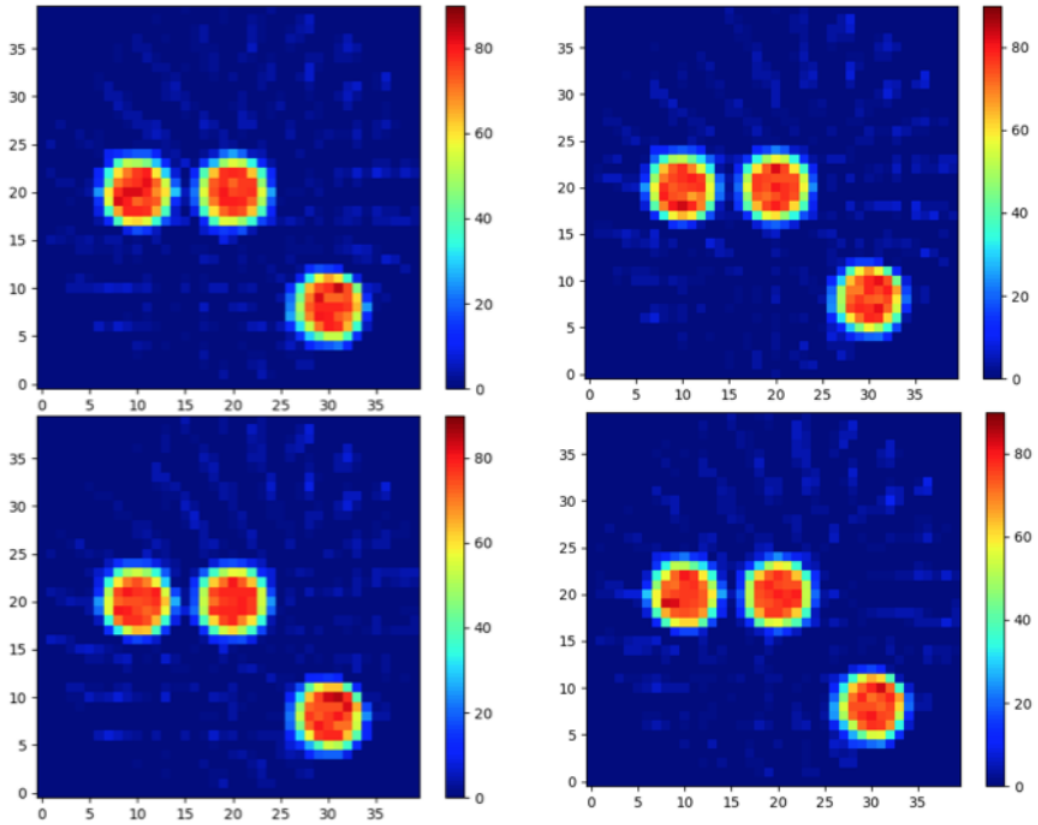

Figure 3.16: Image reconstruction of three emitting rods inside a 8 cm diameter phantom for a 40x40x20 mm^3 array of four CZT detectors, four layers are reported as an example.

Chapter 4

Experimental characterization of a 5x5x20 mm^3 CZT detector

This chapter focuses on the experimental characterization of a 5x5x20 mm^3 CZT detector developed by due2lab s.r.l. as a prototype for the sensor stage of a BNCT-SPECT system. The crystal dimensions are smaller than those chosen for a base element of a BNCT-SPECT system, as discussed in chapter 3, but the thickness is optimized for the detection of 478 keV gammas in PTF configuration. The prototype can be exploited to understand the crystal behaviour when irradiated with standard calibration sources of various energies and moreover it is useful to study the CZT crystal performances when working in a neutron and photons mixed irradiation field typical of a BNCT treatment room.
The CZT detector readout electronics is not state of the art and is composed of two Cremat preamplifiers lodged in the same box as the crystal as shown in Fig.4.1, while the amplifier and power supply are separated from the crystal box. The detector's best working condition requires a voltage of 153 V.
The detector readout electronics makes it possible to read both the signal from the anode and the cathode after the pre-amplification stage and after the amplification.
Fig.4.2 and 4.3 show respectively the pre-amplified signal obtained using an oscilloscope and a ^{137}Cs gamma source.

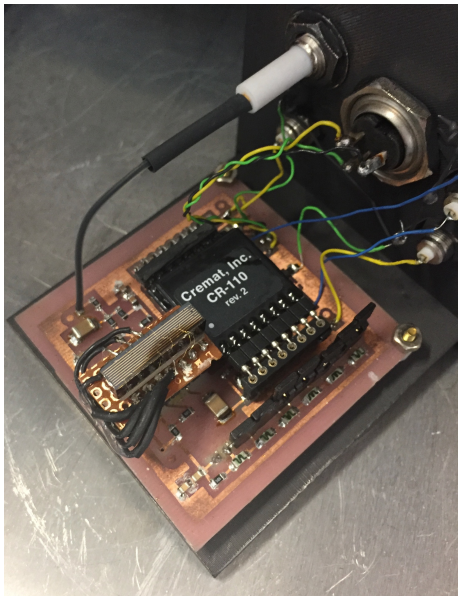

Figure 4.1: CZT detector and preamplifiers.

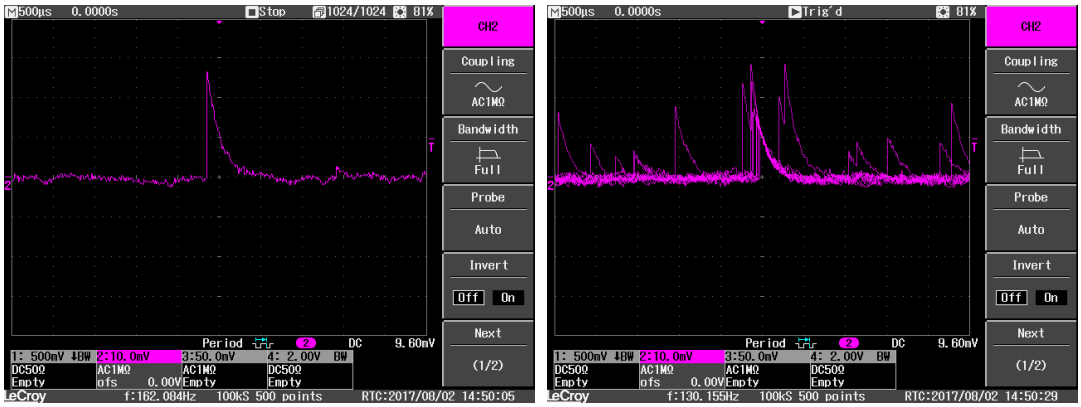

Figure 4.2: Anodic pre-amplified signal of a ^{137}Cs source.

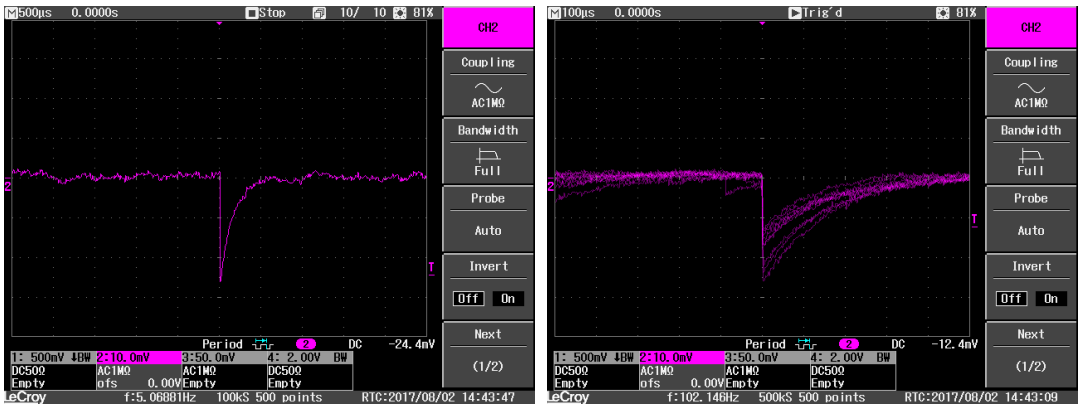

Figure 4.3: Cathodic pre-amplified signal of a ^{137}Cs source.

It is possible to see that the maximum contribution of both the anodic and the cathodic signal reaches almost 30 mV after the pre-amplification. The main difference between the two signals is due to the rate of the signal collection; due to the low mobility of the holes in the CZT crystal, as discussed in Chapter 2, the cathode collects less signals than the anode, thus the anodic signal collects more information and it is the only signal collected in all the following analysis.
The signal from the anode is then amplified as shown in Fig.4.4, the peak intensity is now 3 V, and the signal is positive.

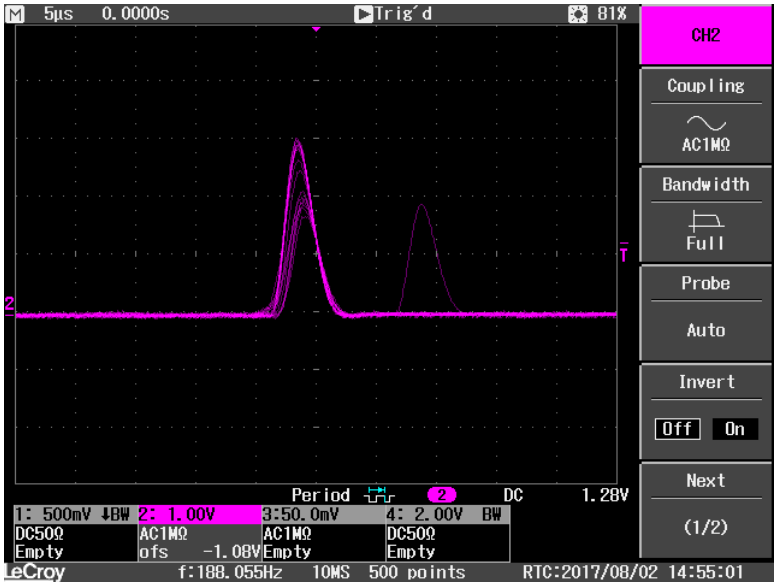

Figure 4.4: Amplified signal from the anode.

The amplified signal is then acquired using an ORTEC 926 MCB coupled with MAESTRO acquisition software.
The data was finally analyzed using ROOT5 [71].

4.1 Energy resolution

To measure the energy resolution of the detector various standard gamma sources were employed. All the sources are point-like and of known initial activity. Table 4.1 shows all the nuclides used, their characteristic energies, their branching ratios and their activity at the time of measurement. The ^{137}Cs, ^{22}Na sources were chosen because the photopeak and the annihilation peak respectively are in the energy range of interest for BNCT-SPECT thus giving a good idea of the detector performances in recording the 478 keV photon emitted during BNCT treatment. ^{133}Ba and ^{60}Co were instead chosen to probe the detector performances at energy ranges lower and higher respectively to

the range of BNCT-SPECT interest.
For the measurements the gamma source was positioned directly on the detector box in front of the 5x5 mm CZT detector surface to maximise the geometrical efficiency of the setup; the distance between the source and the detector was 1cm.

Source	Energy (keV)	Activity (kBq)	Branching ratio (%)
^{133}Ba	276	21.1	7.16
	302.8		18.34
	356		62.05
^{22}Na	511	25.65	180
	1274.5		99.9
^{137}Cs	661.6	136.9	85
^{60}Co	1173	11.47	100
	1332.5		100

Table 4.1: Standard gamma calibration sources employed in the experiment.

Pulse height spectra from ^{133}Ba, ^{137}Cs, ^{22}Na, ^{60}Co gamma sources were acquired. Fig.4.5 shows the energy spectrum obtained by the ^{133}Ba source. The spectrum clearly shows the photopeaks at 276 keV, 302 keV and 356 keV, for each peak the FWHM was measured and the energy resolution calculated (see Tab.4.2).

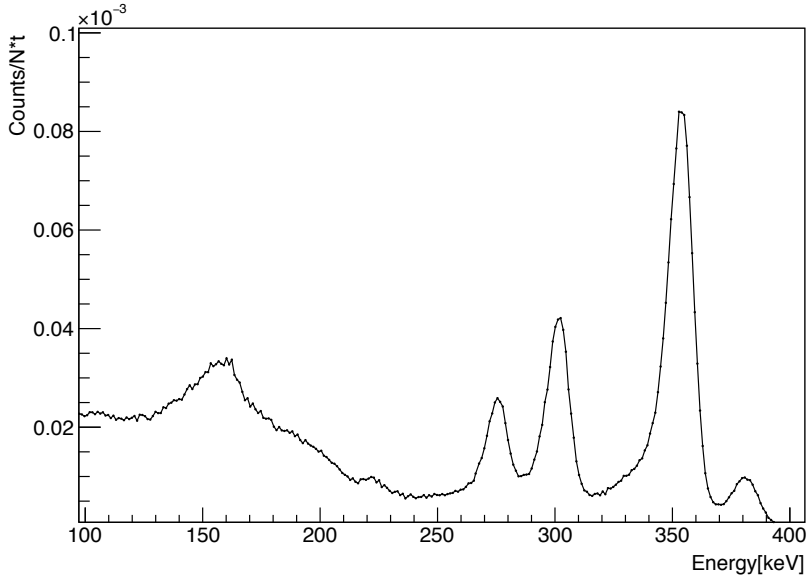

Figure 4.5: ^{133}Ba spectrum, gammas are emitted at E_1=276 keV with FWHM=8.21 keV, E_2=302.8 keV with FWHM=7.69 keV and E_3=356 keV with FWHM=10 keV

Figs. 4.6 and 4.7 show respectively the spectra for ^{137}Cs and ^{22}Na, which

Photopeak Energy [keV]	FWHM [keV]	Energy Resolution [%]
276	8.21	2.97
302.8	7.69	2.53
356	10.0	2.81

Table 4.2: FWHM and energy resolution of ^{133}Ba photopeaks

are of great interest for SPECT BNCT purposes since the photopeak from Cesium and the annihilation photons from Sodium have energies in a range close to the one considered in BNCT due to the 478 keV and 558 keV gamma rays emitted respectively by the ^{10}B and ^{113}Cd capture reactions.
The 661.6 keV photopeak from the ^{137}Cs has a FWHM of 18.62 keV and thus an energy resolution of 2.81%. In the case of the ^{22}Na the characteristic photopeak can be seen at 1274.5 keV even though the peak qualitatively shows a worse resolution than the annihilation peak. For the former the energy resolution is 2.09% (FWHM=26.66 keV) while for the annihilation peak is 2.99% corresponding to a FWHM of 15.43 keV.

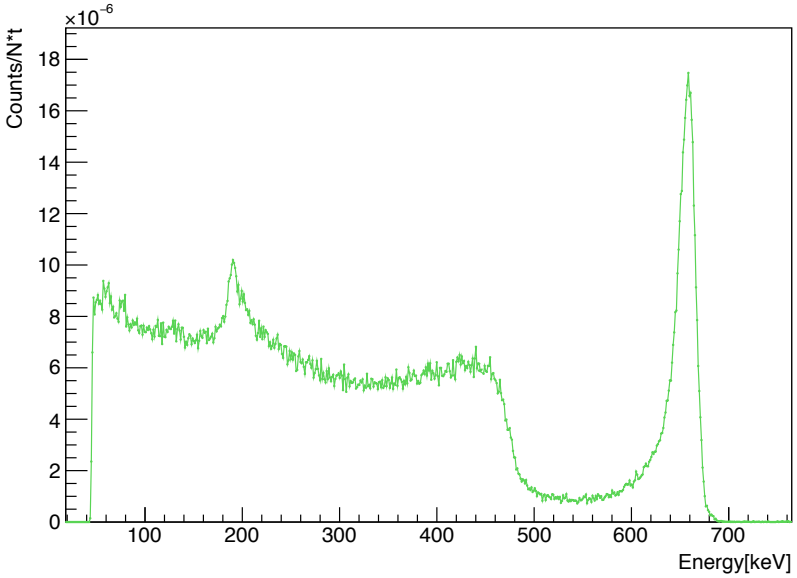

Figure 4.6: ^{137}Cs spectrum, the photopeak is at E=661.6 keV with FWHM=18.62 keV

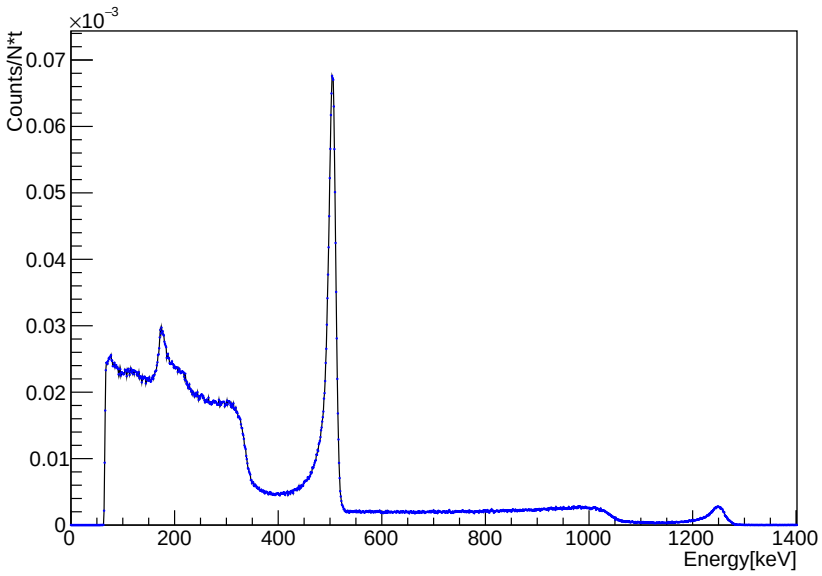

Figure 4.7: ^{22}Na spectrum, the emitted gammas are at E_1=511 keV with FWHM=15.43 keV and at E_2=1274.5 keV with FWHM=26.66 keV

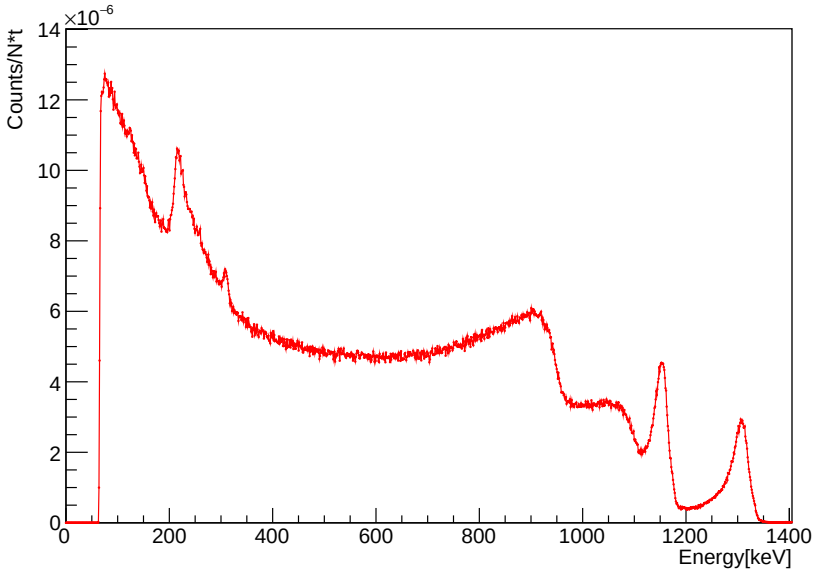

Figure 4.8: ^{60}Co spectrum, the emitted gammas are at E_1=1173 keV with FWHM=19.19 keV and at E_2=1332.5 keV with FWHM=23.65 keV

Fig.4.8 shows the spectrum acquired using a ^{60}Co source which is characterised by a double equiprobable emission at 1173 keV and 1332.5 keV, the energy range is much higher than the one of BNCT-SPECT interest nonetheless giving valuable information on the detector performances. The FWHM

of the 1173 keV peak is 19.19 keV with an energy resolution of 1.64% while for the 1332.5 keV peak the FWHM is 23.65 keV corresponding to an energy resolution of 1.78%.
The results of this first characterisation step show that at 511 keV a 5x5x20 mm^3 CZT detector irradiated on the 5x5 mm^2 surface by an isotropic point-like source has an energy resolution of 2.99% corresponding to a FWHM of 15.43 keV. Since in SPECT-BNCT we expect to have 478 keV gamma due to the boron capture reaction and a gamma at 558.5 keV due to the neutron capture reaction of the ^{113}Cd naturally present in the detector, it is of crucial importance that this two energies can be correctly distinguished. The energy resolution found in the measurements ensures the feasibility of the CZT detector to correctly identify the peak due to the boron capture reaction.

4.1.1 Comparison between simulation and measurement

The measured spectra described in the previous section were compared to the MCNP simulation of the same sources to validate the Monte Carlo model of the CZT detector.
The simulations were performed using Monte Carlo code MCNP6 [74] and recreating the experimental setup; the pulse height spectra were calculated with MCNP's F8 tally. The geometry of the simulation consisted of an isotropic gamma source in the same position with respect to the detector as the one used for the measurement as previously described. The statistical accuracy of the simulation was set to be less than 3%. The obtained spectra were analysed and compared to the measured data using the CERN ROOT software.
The characteristic spectrum from a CdZnTe detector has a not gaussian photo-peak due to the low mobility of the holes, therefore the peak has a tail in the lower energy region.
To better compare the spectra from the simulation and those from the measurement a rebinning technique was implemented. Using the FWHM measured for each source during the experiment a fixed bin width was applied to both spectra. The areas of the simulated and measured photo-peaks were compared to ensure that the simulated results and the measured data were comparable. The calculation of the area under the photo-peak showed that the simulation of a 5x5x20 mm^3 CZT detector overestimated the actual measurement results. To obtain simulation results comparable to the measurements we had to reduce the detector volume to 5x3x20 mm^3. Qualitatively the results can be seen in Fig. 4.9 and Fig. 4.10. These results show that the intrinsic efficiency for the photopeak interaction is around 60% which is comparable to the material intrinsic efficiency given by the major CdZnTe detector production companies. Moreover Fig. 4.11 shows a simulation of the electric field inside the 5x5x20 mm^3 CZT detector. It is possible to see that more than one mm of the detector has a low electric field and thus doesn't collect the charges properly. This could also cause a lower detection efficiency.

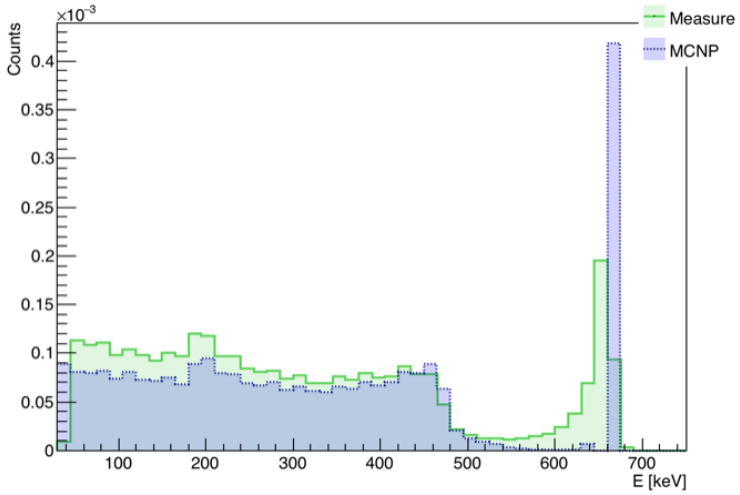

Energy	662 keV
Measure Net Area	5.5 * 10⁻⁴
MCNP Net Area	5.1 * 10⁻⁴

Figure 4.9: ^{137}Cs measurement and MCNP simulation spectra after the rebinning and values of area under the photopeak.

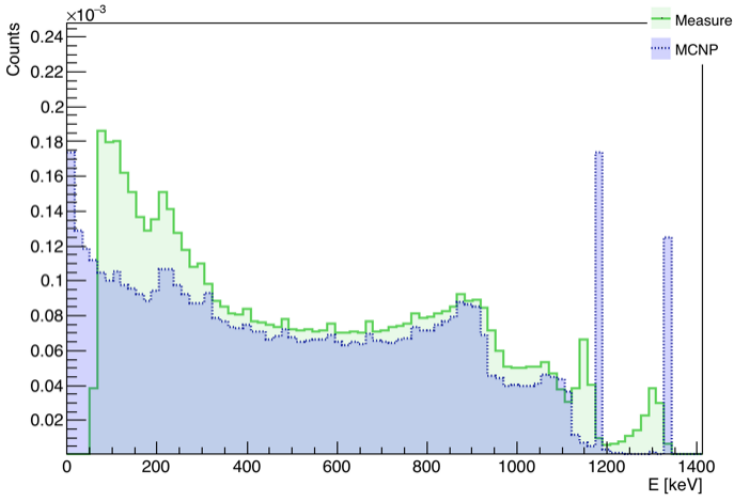

Energy	1173 keV	1332 keV
Measure Net Area	2 * 10⁻⁴	1.4 * 10⁻⁴
MCNP Net Area	2.5 * 10⁻⁴	1.3 * 10⁻⁴

Figure 4.10: ^{60}Co measurement and MCNP simulation spectra after the rebinning and values of area under the photopeak.

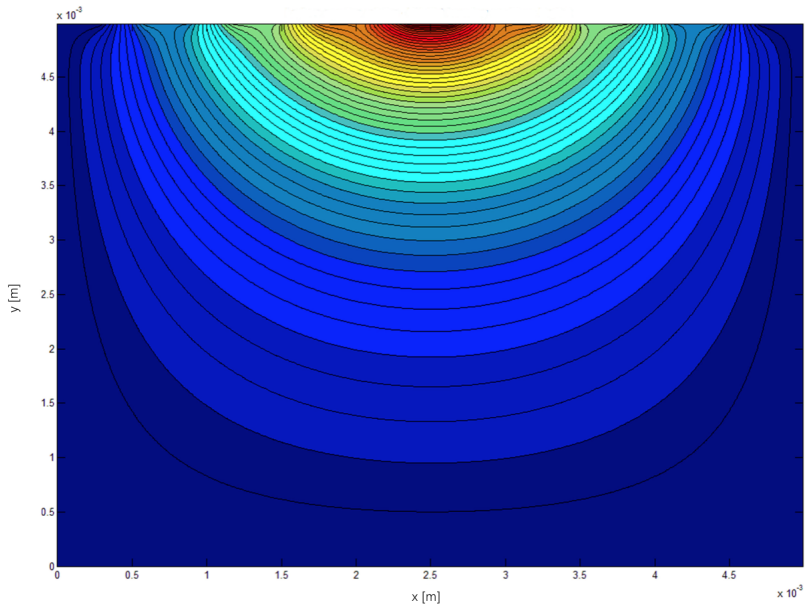

Figure 4.11: Simulation of the electric field inside the 5x5x20 mm^3 CZT detector, red shows the maximum electric field while blue shows the minimum. The electric field was obtained assuming the collecting anode was at 1 V potential and the cathode was kept at ground potential.

4.2 Detection Efficiency

As said in the previous Chapter the intrinsic efficiency ϵ_i of a detector is defined as the number of detected photons over the number of gammas incident on the detector, i.e. the number of photons emitted by the source multiplied by the geometrical efficiency ϵ_g as in equation 4.1. Therefore an high quality detector must maximise the number of detected photons. CZT detector has high Z material thus being able to absorb a high number of gamma rays to improve the detection efficiency.

$$\epsilon_i(E) = \frac{detected\ \ photons}{emitted\ \ photons \cdot \epsilon_g} \tag{4.1}$$

Equation [4.1] assumes a different form when used for measurement or simulation. To calculate the efficiency of the detector from the experimental data the activity of the source has to be taken into account while for the simulation the results are already normalized for source particle.
Eq [4.2] is used to find the experimental detection efficiency, where N(E) are the counts per second under the photopeak, i.e. the full energy absorption, B.R. is the branching ratio of the considered gamma ray, A(t) is the source activity at the time of the measurement expressed as $A(t) = A_0 e^{-\lambda \cdot t}$, which can be calculated using the initial activity A_0 given by the source producer

and taking into account the source half-life, last ϵ_g is the geometric efficiency.

$$\epsilon_i(E) = \frac{N(E)}{B.R. \cdot A(t) \cdot \epsilon_g} \tag{4.2}$$

To calculate the simulated efficiency of the detector eq [4.3] is used.

$$\epsilon_i(E) = \frac{R(E)}{B.R. \cdot \epsilon_g} \tag{4.3}$$

R(E) is the result given by the computation performed with MCNP code which counts the particles detected by the simulated CZT volume and normalizes the result to source particle.
In both cases the geometric efficiency of the detector can be expressed as the solid angle Ω over 4π, and since the CZT detector is placed at 1 cm from the source and its surface is very small Ω can be approximated as $\Omega \sim \frac{Area_{CZT}}{4 \cdot \pi \cdot d^2}$ where d is the distance between the source and the detector. In our experimental setup $\epsilon_g = 0.019$. The geometrical efficiency was also simulated using MNCP6 and we found that the simulated efficiency was $\epsilon_{g\ sim} = 0.0187$.
Finally for the measurement the error is calculated as shown in eq. [4.4] where $\left(\frac{\Delta N}{N}\right)$ is calculated as $\frac{\sqrt{N}}{N}$ which is the relative error associated to the counts under the photopeak, $\left(\frac{\Delta A(t)}{A(t)}\right)$ is the relative error associated to the calculation of the source activity at the time of the measurement which basically depends on the uncertainty of the initial activity as reported by the producer and $\left(\frac{\Delta \epsilon_g}{\epsilon_g}\right)$ is the relative error associated to the geometric efficiency due to variation in the source positioning, in this experiment considered to be 5%.

$$\Delta(\epsilon_i(E)) = \sqrt{\left(\frac{\Delta N}{N}\right)^2 + \left(\frac{\Delta A(t)}{A(t)}\right)^2 + \left(\frac{\Delta \epsilon_g}{\epsilon_g}\right)^2} \cdot \epsilon_i \tag{4.4}$$

Table 4.3 shows the results obtained in the experiment which are also plotted in Fig.4.12 and fitted with a function $\epsilon_i = a \cdot E^b$ with $a = (3.2 \pm 2.2) \cdot 10^6$, $b = (-2.14 \pm 1.04)$ and $\chi^2 = 6.16$
The results show a detection efficiency of 4.3% for the 511 keV gamma emitted by the ^{22}Na source and a detection efficiency of 2.9% for the ^{137}Cs source; as previously said this two peaks are the closest to the energy range of BNCT-SPECT; the efficiency for the 478 keV peak calculated from the fit is 6.08% so the results show a good efficiency of the CZT prototype even though the electronics of the device have great improvement possibility.

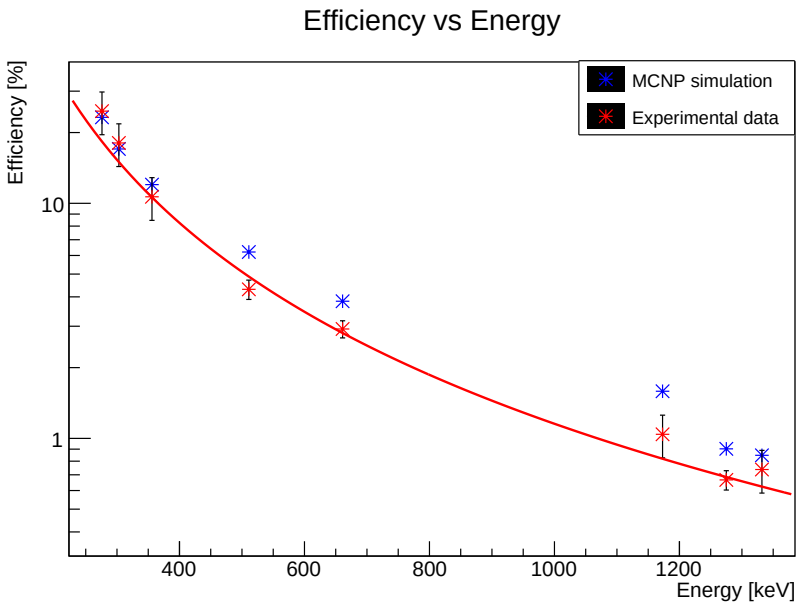

Figure 4.12: 5x5x20 mm^3 CZT prototype detection efficiency.

Source	Energy [keV]	Net Area	time [s]	A(t) [kBq]	$\frac{\Delta A(t)}{A(t)}$ [%]	ϵ_i [%]	$\Delta\epsilon_i$
^{133}Ba	276	37025	5200	21.1	20	24.7	5.1
^{133}Ba	302.8	68894	5200	21.1	20	18.1	3.7
^{133}Ba	356	137775	5200	21.1	20	10.7	2.2
^{22}Na	511	410222	10800	25.65	8	4.3	0.4
^{137}Cs	661.6	58174	900	136.9	6.7	2.9	0.2
^{60}Co	1173	153742	67777	11.47	20	1.0	0.2
^{22}Na	1274.5	34694	10800	25.65	8	0.7	0.1
^{60}Co	1332.5	108895	67777	11.47	20	0.7	0.2

Table 4.3: Experimental data and detection efficiency of CZT prototype

4.3 Geant4 simulation

The simulation study of the CZT prototype detector was also carried out using Geant4 simulation toolkit [69, 70]. This study was conducted in collaboration with Ph.D. student Chunhui Gong and Nanjing University of Aeronautics and Astronautics.

The simulation setup was the same as the measurement, the isotropic source was positioned at 1 cm from the detector. Main difference from the MCNP6 simulation was that the source was implemented as a decaying nuclide not just as a mono-energetic photon emitter.

The geometry of the detector was maintained as a 5x3x20 mm^3 crystal to take

into account the material inhomogeneity and the partial collection due to the electric field inside the detector. Fig.4.13, Fig. 4.14, Fig. 4.15 and Fig. 4.16 show the comparison between the Geant4 simulation, the experimental spectra and the MCNP6 simulation for all the used sources.

Qualitatively the spectra are correctly simulated with Geant4 simulation

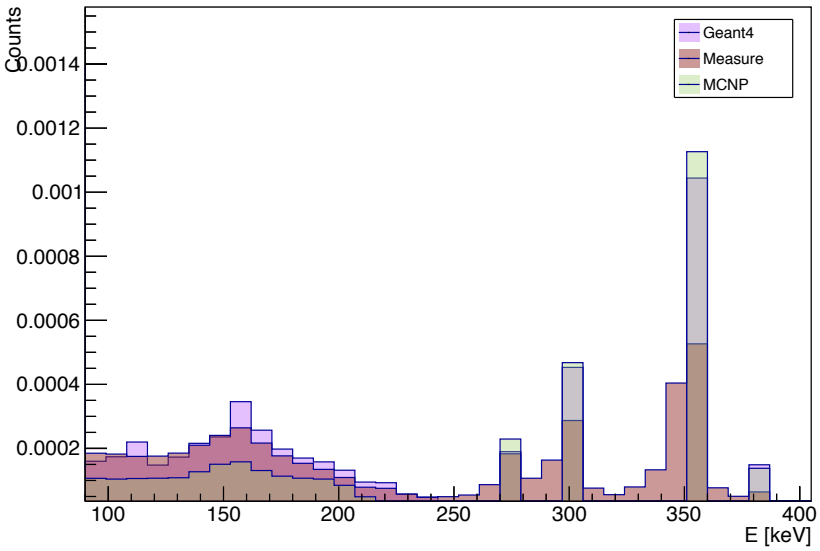

Figure 4.13: Comparison of Geant4 simulation, MCNP6 simulation and experimental data for ^{133}Ba source.

toolkit, the main difference between the two simulations is recognisable in Fig. 4.14 where Geant4 simulation takes into account the cesium nuclide emission at low energies.
To quantitatively asses the performances of the Geant4 simulation the efficiency calculated from these simulated data was considered.
Fig. 4.17 shows the comparison of the efficiency calculated using the experimental data and the simulations with MNCP6 and Geant4. It is possible to see that the values obtained by Geant4 simulation are in good accordance with the experimental data thus confirming that also Geant4 is a suitable simulation toolkit for these studies.

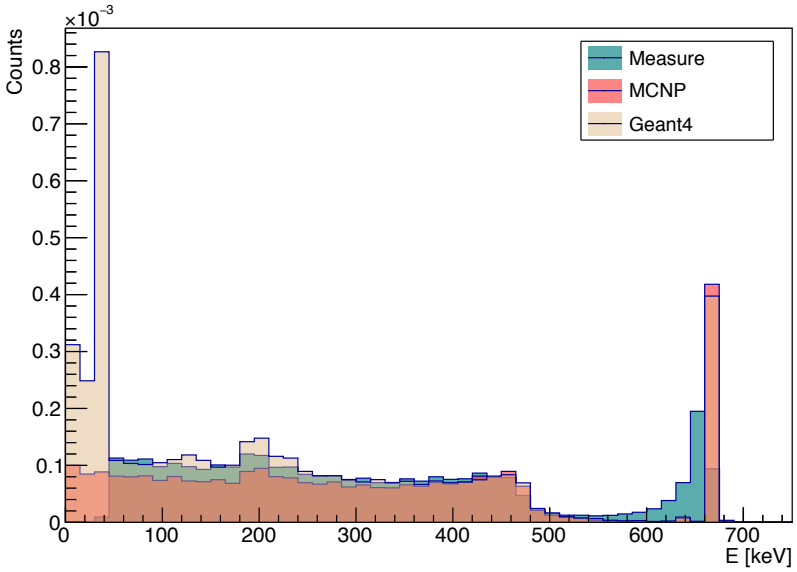

Figure 4.14: Comparison of Geant4 simulation, MCNP6 simulation and experimental data for ^{137}Cs source.

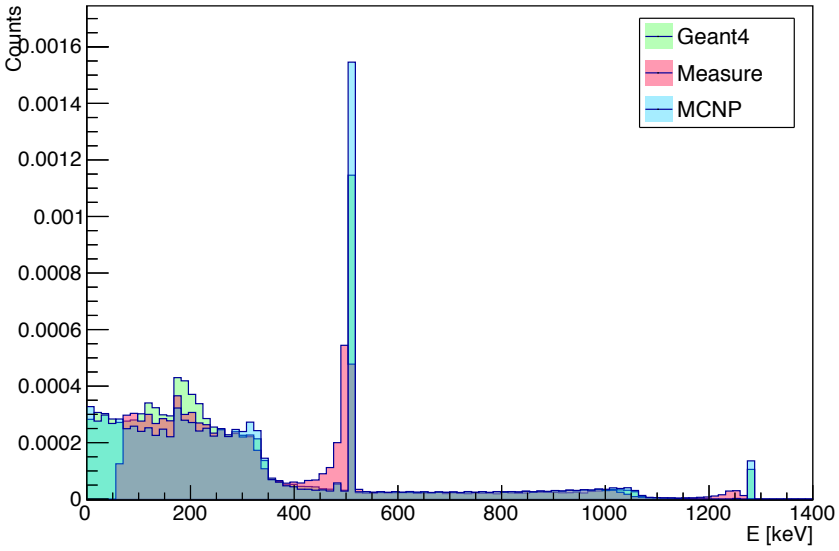

Figure 4.15: Comparison of Geant4 simulation, MCNP6 simulation and experimental data for ^{22}Na source.

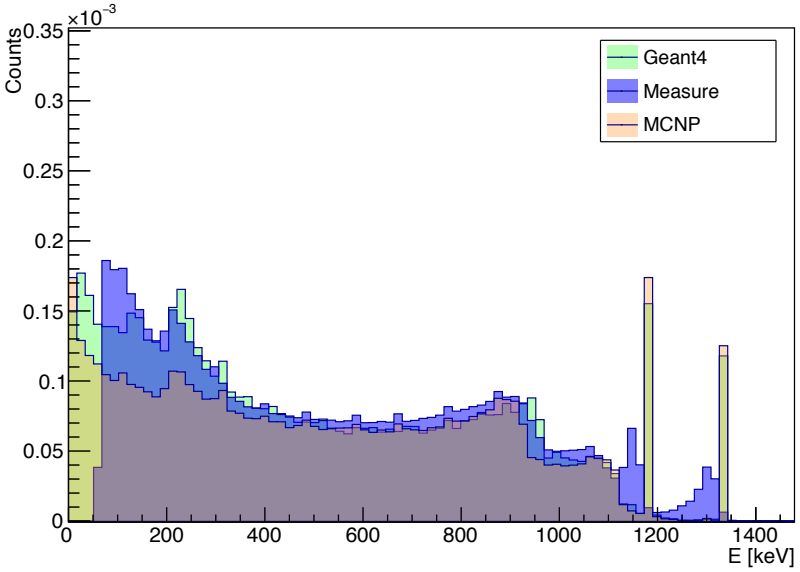

Figure 4.16: Comparison of Geant4 simulation, MCNP6 simulation and experimental data for ^{60}Co source.

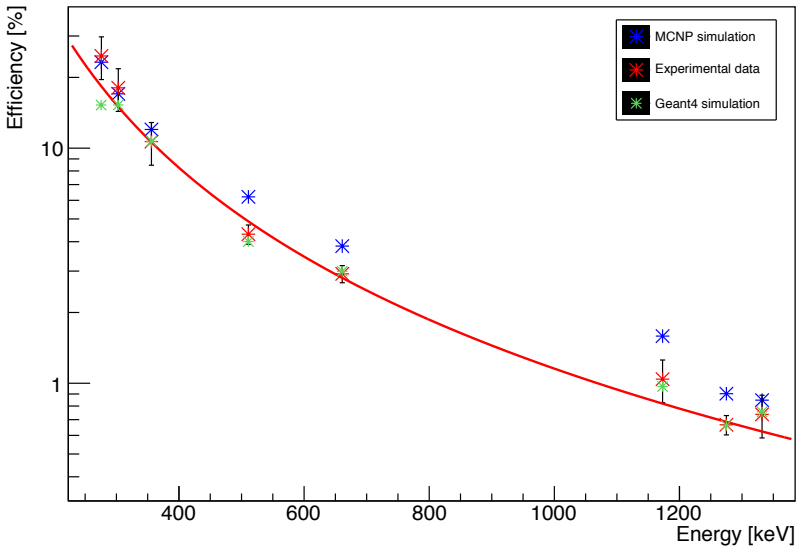

Figure 4.17: Comparison of Geant4 simulation, MCNP6 simulation and experimental efficiency.

Chapter 5

CZT detector prototype measurements in TRIGA Mark II Thermal Column

Chapter 4 shows the characterization of the 5x5x20 mm^3 prototype detector with standard gamma sources to evaluate the detector energy resolution and efficiency. In this chapter we focus on the study of the behaviour of the detector when it is in presence of a photon and neutron mixed background field.
This studies were performed in the Thermal Column of the TRIGA Mark II (Training, Research, Isotopes, General Atomics) research reactor of L.E.N.A. (Laboratorio di Energia Nucleare Applicata) laboratory of University of Pavia.
TRIGA Mark II reactors are non-power nuclear reactors commonly used for research purposes. The TRIGA MArk II reactor is an open-pool thermal reactor with light water moderation and cooling; its nominal steady-state power is 250 kW.
University of Pavia reactor reached its first criticality the 15^{th} of November 1965 and has since been active for various research purposes including BNCT studies.

5.1 The Pavia TRIGA Mark II reactor

The TRIGA Mark II reactor installed in Pavia has 83 fuel rods located in five concentric rings, each rod is a cylinder of 5 cm diameter and 72.5 cm height. The whole core is also a cylinder of 45.7 cm diameter and 55.9 cm height.
Each fuel rod has a 0.76 mm thick cladding made of steel or aluminium. The nuclear fuel is composed of 20% enriched ^{235}U uranium and zirconium hydride ZrH_2; the uranium is dispersed in zirconium hydride and the weight of the two components is respectively 8% and 92%.
Hydrogen is exploited as a neutron moderator while zirconium has a low mi-

croscopic neutron capture cross section. Zirconium hydride moderation effect is highly dependent of the nuclear fuel temperature and has a negative temperature reactivity feedback thus acting as a passive safety system. As the temperature of the fuel increases the moderating effect of the hydrogen is decreased while the upscatter raises thus the thermal neutron population gets lower and a prompt negative reactivity is inserted.
Among the core rods there are some "dummy" rods that contain graphite and are used as reflectors for the fission neutrons. A typical core of a TRIGA reactor is shown in Fig. 5.1.
The core is surrounded by a 30.5 cm thick neutron reflector made of nuclear-

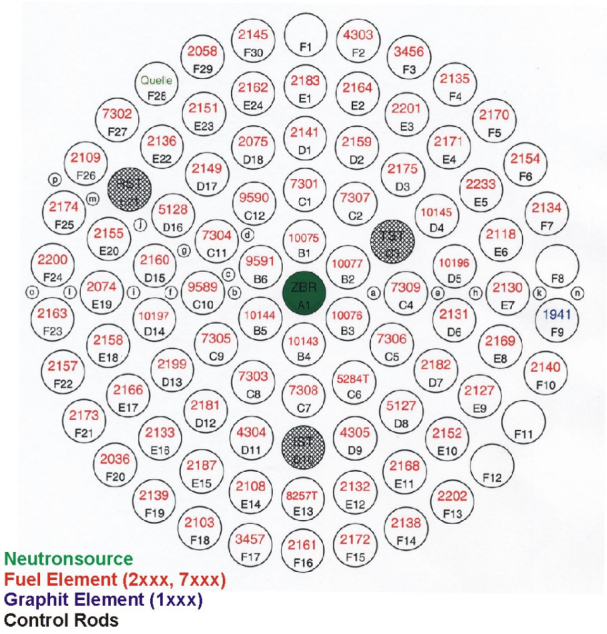

Figure 5.1: Standard TRIGA Mark II core [75].

grade graphite, the reflector is covered in aluminium to avoid the contact with the water coolant. The tank of the reactor is an aluminium cylinder of 2 m diameter and 6.55 m height that contains the core, the reflector and cooling water. The structure is surrounded by the biological shielding made of concrete to absorb all the thermal neutrons; the lower part is a parallelepiped of 3.60 x 6.95 x 8.65 m^3 volume and has an upper level shaped as a octagon base prism of 2.87 m height.
Fig. 5.2 shows the L.E.N.A. reactor core and the surrounding reflector and biological shielding. Moreover it is possible to see the four irradiation channels, three are radial and one is tangential. Channel A and D are penetrating since they cross also the graphite reflector. Channel B ends before the reflector and Channle C is tangential to the reflector surface and reaches the face of channel D. The neutron flux in the penetrating channels has a high component of fast neutrons while the neutron flux in Channel B is more thermalized.

For our experiments we used the thermal column of the reactor which starts

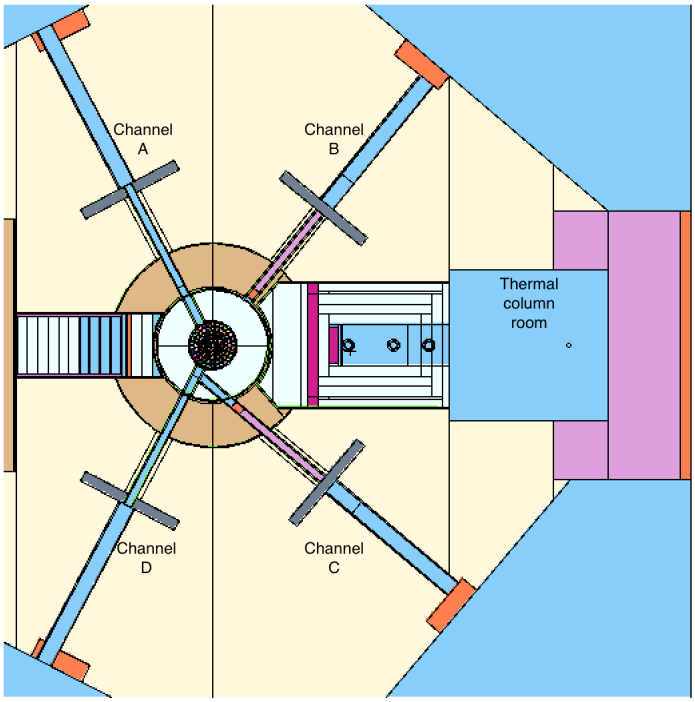

Figure 5.2: MCNP geometry of the TRIGA Mark II reactor of University of Pavia.

outside the reflector and is located in between Channel B and C; it penetrates the concrete shield and the tank container. The thermal column is made by two parts, the first part closer to the core is an aluminium container of 1.22 x 1.68 x 1.22 m^3 volume with an inside coating of a 0.3 cm thick Boral layer and filled with graphite blocks and bismuth layers that reduce the gamma rays due to the nuclear fission in the core. Inside the graphite an irradiation chamber of 1 x 0.4 x 0.2 m^3 was created to house the TAOrMINA project [76, 77]. To close the irradiation chamber a 1 cm thick boral shield is used. The shield has a window opening of 40 x 20 cm^2 that allows the user to put the sample in the irradiation chamber. After the Boral shield a room of 1.40 x 1.48 x 1.68 m^3 volume was created. The thermal column room is closed by a movable concrete door and a pair of movable shutters installed at 82 cm from the Boral shield.

5.2 Neutron beam design

As previously described we used the thermal column room to perform our experiments. The neutrons reach the thermal column room through an aperture of 20 x 40 cm^2 that can be closed with a Boral sliding window or kept open as can be seen in Fig. 5.3. The main disadvantage of such neutron irradiation

room is that does not allow to irradiate a boron target while keeping the detector out of beam.
To be able to perform the tests on our 5x5x20 mm^3 prototype CZT detector we needed to create a small neutron irradiation beam. Some solutions were studied using MCNP6 Monte Carlo code in collaboration with Ph.D. student Chunhui Gong and Nanjing University of Aeronautics and Astronautics.

The source was obtained using MCNP's criticality calculation (KCODE),

Figure 5.3: Image of the L.E.N.A. thermal column room with details of the 20 x 40 cm^2 irradiation chamber and the Boral shield with its sliding window.

modelling the fission reaction inside the fuel elements as it described by Bortolussi et al. [78] and then it was modified using the Surface Source Card as described by Gong et al. [79].
The first configuration implemented to create a smaller neutron beam employed nuclear grade graphite to exploit its low thermal neutron absorption cross section and its high scattering cross section [80], therefore the employment of graphite should allow for a high thermal neutron flux focused on a smaller neutron beam.
The simulation took into account the dimensions of the graphite blocks that could in reality be used to modify the thermal column, as such the neutron beam would be a rectangular aperture of 3 x 5 cm^2.
The second configuration employed nuclear grade graphite as the previous one but to reduce the thermal neutron flux outside the neutron beam a 0.5 cm thick layer of Boral was added around the graphite.
In both cases a F4 tally was used to calculate the neutron and photon flux on the neutron beam aperture. The neutron energies employed were ($< 4.14 \cdot 10^{-7}$) MeV for the thermal neutrons, ($4.14 \cdot 10^{-7}$ - $1.07 \cdot 10^{-5}$) MeV and ($1.07 \cdot 10^{-5}$ - $1.58 \cdot 10^{-3}$) MeV for the epithermal neutrons and ($1.58 \cdot 10^{-3}$

- $1.73 \cdot 10$) MeV for the fast neutrons.
For the photons the tallied energies of our interest were the (0.450 - 0.500) MeV bin that included the flux due to the 478 keV photon emitted by the boron capture reaction and the (2.1 - 2.3) MeV bin that included the 2.2 MeV gamma due to the hydrogen capture reaction.
Tab.5.1 shows the neutron and gamma flux values calculated on the neutron beam aperture in first setup.

In the first setup the thermal neutron flux on the neutron beam is three

	Energy [MeV]	Flux [cm^{-2} s^{-1}]
Neutrons	$< 4.14 \cdot 10^{-7}$	$1.05 \cdot 10^{8}$
	$4.14 \cdot 10^{-7}$ - $1.07 \cdot 10^{-5}$	$4.16 \cdot 10^{5}$
	$1.07 \cdot 10^{-5}$ - $1.58 \cdot 10^{-3}$	$4.95 \cdot 10^{5}$
	$1.58 \cdot 10^{-3}$ - $1.73 \cdot 10$	$5.37 \cdot 10^{5}$
Photons	0.450 - 0.500	$2.38 \cdot 10^{6}$
	2.1 - 2.3	$1.20 \cdot 10^{5}$
	Total	$4.01 \cdot 10^{7}$

Table 5.1: Neutron and photon flux values in various energy bins calculated at the end of the irradiation chamber in the first setup.

orders of magnitude higher than the flux of epithermal and fast neutrons. The main concern lays in the presence of a high photon flux mostly due to photons coming from the interaction of thermal neutrons on the Boral plates. These photons are mostly present in the first 20 cm around the neutron beam which is the most probable position for the CZT detector in our measurements, and thus they represent an obstacle that must be taken into account to avoid their spurious contribution to the CZT acquired spectra.
Tab.5.2 shows the neutron and gamma flux values calculated on the neutron beam aperture for the second setup.

In the second setup the thermal neutron flux on the neutron beam is lower

	Energy [MeV]	Flux [cm^{-2} s^{-1}]
Neutrons	$< 4.14 \cdot 10^{-7}$	$2.52 \cdot 10^{7}$
	$4.14 \cdot 10^{-7}$ - $1.07 \cdot 10^{-5}$	$3.13 \cdot 10^{5}$
	$1.07 \cdot 10^{-5}$ - $1.58 \cdot 10^{-3}$	$3.66 \cdot 10^{5}$
	$1.58 \cdot 10^{-3}$ - $1.73 \cdot 10$	$5.37 \cdot 10^{5}$
Photons	0.450 - 0.500	$2.95 \cdot 10^{6}$
	2.1 - 2.3	$1.10 \cdot 10^{5}$
	Total	$4.59 \cdot 10^{7}$

Table 5.2: Neutron and photon flux values in various energy bins calculated at the end of the irradiation chamber in the second setup.

than the one found in the previous configuration, it is just two orders of mag-

nitude higher than the flux of epithermal and fast neutrons.
This configuration has the advantage of having a lower flux of neutrons directly interacting on the CZT detector thus allowing for a smaller neutron shielding but has a high amount of 478 keV photons.
The last configuration studied was the one then chosen for the measurements. This simulation used natural Lithium Polyethylene (LiPoly) to create a smaller neutron beam of diameter 4 cm. LiPoly is employed for the high capture cross section and the low amount of capture gammas emitted, even though the Li capture cross section is lower than the B one, the advantage of having a lower gamma background is fundamental in our experiment.

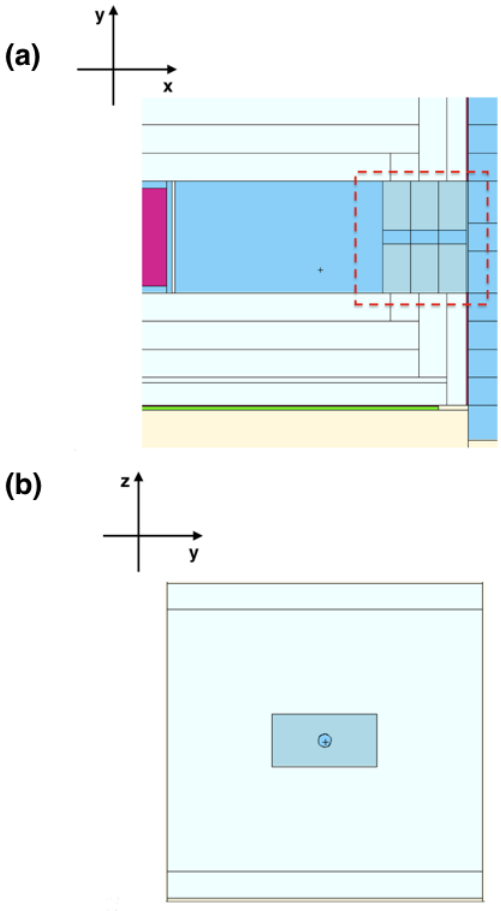

Figure 5.4: MCNP6 geometry of the irradiation chamber modified using 30 cm of LiPoly: (a) longitudinal section of the irradiation chamber and b) sagittal section view of the new neutron beam aperture of 4 cm diameter.

Fig.5.4 shows the MCNP6 geometry of this simulation. In this case the Lithium polyethylene slabs occupied 30 cm inside the irradiation chamber. The neutron and gamma flux were calculated using a MESH tally type 4 by dividing the thermal column room in cubes of edge lengths 5 cm thus the flux

is mediated on such volume. As in the previous case all the results were considered viable if the relative error was $\leqslant 10\%$.

Tab.5.3 shows the neutron and gamma flux values calculated on the neutron beam aperture with an F4 tally while Fig.5.5 and Fig.5.6 show the neutron flux in the irradiation chamber while Fig.5.7 and Fig.5.8 show the 2.2 MeV photon flux and the 478 keV photon flux in the (y,z) plane, i.e. the plane in which the neutron beam lays.
The thermal neutron flux on the neutron beam is slightly lower than the one

	Energy [MeV]	Flux [cm^{-2} s^{-1}]
Neutrons	$< 4.14 \cdot 10^{-7}$	$2.48 \cdot 10^{7}$
	$4.14 \cdot 10^{-7}$ - $1.07 \cdot 10^{-5}$	$2.70 \cdot 10^{5}$
	$1.07 \cdot 10^{-5}$ - $1.58 \cdot 10^{-3}$	$2.71 \cdot 10^{5}$
	$1.58 \cdot 10^{-3}$ - $1.73 \cdot 10$	$2.84 \cdot 10^{5}$
Photons	0.450 - 0.500	$3.05 \cdot 10^{5}$
	2.1 - 2.3	$1.18 \cdot 10^{6}$
	Total	$1.90 \cdot 10^{7}$

Table 5.3: Neutron and photon flux values in various energy bins calculated at the end of the irradiation chamber modified by the insertion of 30 cm of Lithium Poly.

found in the previous configuration, it is two orders of magnitude higher than the flux of epithermal and fast neutrons but as shown in Fig. 5.5 when the flux is mediated on a 5 cm width edge cube the neutron flux in front of the beam is much higher than the one in the surrounding cubes. This configuration has the advantage of having a low flux of neutrons directly interacting on the CZT detector thus allowing for a smaller neutron shielding. Moreover Fig. 5.6 shows the vertical behaviour of the neutron flux in the thermal column room; along the z axes, i.e. the height of the chamber, the flux is highly focused in front of the neutron beam and along the x axes the exponential flux attenuation is clearly visible. The longitudinal behaviour of the neutron flux is similar to the vertical one and it is not shown here for brevity.
The 478 keV photon flux is lower on the beam port than both the previous cases and also, as can be seen in Fig. 5.7 and 5.8, the flux in the 20 cm circle around the neutron beam is significantly reduced so we can expect less noise in the 478 keV photopeak. This is due to the employment of Lithium Polyethylene which has a low gamma capture emission.

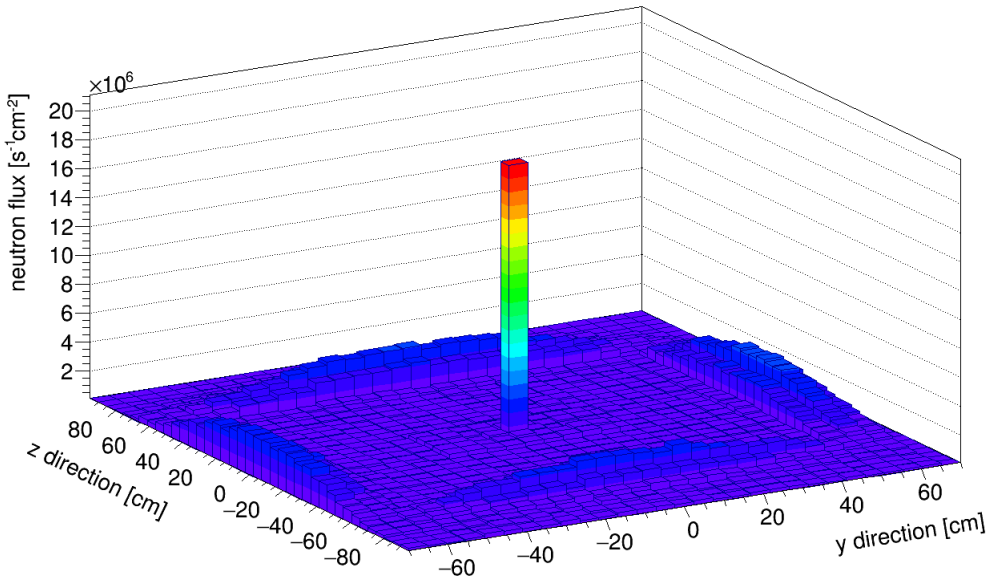

Figure 5.5: Sagittal view of the neutron flux on the neutron beam plane with natural lithium polyethylene at the end of the irradiation chamber.

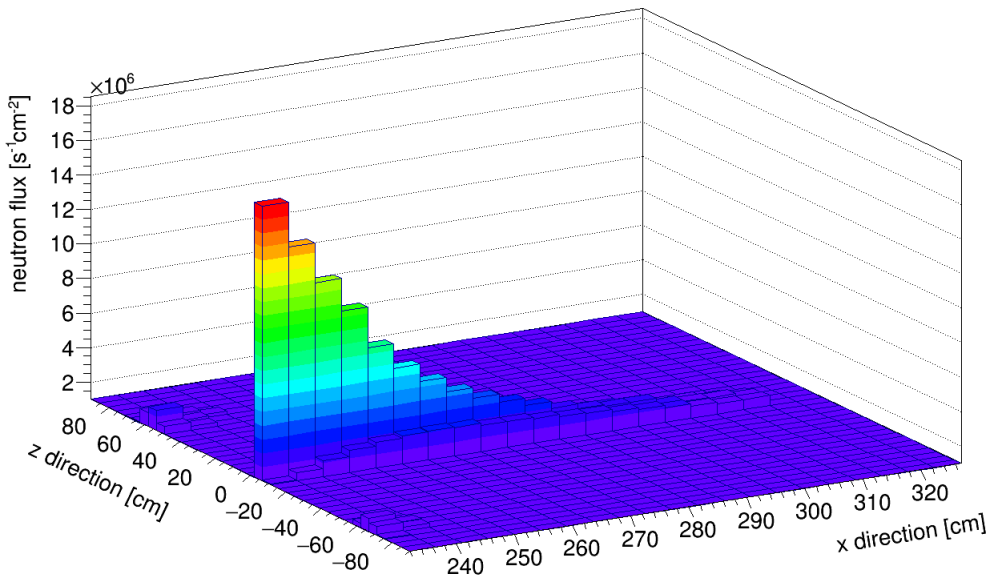

Figure 5.6: Vertical view of the neutron flux on the neutron beam axes with natural lithium polyethylene at the end of the irradiation chamber.

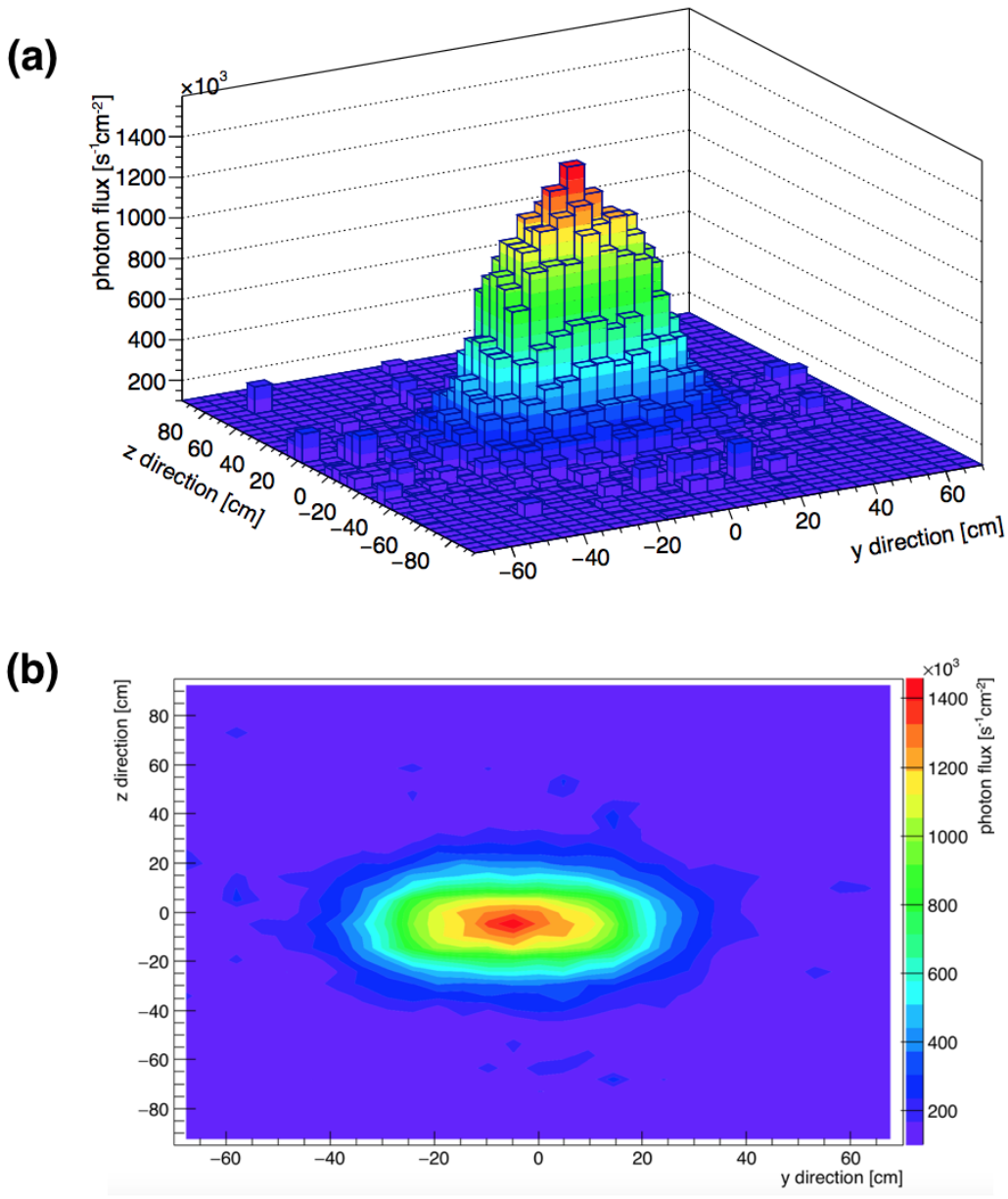

Figure 5.7: 2.2 MeV photon flux on the neutron beam plane with natural lithium polyethylene at the end of the irradiation chamber: (a) 3D view, (b) 2D view on the beam port plane.

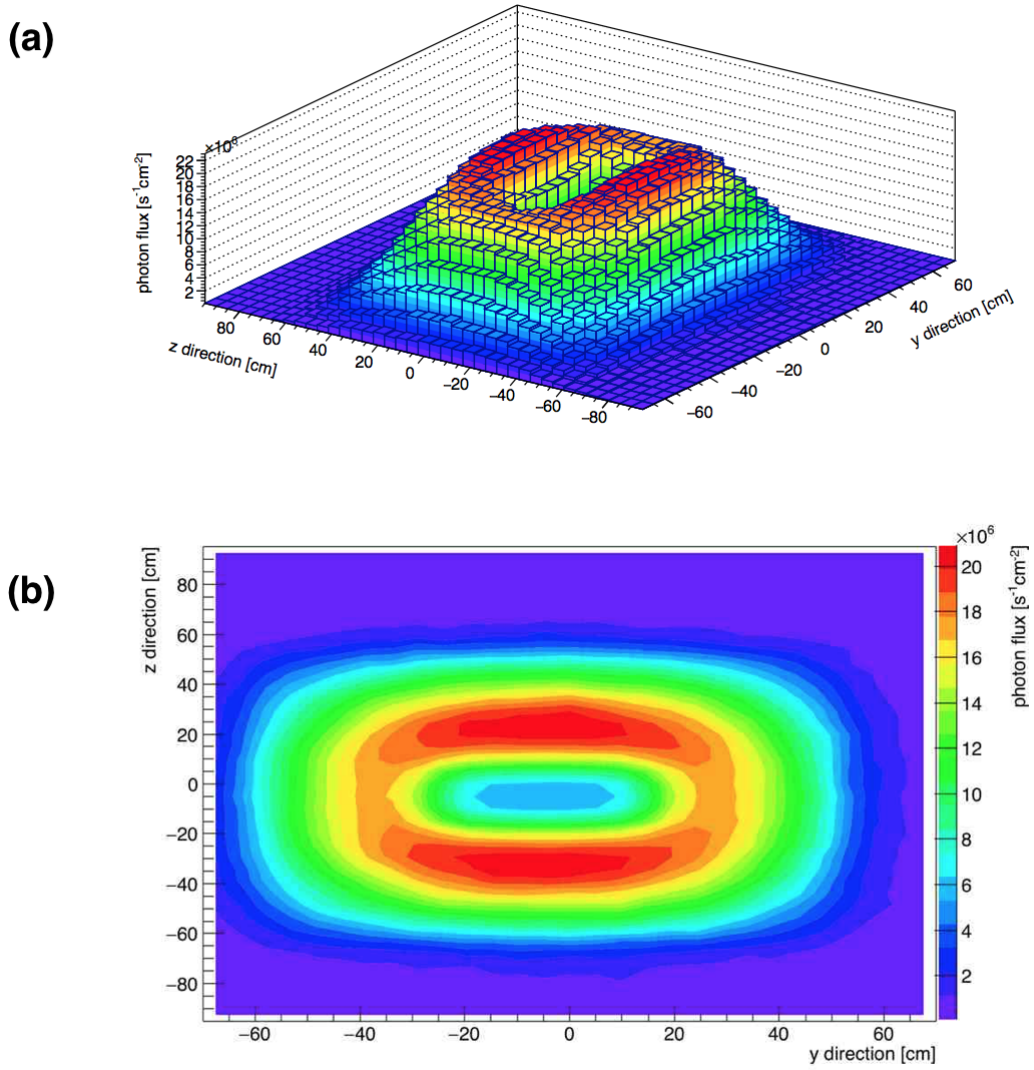

Figure 5.8: 478 keV photon flux on the neutron beam plane with natural lithium polyethylene at the end of the irradiation chamber: (a) 3D view, (b) 2D view on the beam port plane.

5.2.1 Measurements at L.E.N.A. with the current thermal column setup

The measurement campaign was carried out using the Lithium Polyethylene configuration previously simulated. Fig. 5.9 shows the irradiation chamber modification.
Even though the Lithium Polyethylene has good results for the neutron flux this configuration has a high 478 keV photon background due to the presence of the Boral shield. Nonetheless before removing the Boral shield, which is a complicated step and requires to work at lower reactor power, we acquired

some spectra using two different shielding setups and positions of the detector.
In the first case the CZT detector was positioned at 65 cm height and 26.5

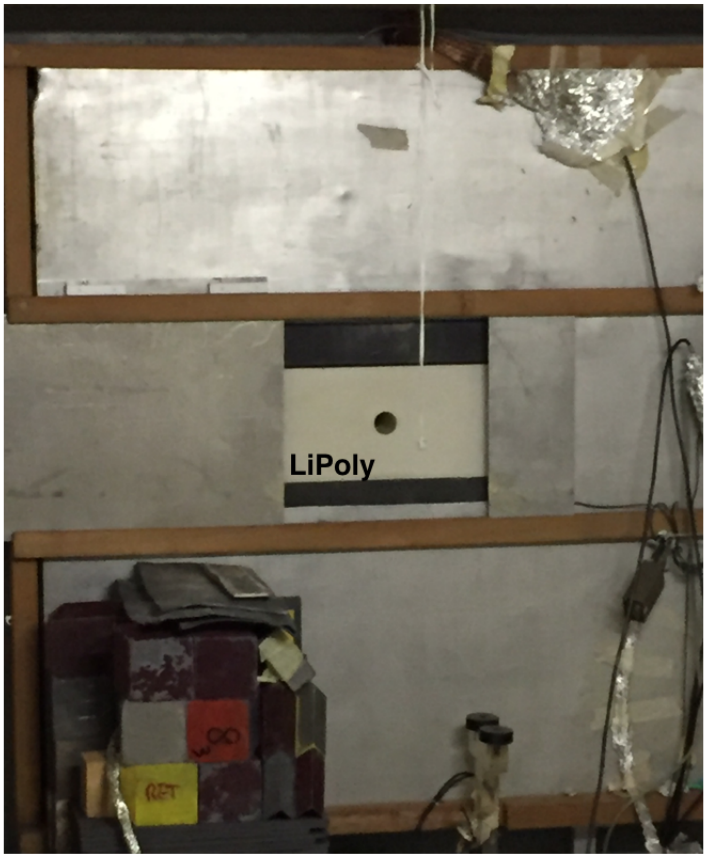

Figure 5.9: Irradiation chamber modification using 30 cm of natural Lithium Polyethylene with a 4 cm diameter neutron beam.

cm from the neutron beam, the detector was inclined at 45 degree angle to be directly faced to the vial containing boric acid and directly exposed to the escaping neutrons.
The measurement was carried out using a 10 cm thick lead shielding to try to reduce the contribution due to the 478 keV gammas coming from the Boral shield, moreover the CZT detector was also shielded from the neutrons by means of a Teflon container filled with about 800 g of Lithium Carbonate at 95% of ^{6}Li.
The measurements were taken with the reactor not at full power to keep the detector dead time low. First we acquired the background spectra at 1 kW and 10 kW to have an estimation of the 478 keV gammas due to the Boral shield. Even though the background of 478 keV gammas was very high we acquired a second spectra at 10 kW with a small vial filled with 714 mg of boric acid, containing 115 mg of ^{10}B, positioned in front of the neutron beam to act as the main ^{10}B sample.

Fig. 5.10 shows the results of the measurements at 1 kW and 10 kW reactor power. In both cases it is possible to see the peak at 478 keV due to the boron capture reaction and the peak at 511 keV due to the annihilation that takes place in the lead while the Cd capture peak is very low since the detector was shielded with the Lithium Carbonate .

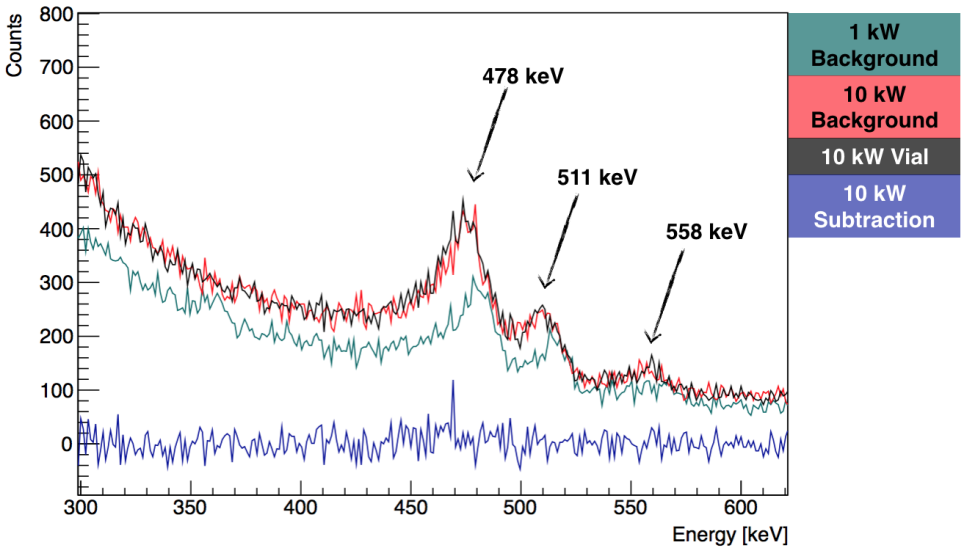

Figure 5.10: Spectra obtained at 1 kW and 10 kW reactor power. Green line represents the 1 kW background. Red line represents the 10 kW background, black line represents the contribute with a small vial of boric acid in front of the neutron beam at 10 kW power, the blue line represents the counts when the red spectrum is subtracted from the black one.

The green line represents the background at 1 kW reactor power while the red spectrum represents the background at 10 kW power, the black spectrum represents the contribution when a small vial of boric acid is positioned in front of the neutron beam at 10 kW power. Lastly the blue line is the subtraction of the background from the vial spectrum when working at 10 kW reactor power. As expected the subtraction shows that the contribution from the boric acid is negligible in respect to the 478 keV gamma background due to the Boral shield.
The results of this measurement show that the high gamma background due to the Boral shield employed in the thermal column room heavily interferes with the possibility to acquire a spectrum of the gamma capture reaction in a sample. To try and reduce the gamma contribution a new step was taken by using a thicker gamma shielding of approximately 15 cm all around the detector.

Fig. 5.11 shows the lead shielding employed for the measurements inside the thermal column room.
The detector is nested behind 15 cm of lead to suppress the 478 keV signal from the Boral shield and it is positioned right under the boric acid vial which in turn is in front of the neutron beam, to maximise the detection efficiency.

Figure 5.11: Improved lead shielding of the CZT prototype detector inside the thermal column room.

Fig. 5.12 shows the spectra obtained with reactor power 1 kW. The CZT detector was not shielded from the neutrons in this study. Once again the red spectrum shows the background, while the black spectrum shows the data acquired with the boric acid vial and the blue line shows the difference between the two.

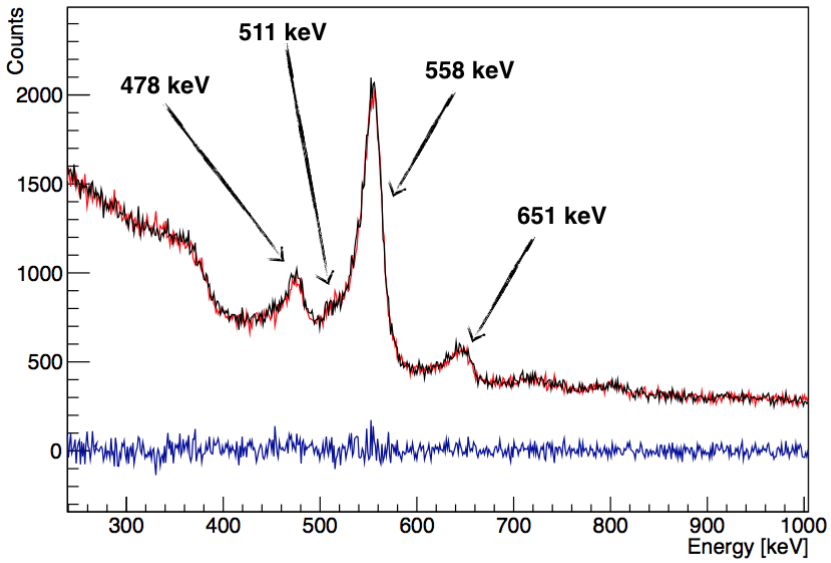

Figure 5.12: Spectra obtained at 1 kW reactor power. Red line represents the background, black line represents the contribute with a small vial of boric acid in front of the neutron beam and the blue line represents the counts when the red spectrum is subtracted from the black one.

The results show the 478 keV boron capture peak, the 511 keV annihilation peak superimposed on the 558 keV peak and the 651 keV peak, the last two are due to the Cd capture reactions now discernible since the detector was not shielded from the neutrons [81].
Once again, the presence of the Boral shield interferes heavily on the possibility to see the 478 keV boron peak due to the neutron capture reactions in the vial. These results further the necessity to remove the Boral shield to be able to correctly distinguish the contribution of the vial.

5.3 Measurements at L.E.N.A. after the modification of thermal column setup

To remove the Boral shield a simulation campaign was first taken up to understand the thermal neutron fluxes in the thermal column room and thus to understand the maximum power reachable to safely employ the reactor. It was found that to operate safely the reactor the measurements should not go above 500 W reactor power.
The simulations were also used to compute the photon background flux in the thermal column room when the Boral shield was removed.
Fig. 5.13 shows the comparison between the gamma fluxes in the 7x7x7 cm^3

cell, filled with air and centred in correspondence of the expected measuring position of the CZT calculated with an F4 tally with and without Boral shield at 300W reactor power.

The 478 keV gamma flux is an order of magnitude lower without the Boral

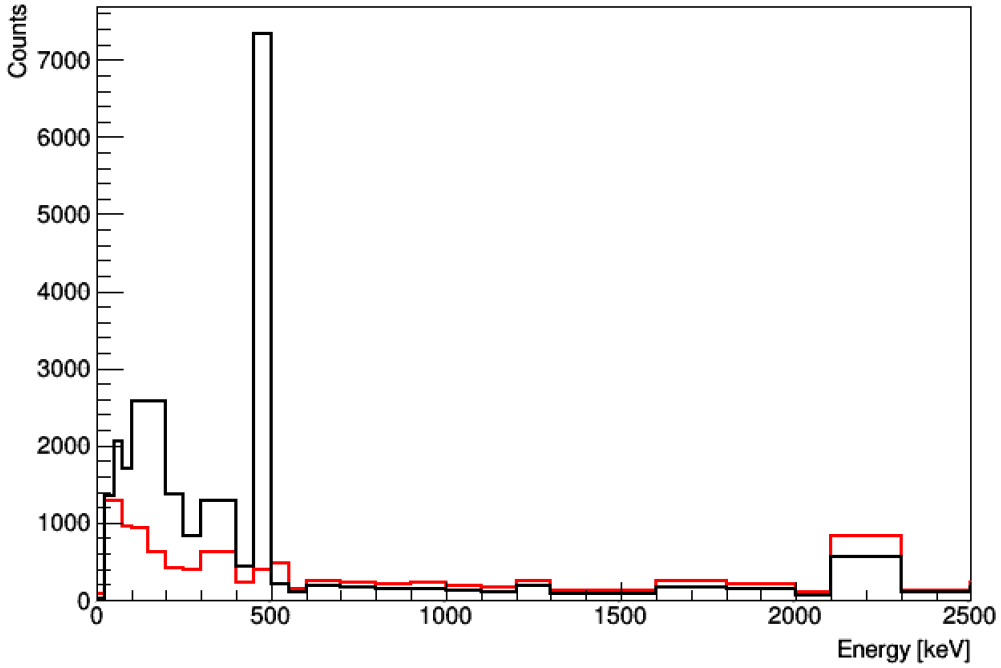

Figure 5.13: Comparison between photon fluxes in the thermal column room on the neutron beam plane with Boral shield (black) and without Boral shield (red).

shield thus lowering the noise on the energy we are interested in. Therefore the measurements campaign should include a less imposing lead shielding and still be able to detect the 478 keV gamma coming from the sample vial.
The measurements where carried out removing the Boral shield and positioning the detector at the same height of the centre of the neutron beam while the vial was positioned directly in front of the neutron beam. Fig. 5.14 shows the detector position and setup when irradiating without the Boral shielding.

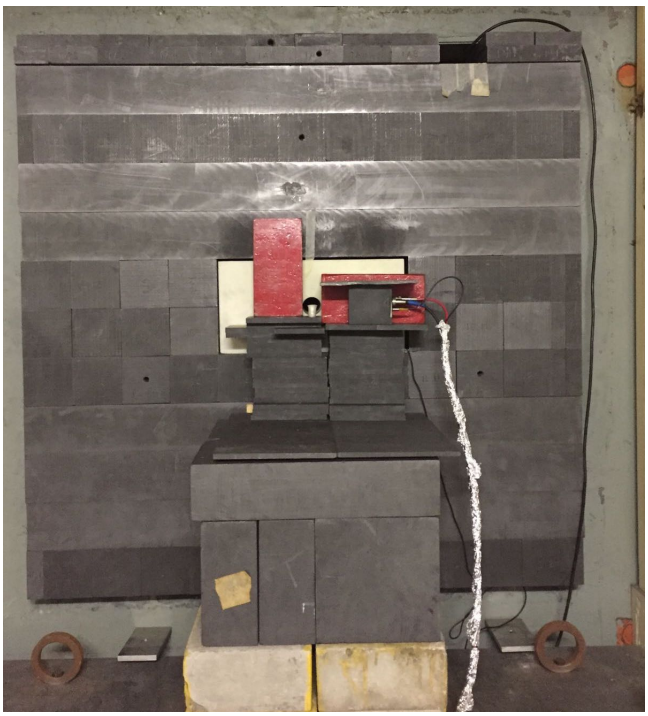

Figure 5.14: CZT prototype detector setup in the thermal column room without Boral shielding, the detector base is made of reactor grade graphite and the two red bricks are lead.

A 5 cm lead brick was used to shield the detector from the gammas coming from the reactor core side and a 1 cm thick lead shield was positioned above the detector. No neutron shielding was employed. For the sample a 1.8 g BPA vial was employed. The vial has a very high number of ^{10}B ppm and was chosen as such to ensure the signal presence in the acquired data.
The detector was tested in different positions with respect to the vial, the best performing setup is reported and consists in positioning the vial in front of the neutron beam and adjacent to the detector's box thus keeping the 1 cm minimum distance between the detector and the vial due to the box presence. Fig. 5.15 shows the results of the measurement employing the BPA vial at 300 W reactor power. The measurement had a live time of 600 s with a dead time lower than 4%.
The red spectrum represents the background of the thermal column room at 300 W reactor power and qualitatively it is possible to appreciate that the 478 keV counts are lower in the background than in the black spectrum acquired with the BPA vial. Nonetheless we were not able to completely suppress the 478 keV gammas due to the background, this is probably due to the presence of other materials containing Boron in the irradiation chamber and in the measurement room that is not possible to work without.

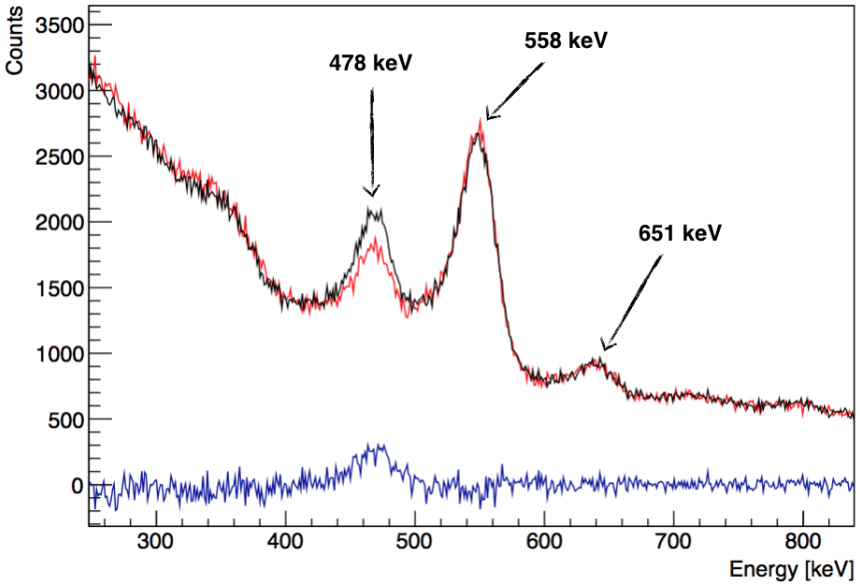

Figure 5.15: BPA spectra at 300W without Boral shielding: red line shows the background, black line shows the BPA spectrum, blue line shows the subtraction.

On the base of such experimental evidence, a study is under way to open another channel at the L.E.N.A. reactor to be used specifically for prompt gamma analysis and BNCT-SPECT measurements. The new channel would be free of any 478 keV background contamination since it is specifically studied for such measurements and would not employ any material containing ^{10}B. In this future scenario, further measurements will be performed adding a PMMA phantom to study a more realistic small animal BNCT-SPECT setup using the 5x5x20 mm^3 CZT detector prototype.

5.4 Cadmium capture reaction peak and neutron flux

Despite the removal of the Boral shield from the thermal column we saw that the results were not sufficient to appreciate the 478 keV peak due to the sample. Nonetheless we took advantage of the new thermal column configuration to study the response of the CZT detector to increasing thermal neutron fluxes as shown in Fig. 5.16. All the measurements were taken without the boron vial and for 600 s live time, since the reactor power was never over 500 W the detector was not shielded from the neutrons thus it is possible to see in the spectra the Cadmium capture reaction peak at 558 keV.

The data was obtained by means of the MAESTRO software tool to select

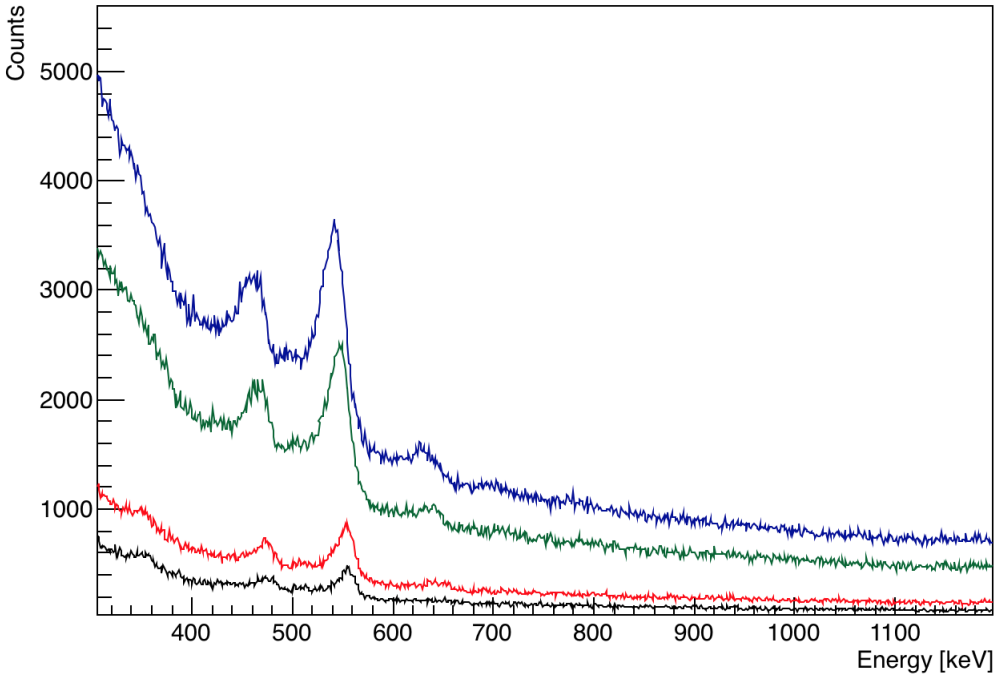

Figure 5.16: Spectra acquired in the thermal column without Boral shielding at 50 W (black), 100 W (red), 300 W (green) and 500 W (blue) reactor power.

a peak and fit it with a gaussian while removing the platform noise and the results are shown in Tab. 5.4. In addition we evaluated the thermal neutron flux in the 5x5x20 mm^3 CZT prototype detector. The simulated neutron flux for each reactor power is shown in Tab.5.4 and is correlated to the measured cps as shown in Fig. 5.17.

The area under the Cd peak, and thus the counts per second, is directly

Reactor Power [W]	Thermal neutron flux [n s^{-1} cm^{-2}]	Peak [keV]	FWHM [keV]	Net Area	cps
50	$3.46 \cdot 10^3$	555.9	12.9	2661	4.43
100	$6.92 \cdot 10^3$	553.9	17.5	5805	9.68
300	$2.08 \cdot 10^4$	546.7	20.8	19565	32.61
500	$3.46 \cdot 10^4$	542.6	25.9	33871	56.45

Table 5.4: Data acquired using MAESTRO software for various reactor powers.

proportional to the reactor power and thus to the neutron flux arriving on the CZT prototype detector. As we can see in Fig. 5.17 the counts per second increase as the thermal neutron flux increases.
We can fit the data with a linear function to find the correlation between cps

under the cadmium peak and the thermal neutron flux. The equation obtained is 5.1.

$$cps = (1.61 \cdot 10^{-3} \pm 0.02 \cdot 10^{-3}) \cdot (Neutron\ Flux) \tag{5.1}$$

In conclusion we can say that when the CZT is exposed to a unitary thermal

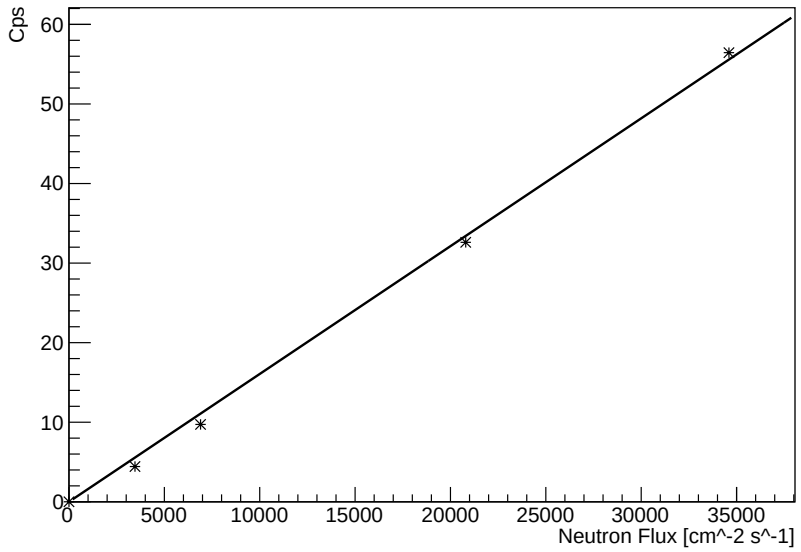

Figure 5.17: Correlation between cadmium peak cps and thermal neutron flux.

neutron flux we would expect a $1.61 \cdot 10^{-3}$ cps under the Cadmium peak. This data can be used to understand the shielding needed for the CZT prototype detector to suppress the cadmium contribution to the spectrum and reduce the system dead time.

Conclusions and future perspectives

Boron Neutron Capture Therapy is a binary radiotherapy. The first step consists in administering to the patient a ^{10}B carrier compound able to accumulate preferentially in the tumour, the second step is to irradiate the tumour with thermal neutrons. The efficacy of the therapy is based on the neutron capture reaction n + ^{10}B $\rightarrow$ ^{7}Li + α of the thermal neutrons on the boron compound. In the 94% of captures the ^{7}Li ion is produced in an excited state which causes the emission of a gamma ray of 478 keV energy.
Since the alpha particles and ^{7}Li ions have a range smaller than the mean cell diameter most of the reaction energy is deposited in the cell where the reaction took place. Therefore reconstructing the point of origin of the emitted 478 keV gamma would allow us to find with a great precision the place where the reaction took place, and thus the microscopic distribution of ^{10}B in tumour cells at the time of irradiation. Moreover the 478 keV gamma counts would give us an information directly about the dose deposited in the cell through equation:

$$D \propto \int n_B \sigma \phi dV$$

In BNCT many methods have been developed to calculate the boron concentration in samples and *in-vivo* but none of them is able to give a measurement in real time while the patient is being treated. A BNCT-SPECT system would give us a direct estimation of the treatment dose delivered to the patient not only the information on the boron concentration.
To develop such BNCT-SPECT system a detector with good energy and spatial resolution is needed. Moreover the detector must be able to be fitted inside a treatment room working in a mixed neutron and photon field. To such purpose we chose to study a CdZnTe detector because it has an energy resolution at 500 keV (3% with a 5x5x20 mm^3 CZT) much higher than the NaI(Tl) scintillators commonly used as clinical SPECT detectors. Moreover if we compare the CZT detector to the state of art solid state spectrometer (HPGe) we find that the energy resolution is comparable, moreover taking into account that

the CZT detector requires smaller crystal volumes and doesn't need any cooling system. Another advantage of using a CZT detector is that we can obtain a good spatial resolution by segmenting the electrodes with strips that allows to use lower number of reading channels than a pixelated detector.
To understand the properties and to test the performance of the CZT detector we performed both simulations and measurements.
At first we studied the imaging capabilities of a 20x20x20 mm^3 CZT detector that would be the base element for a bigger array of detectors to be employed in the SPECT imaging system and that would be made of 4 5x20x20 mm^3 detectors, each with its own read-out electronics. We simulated the energy resolution and efficiency of the 20x20x20 mm^3 detector when used to detect the gammas from various standard sources in the energy range between 250 keV to 1400 keV and we found that at 276 keV the efficiency is 67.13% and at high energies, such as 1333 keV, the efficiency is 7.83%. Moreover the expected efficiency of the detector in the energy range of interest for BNCT-SPECT (478 keV) is 30.8%.
We also simulated the image reconstruction abilities of the 20x20x20 mm^3 detector which has 80 pixels of 1x5 mm^2 with 20 mm thickness obtaining, when a Back Projection algorithm is used, a spatial resolution of about 6 mm when the source is located at 21 cm from the detector.
The results tell us that a BNCT-SPECT imaging system for small animals with a 20x20x20 mm^3 CZT detector should be able to reconstruct images with a 6 mm spatial resolution if the distance between source and detector is decreased and the angular step is thickened while the data collecting time is considered of about 30 minutes which is compatible with a typical BNCT treatment time.
In the framework of the INFN 3CATS project two 5x20x20 mm^3 CZT detectors are being built representing half of our simulated BNCT-SPECT base element. In the next year we will begin testing them to see if the simulated response can be confirmed by the measurements and to further study the feasibility of the BNCT-SPECT imaging system. Moreover to further improve the image reconstruction we aim to introduce a collimator and to explore different reconstruction algorithms.
An important part of the thesis project was the experimental characterization of the 5x5x20 mm^3 CZT detector, which could be considered as a sub-unit of the 5x20x20 mm^3 3CATS prototype.
The CZT detector was characterized at first with standard gamma sources and some simulations of the detector were also performed with MCNP6 and Geant4 Monte Carlo codes and validated with the experimental results. The efficiency of the detector at 478 keV energy was found to be 6.08%.
Afterwards we performed some experiments at the TRIGA Mark II research reactor of Pavia University to study the response of the 5x5x20 mm^3 CZT detector to a mixed neutron and gamma field.
This study is fundamental because during BNCT treatment the SPECT imaging system would be exposed to such mixed field and to understand its response

to thermal neutrons due to the high presence of Cadmium in the detector crystal.
To perform the measurements in the TRIGA Mark II thermal column we modified the irradiation chamber using the results of some MCNP6 simulations. The best irradiation setup was based on a 4 cm diameter neutron beam.
Through these experiments we were able to find the correlation between the measured cps under the 558 keV Cadmium photopeak and the mean thermal neutron flux on the detector volume. We found that we can expect an increase of $1.61 \cdot 10^{-3}$ cps for thermal flux unit. We can exploit this result to build the thermal neutron shield for the CZT detector, and thus optimize the data collection of our BNCT-SPECT imaging system.
Since the results of the measurements in the TRIGA Mark II thermal column showed that the high 478 keV gamma background can not be reduced we are presently planning to move the measurements to a different reactor channel that will be built specifically for prompt gamma analysis and SPECT measurements, as such it would be built without any material containing ^{10}B.
In the next year we aim to start a new measurement campaign involving both the 5x5x20 mm^3 detector as well as the new CZT prototype of 3CATS project and using the new reactor channel.

Acknowledgements

WARNING: saying thank you is never going to be enough to express my gratitude and the joy of knowing each one of you, so please consider this as it is: a misguided attempt to reduce to a couple of sentences a great deal more!

I would like to thank Professor Saverio Altieri for welcoming me to the Pavia BNCT group (see Fig. A), for giving me the possibility to learn many new things, for these years of guidance and help, and for all the opportunities that he has given me during my PhD years in Pavia.
To Nicoletta Protti I want to say that all this work would have not been possible without your constant help, and encouragement. Your dedication to the research and your wonderful attitude toward this job taught me a lot. Thank you for guiding me during these three years and for taking me on so many adventures with our dear CZT detector (see Fig. CZT).
I also want to thank Silva Bortolussi for being always ready to help and answer all my questions, but mostly for all the encouragement you showed me.
I want to thank Nanjing University of Areonautics and Astronautics and all the wonderful people I met in Nanjing, thank you for welcoming me to China and showing me your magnificent culture, history and kindness. Xièxie!
Most of all I want to thank my friend Chunhui for all her help while I was in Nanjing and for all the trips around Nanjing and China.
I also want to thank Professor Xiaobin Tang for the opportunity he gave me by welcoming me for more than 2 months in his research group (see Fig. B).
I want to thank L.E.N.A. laboratory and all the reactor staff for helping me in these three years of research, mostly I want to thank Michele Prata for all his help.

When I moved to Pavia I found the pillars of my new life, thank you Ian for always being present for me with your kindness and warmth, for all our Sunday lunches and photo adventures, thank you for always looking out for me. The dark side of the bottle would not be the same without Mario, thank you for all the 2 o'clock chats and for all the times you were there to give me new perspectives, thank you for all it was 'till it was.

My new home would have not been the same without Barbara, I believe there are not enough words to say how much grateful I am to have you as a friend, thank you for these 2 years but mostly for these last months of laughs and tears, of making an empty house a true home.
Samuel(e) you are a true rock. Thank you for always being there ready to listen and for all the laughs, your brightness never ceases to amaze me. This little family we all created would not have been the same without you (See Fig. C).
I owe a great deal of thanks to Angelica. Thank you for all the wonderfully crazy times we got lost while hiking, for all the late night chats, your wisdom and mostly for always looking out for me. Let's not forget the beer-pong tournaments and the fact that you introduced me to (read: dragged me to play) rugby, one of the best things ever!

To my amazing rugby family (see Fig. D) thank you! To all the girls, Fenici and Rocce, you are great and this experience would have not been the same without you! Thank you Agnes, Sam, Divá, Bart, Novi and Ceci, you showed me camaraderie and kindness, we shared laughs and tears and many great times.
To Vale thank you for the moral support and all the good times eating Japanese food and drinking limoncello. #vecchiaiatop. #sushisbronza #laprovacostumeno
Alessia thank you for sharing this PhD road with me and for the ability to always find a new way to make us all smile.
Once again I want to thank Elena, always there for a nice chat and some orecchiette or linguine or pollo alla piastra. I think this is the third of my theses you witness and this says a lot! Thank you!

Thank you Raquel for these three years of friendship, for all the late night motivational quotes and the "balconing" while writing this thesis. Haber si me muero! Thank you mann!
Michi it is wonderful to have you as a friend, in these last years I have always known that you would be there for me when I needed it and I'm forever grateful for that (see Fig. E).

Claudia and Fabia, we have known each other for a long time now, we shared so many experiences and thoughts that it is impossible to summarize them here, it is wonderful to still be friends and see where our life brought us, and share all the hard times (see Fig. F) and all our victories, thank you so much!

To Amedeo I want to say thank you for coming back to my life after so much time, with you I want to thank all the people that shared with me the first struggles of the physics degree back in Torino.

Most of all I want to thank my parents for all that you taught me and all that you do for me, for supporting this crazy dreams I have, I love you.
A big, gigantic thank you to my big sister Laleh you are my inspiration and my compass in this world, without you I would be lost. I love you!

There is a special thank you and a special place in my heart for whom I loved but lost during these years. Thank you for sharing part of this road with me, I will never forget it.

Fig. A

Fig. B

Fig. C

Fig. D

Fig. E

Fig. F

PhD Career Improvement:

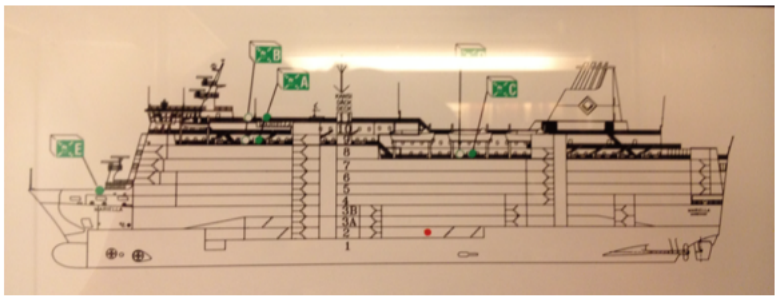

June 2015 - First PhD Mission - Stockholm-Helsinki
Deck 2

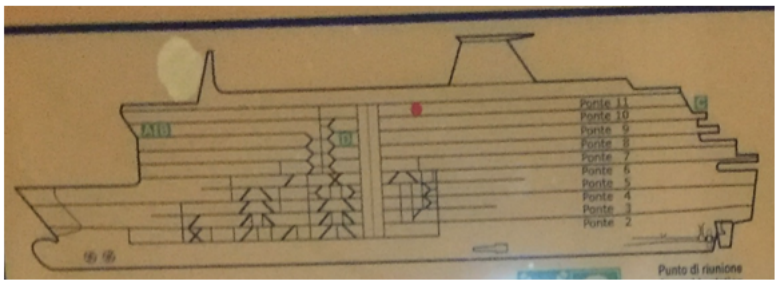

December 2017 - Last PhD Mission - Napoli-Palermo
Deck 11

FIG. CZT

Bibliography

[1] Rolf F Barth, Jeffrey A Coderre, M Graça H Vicente, and Thomas E Blue. Boron neutron capture therapy of cancer: current status and future prospects. *Clinical Cancer Research*, 11(11):3987–4002, 2005.

[2] Wolfgang AG Sauerwein, Andrea Wittig, Raymond Moss, and Yoshinobu Nakagawa. *Neutron capture therapy: principles and applications*. Springer Science & Business Media, 2012.

[3] Andrea Wittig, Jean Michel, Raymond L Moss, Finn Stecher-Rasmussen, Heinrich F Arlinghaus, Peter Bendel, Pier Luigi Mauri, Saverio Altieri, Ralf Hilger, Piero A Salvadori, et al. Boron analysis and boron imaging in biological materials for boron neutron capture therapy (bnct). *Critical reviews in oncology/hematology*, 68(1):66–90, 2008.

[4] Fred G Smith, Daniel R Wiederin, RS Houk, Claire B Egan, and Robert E Serfass. Measurement of boron concentration and isotope ratios in biological samples by inductivey coupled plasma mass spectrometry with direct injection nebulization. *Analytica chimica acta*, 248(1):229–234, 1991.

[5] Susan Evans and Urs Krähenbühl. Improved boron determination in biological material by inductively coupled plasma mass spectrometry. *Journal of Analytical Atomic Spectrometry*, 9(11):1249–1253, 1994.

[6] Hans Vanhoe, Richard Dams, Carlo Vandecasteele, and Jacques Versieck. Determination of boron in human serum by inductively coupled plasma mass spectrometry after a simple dilution of the sample. *Analytica chimica acta*, 281(2):401–411, 1993.

[7] Juha Laakso, Martti Kulvik, Inkeri Ruokonen, Jyrki Vähätalo, Riitta Zilliacus, Markus Färkkilä, and Merja Kallio. Atomic emission method for total boron in blood during neutron-capture therapy. *Clinical chemistry*, 47(10):1796–1803, 2001.

[8] Heikki Joensuu, Leena Kankaanranta, Tiina Seppälä, Iiro Auterinen, Merja Kallio, Martti Kulvik, Juha Laakso, Jyrki Vähätalo, Mika Kortesniemi, Petri Kotiluoto, et al. Boron neutron capture therapy of brain

tumors: clinical trials at the finnish facility using boronophenylalanine. *Journal of neuro-oncology*, 62(1):123–134, 2003.

[9] SJ González, MR Bonomi, GA Santa Cruz, HR Blaumann, OA Calzetta Larrieu, P Menéndez, R Jiménez Rebagliati, J Longhino, DB Feld, MA Dagrosa, et al. First bnct treatment of a skin melanoma in argentina: dosimetric analysis and clinical outcome. *Applied radiation and isotopes*, 61(5):1101–1105, 2004.

[10] Yoshinobu Nakagawa, Kyonghon Pooh, Toru Kobayashi, Teruyoshi Kageji, Shinichi Uyama, Akira Matsumura, and Hiroaki Kumada. Clinical review of the japanese experience with boron neutron capture therapy and a proposed strategy using epithermal neutron beams. *Journal of neuro-oncology*, 62(1):87–99, 2003.

[11] Silva Bortolussi, Laura Ciani, Ian Postuma, Nicoletta Protti, Luca Reversi, Piero Bruschi, Cinzia Ferrari, Laura Cansolino, Luigi Panza, Sandra Ristori, et al. Boron concentration measurements by alpha spectrometry and quantitative neutron autoradiography in cells and tissues treated with different boronated formulations and administration protocols. *Applied Radiation and Isotopes*, 88:78–80, 2014.

[12] W Enge, K Grabisch, R Beaujean, and K-P Bartholmä. Etching behaviour of a cellulose nitrate plastic detector under various etching conditions. *Nuclear Instruments and Methods*, 115(1):263–270, 1974.

[13] Leon C Edwards. Autoradiography by neutron activation: The cellular distribution of boron-10 in the transplanted mouse brain tumour. *The International journal of applied radiation and isotopes*, 1(3):184in5189–188in6190, 1956.

[14] GR Solares and RG Zamenhof. New approach to the microdosimetry of neutron capture therapy. *Transactions of the American Nuclear Society;(United States)*, 65(CONF-920606–), 1992.

[15] Guido R Solares, Robert G Zamenhof, and Guillermo Cano. Microdosimetry and compound factors for neutron capture therapy. In *Advances in neutron capture therapy*, pages 213–216. Springer, 1993.

[16] CS Yam, RG Zamenhof, and GR Solares. Microdosimetric evaluations of boron compound efficacy. *Transactions of the American Nuclear Society*, 73(CONF-951006–), 1995.

[17] GR Solares and RG Zamenhof. A novel approach to the microdosimetry of neutron capture therapy. part i. high-resolution quantitative autoradiography applied to microdosimetry in neutron capture therapy. *Radiation research*, 144(1):50–58, 1995.

[18] S Bortolussi and S Altieri. Boron concentration measurement in biological tissues by charged particle spectrometry. *Radiation and environmental biophysics*, 52(4):493–503, 2013.

[19] Paul T. Callaghan. *Principles of nuclear magnetic resonance microscopy*. Oxford University Press on Demand, 1993.

[20] George W Kabalka, Chao Tang, and Peter Bendel. The role of boron mri in boron neutron capture therapy. *Journal of neuro-oncology*, 33(1-2):153–161, 1997.

[21] Simonetta Geninatti-Crich, Diego Alberti, Ibolya Szabo, Annamaria Deagostino, Antonio Toppino, Alessandro Barge, Francesca Ballarini, Silva Bortolussi, Piero Bruschi, Nicoletta Protti, et al. Mri-guided neutron capture therapy by use of a dual gadolinium/boron agent targeted at tumour cells through upregulated low-density lipoprotein transporters. *Chemistry-A European Journal*, 17(30):8479–8486, 2011.

[22] Diego Alberti, Nicoletta Protti, Antonio Toppino, Annamaria Deagostino, Stefania Lanzardo, Silva Bortolussi, Saverio Altieri, Claudia Voena, Roberto Chiarle, Simonetta Geninatti Crich, et al. A theranostic approach based on the use of a dual boron/gd agent to improve the efficacy of boron neutron capture therapy in the lung cancer treatment. *Nanomedicine: Nanotechnology, Biology and Medicine*, 11(3):741–750, 2015.

[23] Dale L Bailey, David W Townsend, Peter E Valk, and Michael N Maisey. *Positron emission tomography*. Springer, 2005.

[24] Yoshio Imahori, Satoshi Ueda, Yoshio Ohmori, Kenji Sakae, Tsukasa Kusuki, Tooru Kobayashi, Masao Takagaki, Koji Ono, Tatsuo Ido, and Ryou Fujii. Positron emission tomography-based boron neutron capture therapy using boronophenylalanine for high-grade gliomas: part i. *Clinical Cancer Research*, 4(8):1825–1832, 1998.

[25] Yoshio Imahori, Satoshi Ueda, Yoshio Ohmori, Kenji Sakae, Tsukasa Kusuki, Tooru Kobayashi, Masao Takagaki, Koji Ono, Tatsuo Ido, and Ryou Fujii. Positron emission tomography-based boron neutron capture therapy using boronophenylalanine for high-grade gliomas: part ii. *Clinical Cancer Research*, 4(8):1833–1841, 1998.

[26] George W Kabalka, Gary T Smith, Jonathan P Dyke, William S Reid, et al. Evaluation of fluorine-18-bpa-fructose for boron neutron capture treatment planning. *The Journal of Nuclear Medicine*, 38(11):1762, 1997.

[27] Tooru Kobayashi and Keiji Kanda. Microanalysis system of ppm-order 10b concentrations in tissue for neutron capture therapy by prompt gamma-ray spectrometry. *Nuclear Instruments and Methods in Physics Research*, 204(2-3):525–531, 1983.

[28] Cornelis PJ Raaijmakers, Mark W Konijnenberg, Luc Dewit, Dietrich Haritz, Rene Huiskamp, Katharina Philipp, Axel Siefert, Finn Stecher-Rasmussen, and Ben J Mijnheer. Monitoring of blood-10b concentration for boron neutron capture therapy using prompt gamma-ray analysis. *Acta Oncologica*, 34(4):517–523, 1995.

[29] PM Munck af Rosenschöld, WFAR Verbakel, CP Ceberg, F Stecher-Rasmussen, and BRR Persson. Toward clinical application of prompt gamma spectroscopy for in vivo monitoring of boron uptake in boron neutron capture therapy. *Medical physics*, 28(5):787–795, 2001.

[30] Tooru Kobayashi, Yoshinori Sakurai, and Masayori Ishikawa. A noninvasive dose estimation system for clinical bnct based on pg-spect?conceptual study and fundamental experiments using hpge and cdte semiconductor detectors. *Medical physics*, 27(9):2124–2132, 2000.

[31] Glenn F Knoll. Single-photon emission computed tomography. *Proceedings of the IEEE*, 71(3):320–329, 1983.

[32] Steve Webb. *The physics of medical imaging*. CRC Press, 1988.

[33] Philippe P Bruyant. Analytic and iterative reconstruction algorithms in spect. *Journal of Nuclear Medicine*, 43(10):1343–1358, 2002.

[34] Kenneth Lange, Richard Carson, et al. Em reconstruction algorithms for emission and transmission tomography. *J Comput Assist Tomogr*, 8(2):306–16, 1984.

[35] Delphine Lazaro, Z El Bitar, Vincent Breton, David Hill, and Irene Buvat. Fully 3d monte carlo reconstruction in spect: a feasibility study. *Physics in Medicine and Biology*, 50(16):3739, 2005.

[36] Leon Kaufman, John Ewins, William Rowan, Ken Hosier, Michael Okerlund, and Douglas Ortendahl. Semiconductor gamma-cameras in nuclear medicine. *IEEE Transactions on Nuclear Science*, 27(3):1073–1079, 1980.

[37] Jerrold T Bushberg and John M Boone. *The essential physics of medical imaging*. Lippincott Williams & Wilkins, 2011.

[38] National Research Council et al. *Mathematics and physics of emerging biomedical imaging*. National Academies Press, 1996.

[39] I Murata, T Mukai, S Nakamura, H Miyamaru, and I Kato. Development of a thick cdte detector for bnct–spect. *Applied Radiation and Isotopes*, 69(12):1706–1709, 2011.

[40] A Valda, DM Minsky, AJ Kreiner, AA Burlon, and H Somacal. Development of a tomographic system for online dose measurements in

bnct (boron neutron capture therapy). *Brazilian journal of physics*, 35(3B):785–788, 2005.

[41] Daniel M Minsky, AA Valda, AJ Kreiner, S Green, C Wojnecki, and Z Ghani. Experimental feasibility studies on a spect tomograph for bnct dosimetry. *Applied Radiation and Isotopes*, 67(7):S179–S182, 2009.

[42] Daniel M Minsky, AA Valda, AJ Kreiner, S Green, C Wojnecki, and Z Ghani. First tomographic image of neutron capture rate in a bnct facility. *Applied Radiation and Isotopes*, 69(12):1858–1861, 2011.

[43] Stefano Del Sordo, Leonardo Abbene, Ezio Caroli, Anna Maria Mancini, Andrea Zappettini, and Pietro Ubertini. Progress in the development of cdte and cdznte semiconductor radiation detectors for astrophysical and medical applications. *Sensors*, 9(5):3491–3526, 2009.

[44] William Shockley. Currents to conductors induced by a moving point charge. *Journal of applied physics*, 9(10):635–636, 1938.

[45] Simon Ramo. Currents induced by electron motion. *Proceedings of the IRE*, 27(9):584–585, 1939.

[46] Karl Hecht. Zum mechanismus des lichtelektrischen primärstromes in isolierenden kristallen. *Zeitschrift für Physik A Hadrons and Nuclei*, 77(3):235–245, 1932.

[47] RH Redus, JA Pantazis, AC Huber, VT Jordanov, JF Butler, and B Apotovsky. Fano factor determination for czt. *MRS Online Proceedings Library Archive*, 487, 1997.

[48] Alan Owens and Anthony Peacock. Compound semiconductor radiation detectors. *Nuclear Instruments and Methods in Physics Research Section A: Accelerators, Spectrometers, Detectors and Associated Equipment*, 531(1):18–37, 2004.

[49] Tadayuki Takahashi and Shin Watanabe. Recent progress in cdte and cdznte detectors. *IEEE Transactions on Nuclear Science*, 48(4):950–959, 2001.

[50] RO Bell, G Entine, and HB Serreze. Time-dependent polarization of cdte gamma-ray detectors. *Nuclear Instruments and Methods*, 117(1):267–271, 1974.

[51] P Siffert, J Berger, C Scharager, A Cornet, R Stuck, RO Bell, HB Serreze, and FV Wald. Polarization in cadmium telluride nuclear radiation detectors. *IEEE Transactions on Nuclear Science*, 23(1):159–170, 1976.

[52] Miles N Wernick and John N Aarsvold. *Emission tomography: the fundamentals of PET and SPECT*. Academic Press, 2004.

[53] N Auricchio, E Caroli, G De Cesare, W Dusi, D Grassi, M Hage-Ali, E Perillo, P Siffert, and G Spadaccini. Spectroscopic response versus interelectrodic charge formation position in cdte detectors. *MRS Online Proceedings Library Archive*, 487, 1997.

[54] Irfan Kuvvetli, C Budtz-Jrgensen, E Caroli, N Auricchio, E Kalemci, and JB Stephen. Charge collection and depth sensing investigation on czt drift strip detectors. In *Nuclear Science Symposium Conference Record (NSS/MIC), 2010 IEEE*, pages 3880–3884. IEEE, 2010.

[55] JC Lund, R Olsen, JM Van Scyoc, and RB James. The use of pulse processing techniques to improve the performance of cd/sub 1-x/zn/sub x/te gamma-ray spectrometers. In *Nuclear Science Symposium and Medical Imaging Conference Record, 1995., 1995 IEEE*, volume 1, pages 126–130. IEEE, 1995.

[56] HH Barrett, JD Eskin, and HB Barber. Charge transport in arrays of semiconductor gamma-ray detectors. *Physical Review Letters*, 75(1):156, 1995.

[57] PN Luke and EE Eissler. Performance of cdznte coplanar-grid gamma-ray detectors. *IEEE Transactions on Nuclear science*, 43(3):1481–1486, 1996.

[58] Yuu Okada, Tadayuki Takahashi, Goro Sato, Shin Watanabe, Kazuhiro Nakazawa, Kunishiro Mori, and Kazuo Makishima. Cdte and cdznte detectors for timing measurements. *IEEE Transactions on Nuclear Science*, 49(4):1986–1992, 2002.

[59] R Amrami, G Shani, Y Hefetz, A Pansky, and N Wainer. Timing performance of pixelated cdznte detectors. *Nuclear Instruments and Methods in Physics Research Section A: Accelerators, Spectrometers, Detectors and Associated Equipment*, 458(3):772–781, 2001.

[60] Arnaud Drezet, Olivier Monnet, Françoise Mathy, Guillaume Montemont, and Loïck Verger. Cdznte detectors for small field of view positron emission tomographic imaging. *Nuclear Instruments and Methods in Physics Research Section A: Accelerators, Spectrometers, Detectors and Associated Equipment*, 571(1):465–470, 2007.

[61] E Bertolucci, M Conti, CA Curto, and P Russo. Timing properties of cdznte detectors for positron emission tomography. *Nuclear Instruments and Methods in Physics Research Section A: Accelerators, Spectrometers, Detectors and Associated Equipment*, 400(1):107–112, 1997.

[62] P Vaska, A Dragone, W Lee, D-H Kim, J-F Pratte, Y-G Cui, J Fried, S Krishnamoorthy, A Bolotnikov, S-J Park, et al. A prototype czt-based pet scanner for high resolution mouse brain imaging. In *Nuclear Science*

Symposium Conference Record, 2007. NSS'07. IEEE, volume 5, pages 3816–3819. IEEE, 2007.

[63] Y Eisen, A Shor, and I Mardor. Cdte and cdznte gamma ray detectors for medical and industrial imaging systems. *Nuclear Instruments and Methods in Physics Research Section A: Accelerators, Spectrometers, Detectors and Associated Equipment*, 428(1):158–170, 1999.

[64] Lucie Guerin, LoÏck Verger, VÉronique Rebuffel, and Olivier Monnet. A new architecture for pixellated solid state gamma camera used in nuclear medicine. *IEEE Transactions on Nuclear Science*, 55(3):1573–1580, 2008.

[65] JF Butler, CL Lingren, SJ Friesenhahn, FP Doty, WL Ashburn, RL Conwell, FL Augustine, B Apotovsky, B Pi, T Collins, et al. Cdznte solid-state gamma camera. *IEEE Transactions on Nuclear Science*, 45(3):359–363, 1998.

[66] Y Eisen, I Mardor, A Shor, Z Baum, D Bar, G Feldman, H Cohen, E Issac, R Haham-Zada, S Blitz, et al. Nucam3-a gamma camera based on segmented monolithic cdznte detectors. *IEEE Transactions on Nuclear Science*, 49(4):1728–1732, 2002.

[67] L Verger, MC Gentet, L Gerfault, R Guillemaud, C Mestais, O Monnet, G Montemont, G Petroz, JP Rostaing, and J Rustique. Performance and perspectives of a cdznte-based gamma camera for medical imaging. *IEEE Transactions on Nuclear Science*, 51(6):3111–3117, 2004.

[68] Douglas J Wagenaar, Samir Chowdhury, John C Engdahl, and Darrell D Burckhardt. Planar image quality comparison between a cdznte prototype and a standard nai (tl) gamma camera. *Nuclear Instruments and Methods in Physics Research Section A: Accelerators, Spectrometers, Detectors and Associated Equipment*, 505(1):586–589, 2003.

[69] Sea Agostinelli, John Allison, K al Amako, J Apostolakis, H Araujo, P Arce, M Asai, D Axen, S Banerjee, G Barrand, et al. Geant4?a simulation toolkit. *Nuclear instruments and methods in physics research section A: Accelerators, Spectrometers, Detectors and Associated Equipment*, 506(3):250–303, 2003.

[70] John Allison, Katsuya Amako, Jea Apostolakis, HAAH Araujo, P Arce Dubois, MAAM Asai, GABG Barrand, RACR Capra, SACS Chauvie, RACR Chytracek, et al. Geant4 developments and applications. *IEEE Transactions on Nuclear Science*, 53(1):270–278, 2006.

[71] Rene Brun and Fons Rademakers. Root?an object oriented data analysis framework. *Nuclear Instruments and Methods in Physics Research Section A: Accelerators, Spectrometers, Detectors and Associated Equipment*, 389(1-2):81–86, 1997.

[72] Numpy Developers. Scientific computing tools for python-numpy, 2010.

[73] Stefan Van der Walt, Johannes L Schönberger, Juan Nunez-Iglesias, François Boulogne, Joshua D Warner, Neil Yager, Emmanuelle Gouillart, and Tony Yu. scikit-image: image processing in python. *PeerJ*, 2:e453, 2014.

[74] T Goorley, M James, T Booth, F Brown, J Bull, LJ Cox, J Durkee, J Elson, M Fensin, RA Forster, et al. Initial mcnp6 release overview. *Nuclear Technology*, 180(3):298–315, 2012.

[75] H Böck and M Villa. Triga reactor characteristics. *Atomic Institute of the Austrian Universities Technical Report AIAU*, 27306, 2004.

[76] T Pinelli, S Altieri, F Fossati, A Zonta, D Cossard, U Prati, L Roveda, G Ricevuti, and R Nano. Development of a method to use boron neutron capture therapy for diffused tumours of liver (taormina project). In *Cancer neutron capture therapy*, pages 783–794. Springer, 1996.

[77] S Bortolussi and S Altieri. Thermal neutron irradiation field design for boron neutron capture therapy of human explanted liver. *Medical physics*, 34(12):4700–4705, 2007.

[78] S Bortolussi, N Protti, M Ferrari, I Postuma, S Fatemi, M Prata, F Ballarini, MP Carante, R Farias, SJ González, et al. Neutron flux and gamma dose measurement in the bnct irradiation facility at the triga reactor of the university of pavia. *Nuclear Instruments and Methods in Physics Research Section B: Beam Interactions with Materials and Atoms*, 414:113–120, 2018.

[79] C Gong, S Fatemi, N Protti, I Postuma, S Bortolussi, C Geng, X Tang, and S Altieri. Optimization of the therrmal column of pavia triga mark ii reactor for bnct-spect experiment. *High Power Laser and Particle Beams*, 29(12), 2017.

[80] DE Baker. Graphite as a neutron moderator and reflector material. *Nuclear Engineering and design*, 14(3):413–444, 1971.

[81] DS McGregor, JT Lindsay, and RW Olsen. Thermal neutron detection with cadmium1- x zincx telluride semiconductor detectors. *Nuclear Instruments and Methods in Physics Research Section A: Accelerators, Spectrometers, Detectors and Associated Equipment*, 381(2-3):498–501, 1996.

List of Publications

1. S. Bortolussi, N. Protti, M. Ferrari, I. Postuma, S. Fatemi, M. Prata, F. Ballarini, M. P. Carante, R. Farias, S. J. González, M. Marrale, S. Gallo, A. Bartolotta, G. Iacoviello, D. Nigg and S. Altieri. (2018). *Neutron flux and gamma dose measurement in the BNCT irradiation facility at the TRIGA reactor of the University of Pavia.* Nuclear Instruments and Methods in Physics Research Section B: Beam Interactions with Materials and Atoms, 414, 113-120.

2. Gong Chunhui, Fatemi Setareh, Protti Nicoletta, Postuma Ian, Bortolussi Silva, Geng Changran, Tang Xiaobin, Altieri Saverio. *Optimization of thermal column of Pavia TRIGA Mark II reactor for BNCT-SPECT experiment.* High Power Laser and Particle Beams, 2017, 29(12): 29126004-.

3. S. Fatemi, C.H Gong, S. Bortolussi, I. Postuma, N. Protti, G. Benassi, N. Zambelli, M. Bettelli, A. Zappettini, X.B. Tang and S. Altieri. *CHARACTERIZATION OF A CdZnTe DETECTOR PROTOTYPE FOR BORON IMAGING BY SPECT* Radiazioni - Ricerca e Applicazioni, Aprile-Agosto 2017 della rivista (vol. XX n.1-2)

4. Chunhui Gong, Xiaobin Tang, Setareh Fatemi, Haiyan Yu, Wencheng Shao, Diyun Shu and Changran Geng. *A Monte Carlo study of SPECT in boron neutron capture therapy for a 2 heterogeneous human phantom* Accepted by International Journal of Radiation Research.